Effects of Localization on Autonomous Formation Flight: A Simulation-Based Analysis

Doctoral Thesis
(Dissertation)

to be awarded the degree
Doctor of Engineering (Dr.-Ing.)

submitted by
Mehmet Can Kılıç
from Ankara, Turkey

approved by
the Faculty of Mathematics/Computer Science
and Mechanical Engineering,
Clausthal University of Technology

Date of oral examination
28.08.2020

Dean

Prof. Dr.-Ing. Volker Wesling

Chairperson of the Board of Examiners

Prof. Dr. Stephan Westphal

Supervising tutor

PD Dr.-Ing. habil. Umut Durak

Reviewers

Prof. Dr. Sven Hartmann

Assoc. Prof. Dr. Shafagh Jafer
Embry-Riddle Aeronautical University

Acknowledgments

The development of this thesis started during my employment as a guest researcher at the Department of Unmanned Aircraft, at the Institute of Flight Systems of the German Aerospace Center (DLR) in Braunschweig.

Hereby, I would like to thank everyone, who supported me throughout the course of this thesis.

First of all, I would like to express my gratitude to my doctoral advisor, PD Dr.-Ing. habil. Umut Durak for accepting to supervise this work, his encouragement and helpful advice. I am thankful to Prof. Dr. Sven Hartmann and Assoc. Prof. Dr. Shafagh Jafer from Embry-Riddle Aeronautical University for reviewing the thesis.

I would like to thank, Prof. Dr.-Ing. Stefan Levedag for providing helpful feedback about my work, Jörg Dittrich and Johann Dauer for supporting me in starting the research at the DLR. I also thank the members of the Institute of Flight Systems, particularly the Department of Unmanned Aircraft, for their guidance.

Finally, I would like to thank my family for their patience and continuous support during the course of this thesis.

Mehmet Can Kılıç

Abstract

Effects of Localization on Autonomous Formation Flight: A Simulation-Based Analysis

In order to execute the formation flight autonomously, the relative position information of the participating aircraft is required, which is obtained from sensors and navigation solutions. The relative position, which is also referred to as relative localization, is then processed by automatic control systems for the execution of the mission. Since the sensors and navigation solutions are not ideal, the relative position information provided by them includes certain deficiencies. These deficiencies eventually have an influence on the performance of the autonomous formation flight. Considering the relative position information as the essential information enabling the formation flight, this work investigates, how the deficiencies of the relative localization affect the performance of the formation flight.

An autonomous formation flight of two aircraft is considered on a straight and level flight path, in which the follower aircraft's formation flight controller is responsible for maintaining the aircraft's relative position at a commanded location with respect to the leader aircraft. The deficiencies of the relative position information are represented by three parameters: The magnitude of error, delay and sampling period. The performance of the formation flight is expressed by the maximum relative position error of the aircraft during a predefined duration of formation keeping.

This work uses nonlinear flight simulation as the main means of investigation. In order to find out the effects of the aforementioned parameters on the formation flight performance, repetitive runs of simulations are employed, among which the parameter values are varied. The results of the simulations are presented graphically. Complementing the simulation results, system-theoretical models are derived, which approximate the effects of the parameters on the maximum relative position error during formation flight.

Kurzfassung

Auswirkungen der Lokalisierung auf den autonomen Formationsflug: Eine simulationsbasierte Analyse

Damit ein Formationsflug autonom ausgeführt werden kann, ist relative Positionsinformation der teilnehmenden Flugzeuge erforderlich, welche von den Sensoren und Navigationslösungen geliefert werden. Die relative Positionsinformation, die auch als relative Lokalisierung bezeichnet wird, wird von den automatischen Flugregelungssystemen für die Ausführung der Mission verarbeitet. Da die Sensoren und Navigationslösungen nicht ideal sind, enthaltet die von ihnen gelieferte relative Positionsinformation gewisse Schwächen. Diese Schwächen haben dann Einfluss auf die Leistung des autonomen Formationsfluges. Unter Berücksichtigung der relativen Positionsinformation als wesentliche Information, die den Formationsflug ermöglicht, untersucht diese Arbeit, wie sich die Schwächen der relativen Lokalisierung auf die Leistung des Formationsfluges auswirken.

Ein autonomer Formationsflug von zwei Flugzeugen wird auf einer geraden und ebenen Flugbahn betrachtet, bei der der Formationsflug-Regler des Follower-Flugzeugs dafür verantwortlich ist, die relative Position des Flugzeugs an einer kommandierten Stelle in Bezug auf das Leader-Flugzeug aufrechtzuerhalten. Die Schwächen der relativen Positionsinformation werden durch drei Parameter repräsentiert: die Grösse des Fehlers, die Verzögerung in der Datenübertragung und die Abtastperiode. Die Leistung des Formationsfluges wird durch den maximalen relativen Positionsfehler des Flugzeugs während einer vordefinierten Dauer der Formationshaltung dargestellt.

Diese Arbeit verwendet nichtlineare Flugsimulation als Hauptuntersuchungsinstrument. Um die Auswirkungen der zuvor-genannten Parameter auf die Leistung des Formationsfluges herauszufinden, werden wiederholte Läufe von Simulationen verwendet, unter denen die Parameterwerte variiert werden. Die Ergebnisse der Simulationen werden grafisch dargestellt. Ergänzend zu den Simulationsergebnissen werden systemtheoretische Modelle abgeleitet, die die Auswirkungen der Parameter auf den maximalen relativen Positionsfehler während des Formationsfluges approximieren.

Contents

List of Figures

List of Tables

Nomenclature

Symbols

Some symbols have multiple meanings through the entirety of the text. The meanings provided below are the default meanings, which can be adopted unless otherwise stated in the respective part of the text. This also holds for the units of the entities.

Scalars	**Explanation**	**Units**
$Æ$	Wing aspect ratio	–
b	Wing span	m
$\overline{c}$	Wing mean aerodynamic chord	m
C_D	Drag coefficient	–
C_{D_0}	Zero-lift drag coefficient	–
C_L	Lift coefficient	–
C_l	Aerodynamic moment coefficient along x-axis	–
C_m	Aerodynamic moment coefficient along y-axis	–
C_n	Aerodynamic moment coefficient along z-axis	–
C_X	Aerodynamic force coefficient along x-axis	–
C_Y	Aerodynamic force coefficient along y-axis	–
C_Z	Aerodynamic force coefficient along z-axis	–
d	Relative position information delay	s
D	Drag force	N
e	Wing efficiency number	–
g	Gravitational acceleration	m/s^2
I	Moment of inertia	$kg \times m^2$
k	Relative position information error attenuation factor	–
K	Constant controller gain	case-dependent
L	Lift force	N
m	Mass	kg
p	Rotational velocity vector component along the x-axis	rad/s
q	Rotational velocity vector component along the y-axis	rad/s
$\overline{q}$	Dynamic pressure	N/m^2
r	Rotational velocity vector component along the z-axis	rad/s

Scalars	**Explanation**	**Units**
R_g	Gravity scale factor	–
R_l	Length scale factor	–
R_ρ	Density scale factor	–
S	Wing area	m^2
T	Thrust force	N
T	Relative position information sampling period	s
t	Time	s
V	Ground velocity	m/s
W	Weight	N
u	Velocity vector component along the x-axis	m/s
v	Velocity vector component along the y-axis	m/s
w	Velocity vector component along the z-axis	m/s
x	Position vector component along the x-axis	m
y	Position vector component along the y-axis	m
z	Position vector component along the z-axis	m
X	Force vector component along the x-axis	N
Y	Force vector component along the y-axis	N
Z	Force vector component along the z-axis	N
α	Angle of attack	rad
β	Angle of sideslip	rad
δ_a	Aileron deflection	rad
δ_e	Elevator deflection	rad
δ_r	Rudder deflection	rad
δ_t	Throttle setting	–
γ	Climb angle	rad
χ	Course angle	rad
ϕ	Bank angle	rad
θ	Pitch angle	rad
ψ	Azimuth angle	rad
ρ	Air density	kg/m^3
ζ	Damping ratio	–
τ	Time constant	s
ω	Natural frequency	rad/s
λ	Time delay	s

Vectors	Explanation
$\overline{\boldsymbol{e}}_r$	True relative position error vector
$\boldsymbol{F}$	Force vector
$\boldsymbol{M}$	Moment vector
$\boldsymbol{r}$	Position vector
$\boldsymbol{u}$	Control vector
$\boldsymbol{x}$	State vector
$\boldsymbol{V}$	Velocity vector
$\boldsymbol{y}$	Output vector
$\boldsymbol{\Omega}$	Angular velocity vector

Matrices	Explanation
$\boldsymbol{T}$	Transformation matrix

Subscripts and Superscripts

Some subscripts have multiple meanings, which are separated by commas below.

Symbol(s)	Explanation
A	Aerodynamic
B	Body-fixed reference frame
c	Commanded
cg	Center of gravity
d	Desired
F	Follower aircraft
I	Integral control action
K	Kinematic, Kinematic reference frame
L	Leader aircraft
mrp	Moment reference point
npt	Horizontal stabilizer neutral point
P	Proportional control action, Propulsive
t	Horizontal stabilizer
$trst$	Thrust, thrust vector action point
w	Wake-induced
W	Wind
x	x-component
y	y-component
z	z-component
0	North-East-Down reference frame

Chapter 1

Introduction

This chapter begins with a brief motivation to automated formation flight, by first stating the main application areas of formation flight in general, then expressing the need for automating the formation flight. Based on this background, the statement of the research problem is given thereafter. This is followed by a literature review section, focusing on the main aspects of the automated formation flight covered in this work.

1.1 Motivation

1.1.1 Application Areas of Formation Flight

Formation flight of aircraft is the flight of at least two aircraft as a group, which fly and maneuver synchronously in a predesignated manner; acting like a single aircraft in terms of navigation and position declaration [1]. Therefore the group of aircraft constitutes a *formation*.

Most commonly, the formation flight is practiced according to the scheme of *leader-follower formation*, in which one of the participating aircraft is chosen as the *leader* of the formation. The leader aircraft's responsibility is to guide the formation, in which all other, *follower* aircraft are commanded to follow the leader aircraft at desired relative positions with respect to the leader aircraft [2]. That is, the leader aircraft is responsible for the navigation, and the follower aircraft are responsible for maintaining the formation [3].

The main application areas of formation flight are aerial refueling, saving fuel due to aerodynamic benefits, increase in the intensity of aerial defense or attack, and increased efficiency with regard to air traffic control [4, 5].

Today, the formation flight is primarily used during *aerial refueling*, which is a widely practiced capability in military aviation. It is the airborne transfer of fuel from a *tanker* aircraft to *receiver* aircraft, which increases the mission endurance of

the receiver aircraft. Aerial refueling also makes it possible for the receiver aircraft to take off with less fuel in order to get more payload or reduce the minimum required length of the runway. Although currently practiced by military aircraft, the aerial refueling is also envisioned for civil transport aircraft due to the economical benefits that it can provide as a result of increased range and payload [6]. It was estimated that, utilization of aerial refueling can enable today's intercontinental civil air transportation to benefit from about 15-30 percent reduction in fuel and CO_2 emissions, depending on the range of the flight [7, 8].

Two methods of aerial refueling are available today: The *probe and drogue* and the *boom and receptacle* methods. In the probe and drogue method, the receiver aircraft docks its refueling boom attached to its front into a free-flying refueling drogue, which is connected to the tanker's fuel tanks with a flexible hose. In the boom and receptacle method, a boom operator on-board the tanker guides a telescopic refueling boom into a receptacle on the upper part of the receiver aircraft, which maintains its position within the reach of the refueling boom. With either of the methods, in order for an aerial refueling mission to succeed, the receiver and the tanker aircraft are required to fly in accordance with the leader-follower formation described above. During the aerial refueling mission, the tanker aircraft has the role of the leader and the receiver aircraft have the role of the follower. In the probe and drogue method, after the receiver pilot successfully docks into the refueling drogue, he has to fly in formation with the tanker, maintaining a constant relative position with respect to the tanker as accurately as possible, in order to avoid unwanted detachments with the drogue and keep a safe distance with the tanker. Also for the initiation of the docking phase, the receiver aircraft must establish formation with the tanker aircraft, which is accurate enough to permit a docking attempt. Likewise in the boom and receptacle method, the receiver aircraft must fly in formation with the tanker accurately, in order to allow the boom operator to dock the boom into the receptacle, avoid unwanted detachments with the boom during the fuel transfer, and maintain a safety distance with the tanker.

The area where the receiver aircraft is located during the docking and fuel transfer phases is called *refueling area* [9], as shown in Figure 1.1. This is not the only area, in which the receiver aircraft fly formation with the tanker. Formation flying with the tanker aircraft is necessary also before and after the docking and actual fuel transfer phases in both refueling methods. According to the procedures described by NATO (North Atlantic Treaty Organization) [9], the receiver aircraft are commanded to join the formation with the tanker from the tanker's left side, and maintain their position at an area called *observation area*, until each receiver gets the clearance to enter the refueling area. Likewise, after a receiver aircraft gets the fuel from the tanker and undock from the tanker's refueling equipment, it is commanded to enter into the *reform area* [9]. This is an area, which is located at the right side of the tanker, and the receiver is commanded to maintain its position in this area until it receives the

clearance to separate from the formation. These steps are necessary for procedural reasons in order to guide the receiver aircraft to safely join and leave the proximity of the tanker aircraft. Therefore, it can be said that the entire aerial refueling mission is built on the base of accurate formation flying capability, which is therefore a strong factor determining the success and the safety of the mission.

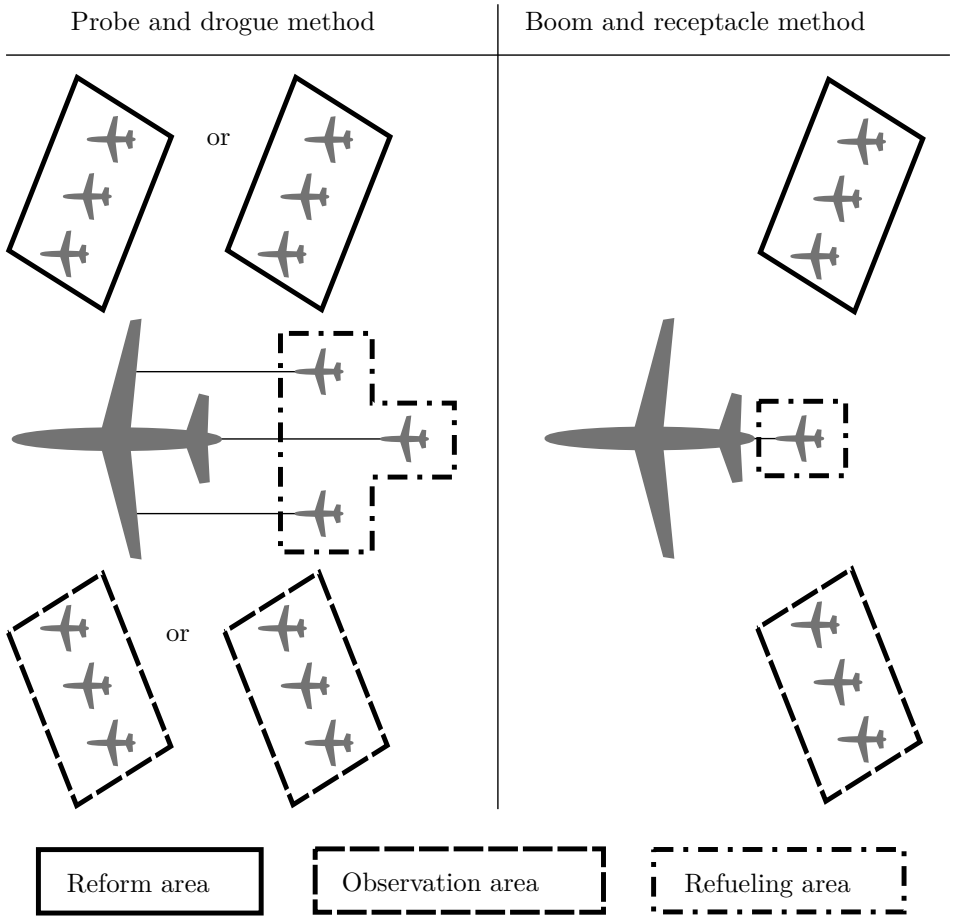

Figure 1.1: Formation flying positions during aerial refueling according to the procedures described by NATO [9]. View from above. For the probe and drogue method, the rear observation and reform areas are used, if there is an observer aircraft behind the tanker-receiver formation.

Another application area of the formation flight lies in the field of aerodynamics. During the flight of an airplane, the airplane's wing generate lift force, due to the greater average pressure on the lower surface of the wing than that on the upper surface [10]. As a result of this pressure difference, the air tends to flow around the wingtips from lower side to upper side, following a circular path [10]. As the aircraft translates in the air, it leaves this circulatory motion of air, stretching from the tips of each wing downstream. This flow of air generated behind the aircraft is called in the literature *wake vortices* [11, 12], *trailing vortices* [10, 13] or *wingtip vortices* [10, 14].

The trailing vortices that an airplane leaves behind also influence the motion of the surrounding air, as depicted by Figure 1.2. The vortices induce upward flow of air, i.e. *upwash*, at right and left sides of the aircraft. If another airplane flies at proper locations in these upwash regions, the upward airflow help the airplane generate less induced drag [14]. Therefore less thrust will be required for the airplane to maintain a steady flight, whose direct consequence is fuel savings. This is where the formation flight can be used to utilize this aerodynamic advantage. If an airplane flies formation with another airplane, keeping its position in the upwash region, the follower aircraft can benefit from fuel savings up to 20 %, theoretically [15]. It has also been demonstrated in different flight experiments that drag reductions of 10-20 % is achievable for a follower aircraft in formation at the leader's wake [16]. If applied to commercial transport aircraft, this drag reduction may enable substantial reduction of fuel over a given amount of operation period. It is reported that, a 1 % drag reduction due to formation flight may offer fuel savings between about 13000 kg and 45000 kg per aircraft per year with the utilization rates of today's commercial transport aircraft [17]. Cruising flights at routes with high flight frequencies form a potential area in which the formation flight's aerodynamic benefits might be put into use by future commercial aircraft [18]. In this respect, a recent numerical study [19] reports 1.8 % reduction in the combined fuel consumption of two wide-body airliners, which establish a formation in the course of their trans-Atlantic routes.

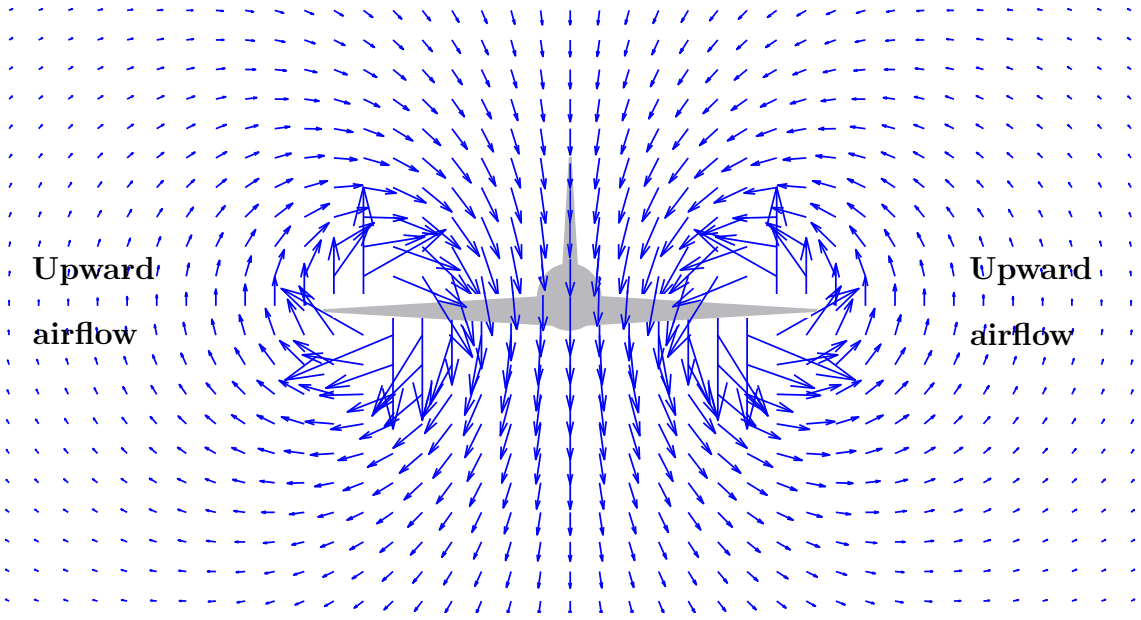

Figure 1.2: Flow field behind an aircraft. View from the rear. Arrows show the direction of the local airflow. The size of the arrows show the relative strength of the airflow.

The accuracy of the position keeping during the formation flight is an important factor for the drag reduction applications. In order to fully benefit from the maximum drag reduction potential, the follower aircraft must be placed at a location in the

upwash region of the leader aircraft, which gives the maximum drag reduction. This location is named in the literature as *sweet spot* [14, 20, 21]. If the follower aircraft cannot perform an accurate position keeping at the sweet spot, it cannot benefit from the drag reduction to its full extent. It is reported on a numerical formation flight study with aircraft of identical geometry that, if the follower aircraft cannot maintain its position at the sweet spot within an accuracy of ten percent of a wingspan, it looses half of the drag reduction benefits [22]. Further inaccuracies in follower aircraft's position keeping may even result in the aircraft's nearing the core of the trailing vortex. The strength of the circulatory air flow within the trailing vortex is so strong that it can cause loss of control on the follower aircraft [23]. Therefore accurate formation flight capability is an enabling factor for profiting from the flow field behind another aircraft, and a necessary skill for conducting this operation in a safe and reliable manner.

As introduced previously, other applications of formation flight are in the fields of military and air traffic control (ATC). From the military point of view, carrying out a defense or attack mission will be much more effective, if multiple aircraft take part in the operation. The firepower is proportional to the number of aircraft taking part in the mission. Furthermore, multiple aircraft make target or task allocation possible among involving aircraft. Additionally, among the military transport aircraft, formation flight is used as regular practice for reliable and efficient deployment of numerous aircraft [24]. Another military-application area of formation flight is covered operations, in which the probability of detection of the aircraft by ground-based systems is critical [25]. In such missions military aircraft fly close to the ground in formation, with aircraft flying exactly behind another. This decreases the land area over which the aircraft fly, reducing the probability of detection from the ground [25].

From the air traffic control point of view, formation flying reduces the workload of the air traffic control operators, since the formation of aircraft is handled as a single aircraft [26]. After a formation of aircraft switches to a new ATC radio frequency, the leader aircraft is responsible to communicate with the ATC on behalf of all aircraft participating in the formation that it leads [1]. In this communication, the leader informs the ATC that it is leading a formation and declares the number of aircraft that take part in formation [1]. Then the air traffic control treats the formation as a single aircraft in terms of navigation, position reporting and issuing of clearances [1]. Therefore the efforts of the air traffic control operator is reduced per the total number of aircraft guided.

In the next section, the necessity of automating the formation flight is discussed. Before proceeding further with the corresponding details, a brief discussion is given on the terms *automated* and *autonomous*, as the terms are often used interchangeably in the literature, but different definitions also exist for them.

Within the context of information science, the term automation is defined as the approaches used for carrying out tasks with minimum human intervention. The term

autonomous, however, refers to the capability of self-decision and self-governance [27]. In the field of automotive, different automation levels are described depending on the extent and complexity of the tasks which can be performed by the vehicle without human intervention. In this respect, higher levels of automation are regarded as autonomy [28].

This work concentrates on performing a specific task, i.e. formation keeping, without human intervention. The means for automated decision making are not considered. As no human intervention is required for the presented task, and that the automation is the necessary step for reaching autonomy, this work is presented under the title autonomous formation flight. On the other hand, in order to have a clearer indication that the means for automated decision making are not considered, the term automated formation flight is more frequently used throughout the subsequent sections of the text.

1.1.2 The Need for Automated Formation Flight

The need for automation of the formation flight can be seen from two perspectives: The first one is pilot workload relief, and the second one is the increasing operational presence and importance of unmanned (uninhabited) aerial vehicles (UAVs).

As explained by Buzogany [29], formation flight can be an exhausting task for pilots to carry out: Flying in a formation, the pilots are required to visually monitor their relative position with respect to the neighboring aircraft, while reading their flight instruments. The difficulty of this task increases even further, in case of a tight formation or in the presence of external factors requiring extra attention of the pilot. These factors can be deterioration of visibility conditions, navigational tasks or reaction to the adversary threats [29]. Therefore, automation of formation flight would give pilots the time that they need for completing other mission-relevant tasks, alleviating their workload and decreasing their fatigue [25, 29–32]. These benefits of automation apply also to the specialized applications of formation flight, such as aerial refueling [33].

Another area, from which a need for automation of formation flight arises, is the unmanned aircraft, whose operational presence is increasing in military and civil applications. The UAVs offer mission capabilities that are difficult or too risky to perform with manned aircraft, such as continuous surveillance in distant sites with extended duration, and situational evaluation in dangerous environments [34]. There are also armed UAVs [35], which have been active in various military forces. These UAVs are intended for carrying out similar functions as today's manned military aircraft, towards which aerial refueling is regarded as an important step [36]. Formation flight capability for the UAVs is directly implied here, along with being a key for UAVs' gathering further manned flight capabilities explained above.

The UAVs can be operated in autonomous or remotely-piloted fashion. However,

in order to make full use of what UAVs offer, especially in reduction of the number of required personnel and long distance, high endurance operations, UAV missions have been automated [37]. Therefore, automated formation flight capability is foreseen for the UAVs, in order to combine the benefits of formation flight with the capabilities of the UAVs to their fullest extent.

1.2 Terminology

In order to avoid uncertainties in meanings of terms and attain a clearer distinction among them, some definitions are given below. The given definitions are not necessarily the universal definitions, but the ones adopted in this text.

Formation keeping means the follower aircraft's control of its relative position with respect to the leader in order to constantly remain at a commanded relative position with respect to the leader. The terms *station keeping*, *position keeping*, *maintaining position*, or *maintaining formation* are also used in the text, corresponding to the same definition.

The term *automatic pilot* is used for any control law, which enables the aircraft to track commanded values of a set of state variables by generating appropriate commands of aerodynamic surface deflections and throttle setting for the aircraft's actuators. The term is also used in the text simply as *autopilot*. For the automatic pilot used in this work, the tracked state variable is translational velocity.

The term *formation controller* refers to the follower aircraft's position control law, which controls the relative position of the follower with respect to the leader by generating appropriate commands for the automatic pilot. Other terms, which are used in the text with the same meaning, are *formation flight controller* and *formation hold controller*.

A *guidance algorithm* stands for any control law or algorithm, that controls the position or spatial trajectory of an aircraft by generating appropriate commands for the autopilot. Examples: Formation flight controller, path-following algorithm. The term is also denoted in the text simply as *guidance*.

An *inner-loop controller* is a control law, whose input, i.e., setpoint or command signal, is determined by another control law or guidance algorithm. For instance, the autopilot is an inner-loop controller with respect to the formation-hold controller. Similarly, with respect to the autopilot, the formation-hold controller is an *outer-loop controller*.

The term *flight data* is used in the text for denominating any flight-related data that the aircraft's systems require in order to pursue the automated flight, which are obtained from sensors, navigation solutions. The term does not make a distinction whether the flight data is relative to another aircraft or defined in absolute sense, that is, with respect to an inertial reference frame. Examples: Relative or absolute

velocity, position, attitude angles, dynamic pressure, etc. The term flight data is used in the text interchangeably with the term *flight information*. If the flight data is defined with respect to the corresponding flight data of another aircraft, the terms *relative flight data*, *relative flight information*, *relative navigation data*, or *relative states* are used. The relative flight data are obtained by subtracting the flight data of one aircraft from the same flight data of another aircraft. Examples: Relative velocity, relative position, relative attitude, etc.

Finally, the term *relative position data* is used to refer to the relative position of the follower aircraft with respect to the leader, which is required by the follower's formation controller for relative position control. Follower aircraft acquires this information from any sensor, navigation solution, or any combination of them. The term is also used in the text as *relative position information*.

1.3 Problem Statement and Methodology

1.3.1 Problem Statement

In order for a follower aircraft to fly formation with a leader aircraft, the follower aircraft requires the information of the leader besides the usual set of flight data that it requires for a solo flight. Since the formation flight is a relative positioning task, follower-leader relative position information is required by the follower aircraft, so that it is able to position itself with respect to the leader. In the automated formation flight literature, although different formation control approaches require different set of data from the leader, in all approaches the common ingredient of the leader data is the relative position information [2, 3, 25, 29, 38–66]. Among these, some formation control approaches only require the relative position information of the leader [25, 39, 40, 42, 55–57, 60]. Therefore it can be said that, the most fundamental leader information, that the follower aircraft requires, is its relative position with respect to the leader aircraft.

Various approaches are presented in the literature, by which the follower aircraft acquire the leader flight data. In some approaches, the follower aircraft is designated to obtain the leader's flight data solely by on-board sensors, such as cameras [58, 67]. In such approaches image processing algorithms extract the leader relative position information from the leader's images captured by the cameras. In other approaches, the follower aircraft gathers the leader aircraft flight data from sensors placed on the leader. Typical sensors are global positioning systems (GPS) [54, 60, 62] or both GPS and inertial navigation systems (INS) [3, 49, 52, 53, 59, 68]. The GPS and inertial sensor measurements are usually coupled by filters such as Kalman filter [53, 68] for obtaining a navigation solution. In these approaches, the leader aircraft sends its flight data to the follower through wireless data links. The relative navigation

information is then obtained by comparing the leader's flight data with the follower's flight data. For instance, in case the leader sends its absolute position information to the follower aircraft, the follower calculates its relative position with respect to the leader by subtracting leader's absolute position from its own absolute position. The follower's flight data are generally obtained from the sensors or navigation solutions of the same type as those on the leader. A more detailed discussion on the means of obtaining the relative navigation information between the leader and follower aircraft can be found in Section 1.4.2.

During a manually-flown formation flight, the follower aircraft pilot visually monitors the distance between the leader and his aircraft in order to position his aircraft appropriately. Therefore, it is the pilot who obtains and processes the relative position information. On the other hand, in an automated formation flight, the pilot is replaced by guidance algorithms and automatic control systems for execution of the control tasks. These guidance and control systems process the leader's relative position data, which are provided by sensors and navigation solutions outlined above. However, regardless of the type of the sensors and navigation solutions, the relative position data that are provided by those will not be perfect. That is, the data obtained from these sources will have deficiencies in terms of frequency, accuracy, and up-to-dateness. In this work, these deficiencies of relative position data are regarded as the determinants of the quality or the characteristics of the information. Table 1.1 shows the existence of these deficiencies in relative position information, based on existing methods presented in the literature. The first column lists a set of exemplary means of obtaining the relative position information for the follower aircraft with corresponding references. The characteristics of the relative position information are represented by the sampling period, maximum error and the delay of the information, as listed in the second to fourth columns of the table respectively. As illustrated in the second column of the table, the relative position information becomes available to the follower aircraft only at certain intervals of time. Similarly, besides containing error in it, the relative position information is not always up-to date. That is, there can be delays present in it by the time it becomes available to the follower aircraft, making the information outdated. Under normal conditions all these deficiencies are likely to be present in the relative position data that the follower aircraft's formation controller processes at a certain degree. This degree of presence may further escalate under unfavorable conditions due to atmospheric disturbances, adversary threats, nature of the mission, etc., which are discussed in Section 1.4.2. It is assumed that the deficiencies of the relative position information will adversely affect the performance of the automated formation keeping, because the follower aircraft's formation controller processes the relative position information in order to maintain the formation. Except preliminary studies by the author [69, 70], it has not been investigated in the literature, how the effects of these deficiencies manifest themselves on the performance of the automated formation flight. Hence the main scope of this work is to

find out how the follower aircraft's formation keeping performance is affected by the characteristics of the relative position information.

Information source	**Sampling period (s)**	**Maximum error (m)**	**Delay (s)**
2 × GPS [71]	0.5	2.74 (3σ)	0.5
2 × GPS with dead reckoning [71]	0.1	1.14 (3σ)	–
2 × GPS-INS fusion [3]	0.05	1.52	–
2 × GPS-INS fusion [53, 68]	0.05	0.42 (3σ)	0.1
Computer vision [67]	0.1–0.24	–	–
Computer vision [72]	–	1.11 (3σ)	–

Table 1.1: Characteristics of relative position data obtained from different flight data sources.[1]

Recalling the main application areas of formation flight from Section 1.1.1, the importance of accurate formation keeping becomes evident. In applications such as aerial refueling or drag reduction, inaccuracy of the formation keeping may cause complete or partial failure of the mission. Furthermore, due to the collision risks arising from being in close vicinity of other aircraft during applications such as aerial refueling, accuracy of the station keeping becomes decisive also for the safety of the mission.

Due to its importance in formation flight applications, the accuracy of the formation keeping is regarded in this work as the measure of the performance of formation flight. From this standpoint, the factors affecting the performance, i.e. the accuracy of automated formation flight gain importance, in order to be able to tell whether a safe and successful formation flight mission can be carried out. One of such factors is the characteristics of the relative position information, that the follower aircraft's formation controller processes for maintaining the formation. Understanding the effects of the relative position data characteristics on the performance of the automated formation keeping can prove useful during mission design phases. Knowing the characteristics of the relative position information and the properties of the aircraft which take part in the formation flight, performance predictions can be made in order to tell whether the mission can be carried out in a safe, reliable, and effective manner. Furthermore, in case of degradation of the quality of the relative position information during the mission, such a prediction capability can be used for autonomous decision making, in order to tell whether the mission should be further executed or aborted.

[1]The values are under normal operating conditions. The sign "–" is used, if the corresponding information cannot be deduced from the given reference. The sign "2 ×" is used to imply that the relative position is between two separate sets of sensors, one on each aircraft. The sign "3σ" is used for the cases, in which the corresponding reference presents the standard deviation information of the error. In these cases, the maximum error is approximated as three times the error standard deviation, applying the three-sigma rule. The three-sigma rule is described in Section 3.1.

1.3.2 Formation Flight Scenario

As they constitute one of the main foreseen use cases of automated formation flight, UAVs are considered in this work. A leader-follower formation flight with one conventional, fixed-wing UAV-leader and one conventional, fixed-wing UAV-follower aircraft is studied. The formation flight is fully automated, that is, no pilot or operator control is required. Furthermore, corrective or preventive operator interventions, as well as automated collision avoidance algorithms are not considered.

In the formation flight scenario the leader UAV follows a straight and level flight path with a constant commanded velocity. The straight and level flight path is selected, due to its frequent use in formation flight applications. Due to its simplicity, it also helps avoid any side effects on follower's formation keeping performance, stemming from leader aircraft maneuvers. The follower aircraft is commanded to maintain its relative position with respect to the leader at a given, fixed location.

Numerous combinations are possible with regard to the selection of properties and sizes of both leader and follower aircraft. An analysis of the effects of different aircraft combinations on the formation flight can be the topic of a separate study. In this regard, the most immediate effect of the relative size of the leader and the follower aircraft is likely to be on the aerodynamic disturbances acting on the aircraft, and such an analysis is left as future work. Therefore, for the sake of simplicity, keeping inter-aircraft dissimilarities to a minimum is considered to be an adequate starting point. Hence, identical leader and follower UAVs are used. That is, both aircraft are identical [3, 39, 41, 45, 54, 64, 73, 74] in geometry, mass and mass distribution. Additionally, both aircraft are equipped with identical automatic pilots, which is a likely case if the airframes are identical. The only difference between the two aircraft lies in their guidance algorithms, in other words, the way the commands are generated for their autopilots. On the leader aircraft, the autopilot is driven by a path following algorithm, while on the follower aircraft the commands to the autopilot are generated by a formation hold controller. The structure of the follower aircraft's formation hold controller and the structure of the autopilots are of proportional-integral control type.

1.3.3 Problem Concretization and Methodology

In this work, the follower-leader relative position information, that the follower's formation-hold controller processes, is characterized by its properties in terms of frequency, accuracy, and up-to-dateness. These properties are represented by three parameters respectively: *sampling period*, *error magnitude*, and *delay*. For the sake of simplicity and generality, the parameters are handled without focusing on any specific information source, namely, sensors and navigation solutions together with communication systems. It is assumed that, regardless of the sensors or navigation solutions which provide the relative position information to the follower's formation

controller, the information sources will provide this information at a certain sampling period. Furthermore, the provided data will have error. The delays will also be present in the relative position information due to required processing times and communication systems. The parameters characterizing the relative position data are explained below.

The sampling period of the relative position information represents the constant time interval at which a new relative position information becomes available to the follower aircraft's formation hold controller.

In order to represent the error in the leader's relative position information, an additive, zero-mean error is used, which varies randomly throughout its samples. The sampling of the error is the same as the sampling of the relative position information. That is, at each sample that the relative position information becomes available to the follower's formation controller, the error has different values. Since the error is zero-mean, the error magnitude is specified in terms of the standard deviation of the error over the entire time span that the follower aircraft is holding the formation. For the distribution of the error's values throughout its samples, Gaussian probability distribution [75] is used, which is commonly chosen for modeling of the non-systematic measurement errors of sensors [76], including the ones typically used on aircraft [77].

The delay of the relative position information represents the age of the relative position information by the time it becomes available to the follower's formation hold controller. In other words, it is the time span, by which the current relative position information at the formation hold controller lags behind the actual relative position between two aircraft.

Figure 1.3 visualizes the three parameters characterizing the relative position information, which is provided to the follower aircraft's formation controller for processing. The relative position is a vector quantity. However, for simplicity, the figure is drawn only for one component of the relative position vector. The curve used for true relative position is a dummy curve selected for clearer visualization of the parameters. Similarly, the selected values of the sampling period, error magnitude and the delay length are solely for the ease of visualization. The values, that are used in the analysis, are made clear in the subsequent sections of the text.

Each signal shown in the figure depict the respective relative position information, which would be processed by the formation hold controller, if the conditions stated in the legend were met. Following the order in the legend, the first signal represents the perfect, i.e., continuous, error-free and delay-free, relative position information. In other words, the real, physical relative position between the two aircraft. In the ideal case, this real relative position is presented to the follower formation controller. The following signals on the figure depict the effect of each parameter. The second signal depicts the first signal, delayed by one second. The third signal shows, how the signal would look like, if the delayed signal is sampled at one-second periods. The fourth signal is the third signal, which is corrupted by an additive, zero-mean, random error

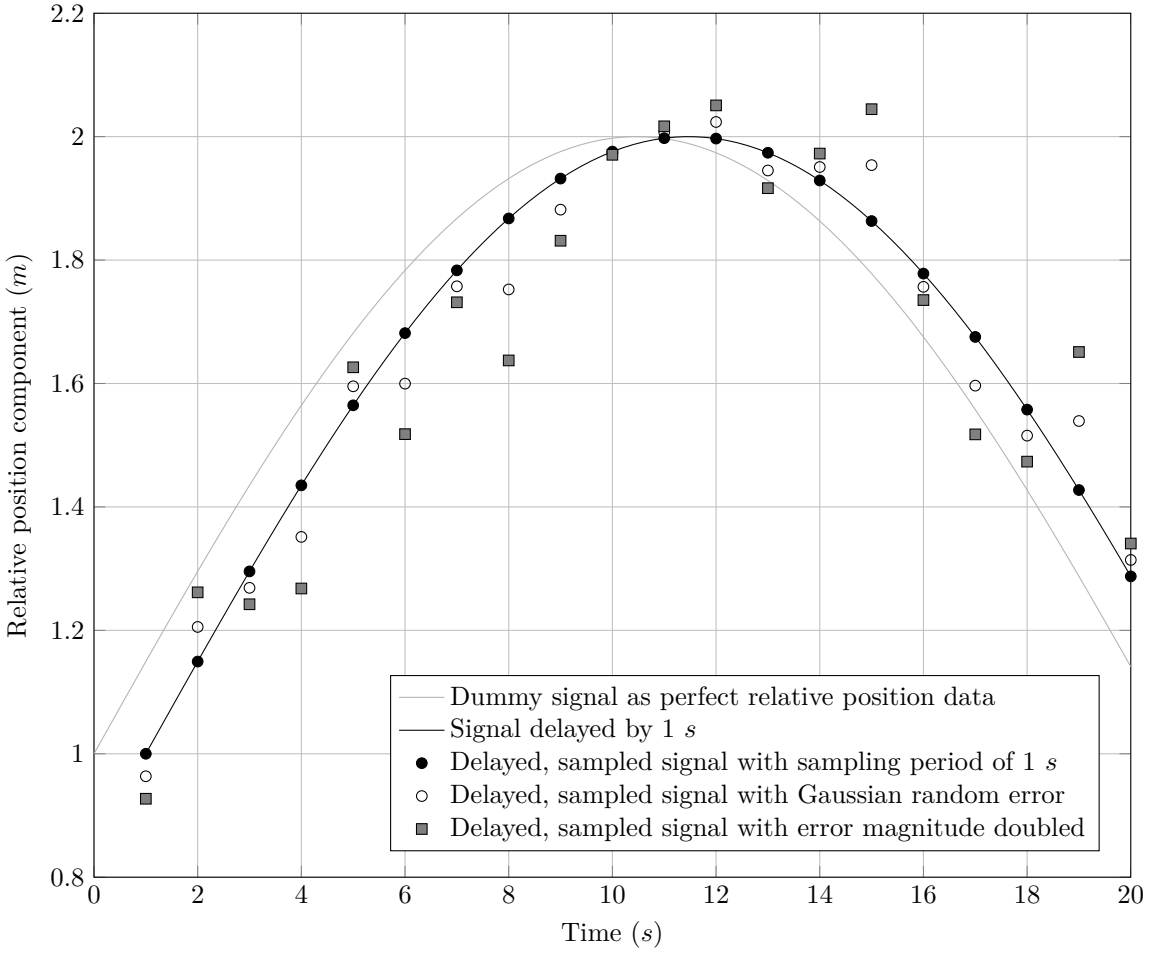

Figure 1.3: Visualization of the parameters characterizing the leader-follower relative position data presented to the follower's formation controller.

with an arbitrary magnitude, described above. The fifth signal is the same as the fourth except the magnitude of the added error, which is double the magnitude of the error in the fourth signal.

As a remark on the representation of the relative position information characteristics by the means introduced above, it is worth noting that, the followed approach is an approximation, which simplifies the problem. It is possible that, with a given set of values for the three parameters, the approach may not precisely describe the characteristics of a specific means of relative position data gathering. Namely, the approach does not attribute the primary importance on precision. Instead, more emphasis is given on the manageability of the problem, with the aim that the effect of each parameter on the performance of the formation keeping can be obtained.

The effect of the above parameters on the formation keeping performance of the follower aircraft is examined in this work. The term *formation keeping performance*

is represented in this work by the actual maximum relative position error between the leader and follower aircraft during the considered period of the formation keeping. As explained before, the accuracy of the position keeping is an important factor for the success and safety of the formation flight missions. The maximum position keeping error is used for representing the formation flight performance, in order to take the worst case into account during the station keeping.

Based on the terms explained above, the main research focus of this work can be formulated in question form as given below.

> *How do the sampling period, magnitude of error, and delay of the follower-leader relative position information, which is used by the follower aircraft's formation controller, affect the follower's actual maximum relative position error during the formation flight?*

The main approach selected for answering the above question is nonlinear simulation. The use of simulation for the problem studied in this work is advantageous with respect to real flight tests in terms of flexibility, controllability and repeatability. Simulation allows full control over the parameters and access to the desired flight data besides enabling the realization of the desired formation flight scenario. Furthermore, the repetition of the simulations with fixed flight conditions and parameters are possible. With respect to linear system-theoretical approaches [41, 78, 113], using a nonlinear formation flight simulation allows better description of the physics involved, by reducing the simplifying assumptions which would otherwise be necessary in order to make the problem manageable.

Six degree-of-freedom, nonlinear aircraft flight dynamical models are used for simulating the flight-dynamical behaviors of the leader and follower aircraft. The simulated flight conditions are outlined in Section 1.3.2. In order to see the effects of the parameters of the leader-follower relative position data on the follower's formation keeping, the simulation is run repetitively. In each run of the simulation one parameter is varied and the follower's actual formation keeping error is recorded during a predesignated duration of the formation flight simulation. At the end of the set of simulations, the effects of the parameters on the maximum formation keeping error are graphically presented. Later on, dynamical system analysis tools, such as system norms and frequency response, are also utilized in order to complement the explanations of the results obtained from the simulations, as well as for relating the results with aircraft closed-loop characteristics.

In this work, two scales of leader-follower aircraft pairs are used in the simulations; lower and higher-scale aircraft pairs. Within the simulations of each aircraft scale, the leader and follower aircraft are identical. In one set of simulations the aircraft are UAVs of 3.2-meter wing span, roughly classified as *small unmanned aircraft* [79]. In the other set of simulations *medium altitude, long endurance* (MALE) type of UAVs of 20-meter wingspan are used. The reason for using two different simulation sets of

different aircraft scales is to observe how the answer to the above question vary at different scales of aircraft. The two scales of aircraft are dynamically scaled versions of each other. That is, their geometry is the same and their dynamical properties, as well as their flight conditions are related to each other by known constants determined by the rules of dynamical scaling. For the simulations with each scale of aircraft, it is preferred to use dynamically-scaled aircraft, instead of using completely different and unrelated aircraft. This simplifies the correlation of the results obtained from each scale and drawing a comparative conclusion by reducing the secondary effects coming from other factors, such as aircraft aerodynamic characteristics, which are not under investigation in this work.

1.4 Literature Review

The previous research on formation flight, which are of relevance to this work, are viewed from three main aspects. These are guidance and control aspects of automated formation flight, the means of obtaining relative navigation data, and the aerodynamics of formation flight. Each of these aspects are covered in this work to different extents. The review presented in this section also extends the discussions presented in sections 1.1 and 1.3.

1.4.1 Guidance for Automated Formation Flight

In the work by Wilson et al. [65] the methods for automated formation flight guidance are grouped under three categories: Path-following-based formation flight guidance approaches, missile-guidance-inspired formation flight guidance, and feedback-control-based formation flight guidance. This classification is adopted in the following text. Although the automated formation flight guidance applied in this work is of the third category, the reviews of the first two categories are also presented for the sake of completeness.

In the path-following-based approaches, the leader and follower aircraft's autopilots are driven by path-following algorithms. Both aircraft are commanded to follow the same or interrelated flight paths, in order to constitute a formation. The extra task that follower aircraft has to perform in addition to following the path is to regulate its separation with the leader. Examples are the works by Park et al. [80] and Mahboubi et al. [81], which use horizontal, circular flight paths for bringing the leader and the follower aircraft into formation. Both approaches were tested in flight with small unmanned aircraft. Further applications of path-following-based formation flight are presented by Nakai and Uchiyama [82] and Nagao and Uchiyama [83]. They use vector-field-based path following approach [84] for bringing the leader and follower aircraft into a formation on a desired flight path, as well as for mid-air

collision avoidance. Small unmanned airplanes are used for demonstration of loose formation flight on circular [82, 83] and straight flight paths [82].

The distinction between the remaining two formation flight guidance methods lies in the way the leader-follower relative state information is expressed and used by the formation guidance. In the field of missile guidance, the relative state between the missile and the target is commonly represented in terms of a vector connecting the missile to the target, namely the *line of sight* (LOS) [85]. The missile guidance approaches then use the attributes of the LOS vector, such as its length (LOS range), orientation (LOS angle), rate of change, etc., in order to generate the guidance commands. An example is *pursuit* guidance in which the missile is commanded to align its velocity vector with the LOS vector [85]. The *proportional navigation* guidance is another example, in which the missile is commanded to rotate its velocity vector at a rate proportional to the rotation rate of the LOS vector [86]. In the missile-guidance-inspired formation flight approaches, the follower aircraft acts as the guided object, namely the missile, and the leader aircraft acts as the target [2]. The attributes of the LOS vector are used to guide the follower to the leader; but instead of intercepting the the leader aircraft, the follower is commanded to keep a desired separation with the leader [2]. For instance, the method of Segal et al. [2] uses the LOS angle information for generation of course and forward speed commands for the follower aircraft's autopilot. Similarly, the approach presented by Tahk et al. [51] uses the LOS range and LOS angle information and their rate of change for generation of acceleration commands in horizontal plane. Based on simulation, Segal et al. [2] present satisfactory formation flight performance for potential applications in which the accuracy of the station keeping is not of primary concern. Additionally, if the aircraft-to-aircraft distance is small, the LOS-angle-based relative position measurement becomes sensitive to the lateral and vertical relative position error components [87]. This may cause the LOS-angle-based guidance algorithm to behave unstably [60], as excessive correction commands can be generated on the lateral and vertical control channels. Despite these, the advantage of the LOS-based methods lies in that, the LOS data can be obtained by on-board sensors of the follower aircraft, such as camera and radar sensors; therefore the communication systems for sending the flight data from the leader to the follower can be avoided [65].

The final and the most widely-used method[2] of automated formation flight is the feedback-control-based approaches. This formation flight approach, which is also followed in this work, provides a more accurate station keeping than the other methods outlined above [65]. In this automated formation flight approach, the relative position of the aircraft is commonly expressed in a rotating Cartesian coordinate system, which is commonly attached to the leader [48, 52, 59] or the follower aircraft [41, 63]. There also exists a desired relative position, which is also expressed in the same coordinate

[2]e.g., Refs. 3, 4, 25, 29–32, 38, 39, 41, 43–46, 48, 49, 52, 53, 59, 61, 88

system. The follower aircraft is commanded to keep its position at this point. The relative position error, i.e., the difference between the follower aircraft's measured relative position and the desired relative position, is then driven toward zero using control laws such as proportional-integral control [25, 29–32]. Numerous variants of the feedback-control-based formation flight guidance approach exist, some of which are discussed below. These variants are mainly in terms of utilization of further states in the formation flight controller, as well as the use of different control laws.

One consideration during the design of formation flight controllers is the maneuvers of the leader, which can be seen by a station-keeping follower as external disturbance [89]. An example is the formation flight on an oval racetrack path, which is commonly used in aerial refueling applications [90]. On this path, the tanker aircraft transitions between straight and level flight, and steady and level turn. Hence it sequentially maneuvers from one flight condition to another. It is desired that the follower aircraft's formation controller reacts fast enough to the maneuvers of the leader, so that large position errors can be avoided. The methods for obtaining a more reactive formation flight controller against the leader's maneuvers include the utilization of further leader states such as bank angle and roll rate, which change faster during leader's maneuver than the relative position. By using the faster-changing leader states, the follower aircraft can react faster to the leader's maneuver than solely reacting to the increasing position error. The incorporation of these sates into the formation flight controller is done by means of feedforward [48, 52].

In the work by Campa et al. [48] a linear formation flight controller of proportional-derivative (PD) type is synthesized, which act on the relative position error. On the lateral and vertical channels, the formation flight controller generates bank and pitch angle commands for the follower aircraft's autopilot. The formation flight controller also have a feedforward component, in which the leader aircraft's bank and pitch angles are directly added to the output of the PD control action. Their simulation-based study show that using fed-forward attitude angles on the formation flight controller improves the follower's position keeping performance during the maneuvers of the leader aircraft. Another example for the use of feedforward in order to improve the formation keeping performance during leader maneuvers is the work by Ross et al. [52]. On the lateral control channel, they use proportional-integral-derivative (PID) control action on relative position error. The leader aircraft's states, which are used in feedforward, are the bank angle and the roll rate. The formation flight controller is also successfully tested in flight with a Learjet follower aircraft flying in tight formation with a Beechcraft C-12 leader. A similar set of leader flight data is required by the controller of Hansen et al. [53] and Dibley et al. [68], who demonstrate the automated formation flight as part of an automated aerial refueling flight test program. Successful automated station keeping is performed by an automated McDonnell Douglas F/A-18 receiver aircraft during straight and turning flight, behind a Boeing 707-300 tanker airplane.

Another concern for the formation flight controller design is the effect of the leader aircraft's wake on the follower aircraft. As shown in Figure 1.2 on page 22, the leader aircraft leaves a non-uniform, position-dependent induced velocity field in the downstream volume of air. As the follower aircraft flies within this induced-velocity field, it experiences aerodynamic forces and moments depending on its relative position with respect to the leader aircraft. These aerodynamic effects act as disturbances on the formation flight controller during its operation.

In the work by Proud [91] and Pachter et al. [41], the performance of a formation flight controller, which is developed without taking wake disturbance into account, is investigated under the wake disturbance. The study uses a three degree-of-freedom nonlinear equations of motion to model the aircraft dynamics. A proportional-integral formation flight controller is tuned for appropriate rejection of the disturbances due to the leader's heading, speed and altitude changes. The controller is then tested in formation flight simulations, in which the follower follows leader at the same altitude, with two wing spans longitudinal and about 0.8 wingspan of lateral separation. This relative position is denoted in the study as the minimum drag point for the follower aircraft. Although the most prominent wake disturbance at the minimum drag point is a rolling disturbance on the follower aircraft [3], the study only considers the force disturbances due to the sidewash and upwash. The controller behaves stably under the aerodynamic disturbance and shows comparable performance both with and without the wake disturbance. Based on these findings, Ross et al. [52] design a PID formation flight controller neglecting the wake disturbance, assuming that the controller is robust enough to cope with the disturbance effects. The controller is flight-tested with the leader and follower aircraft of business jet size, with the follower below the leader, holding formation at the boom and receptacle aerial refueling positions (figure 1.1 on page 21). The transitions between observation and refueling positions are also investigated. The controller exhibits stable and safe behavior at different formation positions, also during the transition maneuvers through the vicinity of the wake. Another study, which use flight tests in order to evaluate the formation flight controller's performance under the wake disturbance, is presented by Hanson et al. [3]. As part of their formation flight test program with two McDonnell Douglas F/A-18 aircraft, the follower's formation flight controller is tested at relative positions near the minimum drag location. The formation flight controller is a PID control action on relative position error, which directly generates the control stick commands of roll and pitch. The integral component of the controller on the lateral channel is denoted to be useful due to its ability to generate a command offset for compensation of the roll disturbance. In the flight tests, the formation controller behaves stably in the outer areas of the vortex up to wingtip-to-wingtip separations of a quarter wingspan with the aircraft at the same vertical position. However the controller cannot stabilize the follower aircraft as the airplane is commanded to approach the core of the vortex. At wingtip-to-wingtip separation of about one-eighth of a wingspan,

the follower aircraft experiences divergent lateral position and roll oscillations.

In addition to the studies outlined above, which treat the wake vortex effects as unknown disturbance and compensate the wake effects with appropriately-tuned linear controllers, studies also exist, which augment the baseline formation flight controller with modules devoted specifically to estimation and compensation of the wake disturbance. Adaptive modules are used in order to complement the commands generated by linear baseline controllers. In the studies by Lavretsky [44] and Misovec [45], baseline formation flight controllers with PID action on relative position error are used. The baseline controllers generate control stick and throttle commands. Adaptive modules use the relative position information with respect to the leader or its rate of change in order to estimate incremental control stick commands. These incremental commands are for compensation of the wake disturbance and are added to the output of the baseline controller. Both studies use the same wake vortex model and nonlinear, 6 degree-of-freedom equations of motion for modeling the dynamics of McDonnell Douglas F/A-18 aircraft. The follower aircraft are commanded to maintain a lateral separation of about 0.8 wingspan, behind and at the same altitude as the leader. With the baseline controller of Misovec [45], the follower experience lateral and vertical position oscillations during the station keeping at the sweet spot. The adaptive augmentation eliminates this oscillatory behavior. The baseline PID formation flight controller of Lavretsky [44] already perform a stable formation keeping at the sweet spot, with additional disturbance effects of turbulence and sensor noise, and a 0.1-second time delay in the control loop. The position keeping performance of the baseline controller is improved with the adaptive augmentation. In a recent simulation-based study by Zhang and Liu [92] the performances of a baseline and an augmented formation flight controller are compared under wake disturbance. The baseline controller, which generates velocity, heading and altitude commands for the autopilot, is designed using backstepping technique without taking the wake effects into account. The design yields a controller with proportional action on position error components along with other terms. The augmented controller is the baseline controller, whose command generation is supplemented with the outputs of a disturbance-estimating filter. The baseline controller already exhibits a stable behavior at the sweet spot, with steady-state relative position errors in longitudinal and vertical components. The steady-state errors are eliminated with the use of the augmented controller. An alternative point of view toward the identification of the wake effects by the follower aircraft is presented by Pollini et al. [42]. They investigate, whether a neural-network-based wake vortex estimation can be used for the sole means of providing the relative position information to the formation flight controller.

Apart from the disturbance rejection and robustness aspects of formation controller design, which are outlined above, studies are also available which apply nonlinear control techniques to formation flight controller design. Studies carried out at West Virginia University involve design, implementation and flight tests of a

nonlinear-dynamical-inversion-based (NLDI) formation flight controller [49, 54]. The dynamical inversion is applied to the kinematic equations defining the relative motion of the leader and the follower aircraft on the horizontal plane. Based on this inversion, throttle command, and a bank angle command for the follower's autopilot are calculated. The flight demonstration of this nonlinear formation control approach is performed with small unmanned aircraft of about two-meter wingspan. Another application of the NLDI-based formation flight control is designed by You and Shim [59] and flight tested with unmanned airplanes of half-a-meter wingspan.

1.4.2 Acquisition of Relative Position Information

In a leader-follower formation flight, the follower aircraft positions itself and performs station keeping relative to the leader. In order to accomplish this task, the follower aircraft needs to know its states with respect to those of the leader aircraft. Based on the existing literature, this section discusses the means by which the follower aircraft acquire the state information with respect to the leader aircraft, particularly the relative position information.

The mostly-used information sources for follower's acquisition of the leader's relative position data are GPS [3, 49, 52–54, 59, 60, 62, 65, 71, 93], inertial navigation systems [3, 49, 52, 53, 59, 65], and computer vision [65, 67, 81, 94]. In some approaches further sensors, such as air data sensors and magnetometers [65], are utilized in order to diversify the leader information sources. Alternative sensors, such as radio-frequency-based ranging equipment [95], are also investigated for use in formation flight. In various approaches the sensor measurements are fused using state estimators such as extended Kalman filter [77, 96], unscented Kalman filter [65], and complementary filter [3]. These sensor fusion approaches utilize the GPS [3, 59, 93], or both GPS and computer vision [65, 77] for correction of the state estimation. Therefore the accuracy provided by these sensors is the main contributor to the overall accuracy of the sensor fusion.

If the computer vision is to be used for obtaining the leader's flight data, monocular cameras are installed on the follower aircraft [58, 65, 67, 81, 94, 97], which capture the images of the leader aircraft. Use of binocular cameras are also presented within the context of airborne aircraft-to-aircraft position estimation [98]. The images captured by the cameras are evaluated by the image processing algorithms in order to identify the leader aircraft based on its shape [58, 67, 97] or with the help of special markers placed on it [65, 81, 94, 98]. The relative position or the pose of the leader aircraft are then extracted with respect to the follower aircraft, by application of geometrical rules to the identified image of the leader aircraft.

Unlike the computer vision, which requires installment of cameras on the follower aircraft, the sensors such as GPS, INS, air data sensors, and magnetometers, need to be placed on the leader aircraft in order to measure its flight data. The flight

data, which are obtained by these sensors, then need to be transferred to the follower aircraft. In order to fulfill this task, the common approach is to install radio antennas and modems on the leader and the follower aircraft in order to set up an inter-aircraft wireless data link. The flight data of the leader are sent to the follower aircraft by means of this wireless data link [3, 49, 52, 53, 59, 65].

The global positioning system is the most widely-used sensor in formation flight applications from which the inter-aircraft relative position information can be obtained. Different methods exist, by which the relative position of two separate GPS receivers can be calculated. In the formation flight demonstrations with small unmanned aircraft, position solutions of the GPS receivers, which are expressed in an earth-fixed reference frame are used for relative position calculation. An example is the work by Gu et al. [99, 100], in which the leader aircraft sends its GPS-based position to the follower aircraft through a wireless data link. In order to calculate the relative position, the follower aircraft then subtracts the leader's GPS-based position from its own GPS-based position.

In the above example, identical GPS receivers are used on both leader and follower aircraft [100]. This increases the probability that both receivers use the same satellite constellation for their own position calculation [71]. If two GPS receivers concurrently track the same satellite, the corresponding measurements of the two receivers will have the same satellite-related errors [101]. Furthermore, since the distance between the two GPS receivers are very small in a formation flight as compared to the satellite-to-receiver distances, the satellite signals arrive the GPS receivers passing through the same volume of the atmosphere. This yields similar atmosphere-related error values in the position measurements of both GPS receivers [70]. Hence, subtraction of the absolute position measurements of the two receivers cancel the common errors, yielding a more accurate relative position measurement as compared to the absolute position measurements of individual receivers. Ground tests were carried out by Kilic and Meiboom [70, Section III.A] in order to find out the error of the relative position measurement, obtained by the method outlined above. Based on the test data exceeding a duration of ten minutes, three dimensional, three-sigma position error of about 3.6 meters was observed. This value matches with the positioning accuracy of the pseudorange-based differential GPS, in which position errors from submeter-level up to 5 meters can be obtained [101].

A more advanced differential GPS positioning, which enables the extraction of relative position measurements from GPS receivers in centimeter-level accuracy, is called real time kinematic (RTK) GPS positioning. In this method, instead of the pseudorange measurements, the numbers of the cycles of the GPS satellites' carrier signals are used [101]. The method requires a communication link between the receivers, in order to transmit the measurements among the receivers [101]. The GPS receivers can have control on the selection of the satellites that they track, in order to use the measurements from the common satellites [71]. With the two GPS receivers

tracking the common satellite constellation, a relative position accuracy of about two to five centimeters can be reached [101].

The use of RTK GPS positioning method in the formation flight has been investigated and demonstrated. Comstock [102], Spinelli [93], and Williamson et al. [96] present relative navigation solutions for automated formation flight, which utilize the RTK GPS relative positioning. Centimeter-level-accurate relative position measurements are obtained at sampling rates up to 20 Hz, both with [93] and without [102] the use of inertial measurement units. These types of relative navigation solutions are further utilized in the aerial refueling demonstrations of Ross et al. [52] and Dibley et al. [68], as the main means of obtaining aircraft-to-aircraft relative position information.

There are possible issues with GPS-based relative position acquisition techniques, which can effect the quality of the relative position information. Multipath, which occurs if the satellite signal arrives the receiver through different paths, can deteriorate the accuracy of the position estimation [101]. Objects around the GPS receiver's antenna, such as other aircraft in a formation flight, can cause the satellite signals to reflect, thus forming the multipath. Further causes for flaws in relative position information are GPS receivers' change of satellites, or tracking of different satellite constellations [71]. GPS signal blockage is another problem, which may take place during formation flight applications. If the leader aircraft has a clear view of the satellites, but the follower's view of the satellites is blocked by the leader, the relative position measurements are likely to be impacted. In this context Khanafseh et al. [103, 104] present a sky blockage model for a receiver aircraft during an aerial refueling mission. Particular reference is given to the turning maneuvers of the aerial refueling missions, in which severe satellite outages are likely [103]. In this respect, the use of multiple GPS receivers and antennas on the receiver aircraft is recommended as a means of enhancing the view of the sky [103]. Further issues may arise with GPS, which can have potential impact on relative positioning. These are its vulnerabilities against jamming and spoofing in unfriendly environments, and dilution of precision [105].

Regardless of the employed sensors and navigation solutions, the transfer of leader flight data via wireless data link may also cause additional issues. The wireless communication may be lost at times [3, 71, 93], causing spikes at relative position information [71, 93] or interruptions on the flow of information to the follower aircraft. The communication system also introduces extra delays on the flow of information [70], in addition to those introduced by the sensors [71] and computational processing. In hostile environments, jamming can be a potential disturbance on the wireless information transfer among the aircraft.

An advantage of using computer vision on the follower aircraft for relative position estimation is that, it does not require a wireless data link between the leader and the follower aircraft. Therefore, the data-link-specific problems discussed above can be

avoided. However, dropouts of the observation of tracked object, i.e. the leader aircraft, can be the case in computer vision. This can cause the interruption of the flow of relative position information to the follower aircraft's formation controller. Such observation dropouts may take place due to the occlusion of the tracked object by the fog and clouds [105], ambient lighting conditions, or if the tracked object is outside of the camera's field of view [72]. The situations such as partial visibility of the tracked object [106] or dropout of one or more markers attached to the object [107] can deteriorate the accuracy of the position estimation. Blurry images due to motion [105] and the change of relative orientation between the camera and the tracked object [108] are the other factors, which may cause observation dropouts or erroneous localization.

1.4.3 Formation Flight Aerodynamics

The research regarding the aerodynamic aspects of formation flight concentrate mostly on modeling of the leader's wake vortex effects on follower aircraft for use in simulation environments, as well as aerodynamic benefits enabled by formation flight.

For the modeling of the trailing or wake vortices, horseshoe wake vortex approximations [13, 109] are used. The approaches involve the placement of a single horseshoe vortex [41, 110] or multiple superposed [15] horseshoe vortices spanning on the wing [41, 110], or both on the wing and horizontal stabilizer [15] of the aircraft. Applying the Biot-Savart law [13, 109] on the horseshoe vortices of known strength, these methods provide estimations of the induced air velocity components at any arbitrary point relative to the horseshoe vortices. As an alternative approach, the vortex lattice method [109] is used, in which the aircraft lifting surfaces are partitioned into panels and horseshoe vortices are placed on each panel. In this method, the strengths of the horseshoe vortices are not not known initially. They are calculated at specific control points, by imposing the condition that the flow of air normal to the lifting surface equals zero [109]. Following this approach, Saban and Whidborne [11] partition the aircraft lifting surfaces into spanwise panels and place horseshoe vortices on each panel. After the calculation of the vortex strengths, Biot-Savart law enables the calculation of the induced velocity components at arbitrary points around the lifting surfaces. Being able to calculate the induced velocity components at arbitrary points, in order to estimate the overall wake-induced effects on the follower aircraft, the point-wise induced velocity components are then averaged over the surfaces of the follower aircraft [11, 41, 110]. Different averaging approaches are presented in the work by Dogan et al. [110].

Another method for obtaining a wake vortex model for implementation in simulations is the use of lookup tables, in which the wake effect data obtained from computational fluid dynamics (CFD) methods, measurements from wind tunnel, or flight tests are collected for use in simulations [11]. Although this is an accurate

method, it is not flexible in that, the obtained data are specific to aircraft and flight condition [11]. An example for flight-test-based wake effect estimation is the work by Hansen and Cobleigh [111], in which two McDonnell Douglas F/A-18 aircraft are used as leader and follower aircraft. Based on flight tests, in which the follower aircraft is flown at different locations relative to the leader aircraft, a relative-position-dependent mapping of wake-induced moment and side force effects on the follower aircraft is presented. A CFD-based wake vortex modeling is carried out by Spence et al. [112] in order to create lookup tables to be implemented into a simulation environment within the context of a wake vortex encounter scenario.

Apart from the modeling of the wake vortex effects, studies also exist, which concentrate on the aerodynamic benefits attainable from the wake of another aircraft. In this respect, simulation-based studies by Okolo et al. [14, 20, 21] provide estimations of the sweet spot location for a follower aircraft flying in the wake of a leader. Their 2012 study [20] uses simulations utilizing Boeing KC-135 leader and follower aircraft models. In trimmed state maximum thrust reduction is reached by the follower aircraft, if it follows the leader at the same altitude and at a lateral separation of about 0.83 wingspans. In a later study [21], the effect of follower aircraft size on the sweet spot location is investigated. It has been found out that, if the follower aircraft is larger than the leader, the minimum thrust point is located further apart from the leader laterally. This change is attributed to the increase of rolling moment disturbance on the follower aircraft with its increasing size. The roll disturbance increase causes a higher trim drag, which then requires higher trust during the trim for compensation [21]. There are also studies, which propose the in-flight determination of the sweet spot, based on real-time information of the flight parameters such as rolling moment, fuel consumption and throttle setting [113, 114]. The effects of leader's geometric parameters, such as wing incidence, aspect ratio, dihedral, and taper ratio, on the aerodynamic efficiency of formation flight is also available in a separate, CFD-simulation-based study [115].

Studies also exist, which investigate the effects of the leader aircraft's wake flow field on aeroelastic follower aircraft. In this respect, a simulation-based stability analysis framework of a flexible *high altitude, long endurance* (HALE) type of follower aircraft within the wake flowfield of a Boeing KC-135 leader aircraft is presented by Devuono and Shearer [116]. Another study is presented by Hanson [117], in which elastic twist deformations of straight, slender wings are considered under aerodynamic effects of drag-reduction-oriented formation flight. The upwash from the wake is reported to cause the follower wing section close to the vortex core to twist in the leading-edge-up sense. Despite having a higher trim drag, a greater overall drag reduction due to formation flight is observed on the flexible wing with respect to a rigid one.

1.5 Organization

This work is organized as follows. Chapter 2 states the general flight-dynamical assumptions and axis systems used in this work, as well as introduces the notation style. Chapter 3 presents the theory, which are applied in this work. In Chapter 4, the details of flight-dynamical models and the nonlinear simulations of the leader and follower aircraft are presented. In Chapter 5, the autopilots and the guidance algorithms of the leader and the follower aircraft are given. Chapter 6 presents the derivation and the characteristics of the aerodynamic disturbance acting on the follower aircraft, induced by the leader's wake vortices. The answers to the research question formulated in Section 1.3 are provided in chapters 7 to 9. Chapter 7 explains the design of the simulation-based experiments and presents the simulation results along with corresponding discussions. Chapter 8 explains the derivation of the system-theoretical expressions, which approximate the results obtained from the simulation. Finally, Chapter 9 summarizes the main conclusions and presents directions for future work.

Chapter 2

Flight-Dynamical Background and Assumptions

This chapter states the general flight dynamical assumptions followed in this work. The flight dynamical background for the subsequent chapters, as well as the notation style and the naming conventions[1] are also stated.

2.1 Flight Dynamical Assumptions

The general flight dynamical assumptions, that this work follows, are stated below.

1. The earth is assumed to be flat and non-rotating. For the transonic and subsonic speed regimes, the loss of accuracy due to this assumption is negligibly small [118].

2. The aircraft are assumed to be rigid. This is a valid assumption, as long as the elastic movements are not deliberately agitated by the aircraft control commands and the natural frequencies of the elastic motion of the aircraft parts are considerably higher than the natural frequencies of the rigid body motion [118].

3. The aircraft mass and center of gravity locations are assumed to be constant, neglecting the effects such as the fuel burn. The loss of reality due to this assumption will be negligibly small for short durations of flight simulation.

2.2 Axis Systems and Right Hand Rule

In this work, three dimensional, *right-handed axis systems* are used. Right-handed axis systems obey the *right hand rule*, which is demonstrated in figure 2.1. As shown,

[1] Most of the notation style and the naming conventions that are used in this work follow those of Flight System Dynamics lecture held by Florian Holzapfel at the Technical University of Munich (personal communication, October 2009 - February 2010).

for the right-handed axis systems if the palm of the right hand is aligned with the x-axis and the fingers are curled toward the y-axis, the direction of the thumb will give the positive direction of the z-axis.

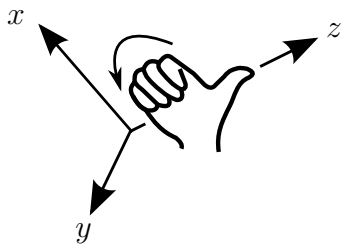

Figure 2.1: Right hand rule and a right-handed axis system.

Unless otherwise stated, the right hand rule also determines the sign conventions for rotations, or the rotational quantities such as moment and angular velocity. If the thumb of the right hand is aligned with the positive direction of an axis and the fingers are curled, the curl of the fingers give the positive direction for the rotation about that axis or the rotational quantities that are defined with respect to that axis. A rotation in the opposite direction is a negative rotation and represents the negative direction for the rotational quantities.

2.3 Reference Frames and Their Conversions

This section gives the reference frames that are used in this work, as well as the geometrical relations between them.

2.3.1 North-East-Down (NED) Frame

This reference frame is defined by a right-handed axis system. The x and y axes of the frame point to the geographical north pole and the east respectively. Both axes remain parallel to the local geoid plane. The z-axis of the frame points downwards and is perpendicular to the local geoid plane. The x, y and z axes of this reference frame are labeled as N, E and D in the figures.

There are two types of this reference frame depending on the point its origin is located. If the origin of the reference frame is fixed to an arbitrary reference point on the surface of the earth, then the reference frame is called the *local* NED frame. If the origin of the reference frame is fixed to the aircraft reference point, for instance the aircraft center of gravity or any other point that moves with the aircraft, then the reference frame is called *vehicle-carried* NED frame. In this case the reference frame translates along with the vehicle. The local and vehicle-carried NED frames are referred to by the symbol 0.

Since the earth is assumed to be flat and non-rotating, all earth-fixed reference frames can be treated as inertial reference frames [118]. Therefore, this work treats the local NED reference frame as inertial reference frame. The local NED frame is used also as the default reference frame with respect to which the positions and velocities are defined, unless otherwise stated.

2.3.2 Kinematic Frame

This reference frame is defined by a right-handed axis system, whose origin is fixed to the aircraft reference point. The x-axis of this reference frame is aligned with and points to the same direction as the ground velocity vector of the aircraft. The y-axis of the kinematic frame is perpendicular to the x-axis, remain parallel to the local geoid plane, and points to the right with respect to the x-axis. Finally the z-axis of the kinematic frame completes the right-handed axis system, that is, it points downward if the ground velocity lies in the horizontal plane. This reference frame is referred to by the symbol K. The axes of this reference frame is labeled as x_K, y_K and z_K in the figures.

2.3.3 Body-Fixed Frame

This reference frame is defined by a right-handed axis system, whose axes are fixed to the aircraft's body. The origin of this reference frame is fixed to the aircraft reference point. The x-axis of this reference frame points to the aircraft nose, in forward direction. The y-axis is perpendicular to the x-axis and points to the right side of the aircraft body. Finally the z-axis is perpendicular to the xy-plane and points downward side of the aircraft fuselage. This reference frame is referred to by the symbol B. In the figures, the axes of this reference frame is labeled as x_B, y_B and z_B. For simplicity, this reference frame is also referred to as *body frame*.

2.3.4 Aerodynamic Frame

Aerodynamic frame is defined by a right-handed axis system, whose origin is fixed to the aircraft, at its reference point. Its x-axis is aligned with and points to the same direction as the velocity vector of the aircraft with respect to the surrounding air. The z-axis is in the symmetry plane of the aircraft, pointing downwards if the x-axis lies in the horizontal plane. The y-axis points to the right side of the aircraft, completing the right-handed axis system. This reference frame is referred to by the letter A. The axes of this reference frame are labeled as x_A, y_A and z_A.

2.3.5 Angular Relations Between Different Reference Frames

2.3.5.1 Attitude Angles

Figure 2.2 shows the angular relations between the reference frames described above. The angles are shown with their directions, along which they are defined positive. The angles ϕ, θ and ψ defines the orientation (attitude) of the aircraft with respect to the local NED frame. The *bank angle* ϕ is defined as the angle between the aircraft's body-frame y-axis and the horizontal plane. A positive bank angle is obtained if the aircraft rolls to the right. The *pitch angle* θ is the angle between the body-frame x-axis and the horizontal plane. A positive pitch angle is obtained in the direction of the aircraft's pitch up motion. The *azimuth angle* ψ is the angle between the local northern direction and the projection of the body frame x-axis on the horizontal plane. This angle shows the direction that the nose of the aircraft is pointing to. If the aircraft yaws to the right, a positive incrementation on the azimuth angle is obtained. The intervals, in which the attitude angles are defined in this work, are given below.

$$-180^\circ \leq \phi \leq 180^\circ \quad -90^\circ \leq \theta \leq 90^\circ \quad -180^\circ \leq \psi \leq 180^\circ \tag{2.1}$$

2.3.5.2 Flight Path and Course Angles

In order to describe the motion of the aircraft's center of gravity with respect to the local NED frame, the angles γ and χ are used. The *flight path angle* γ is the angle between the local horizontal and the velocity vector of the aircraft with respect to the local NED frame, i.e., the ground velocity. A positive flight path angle is present during a climbing flight. The *course angle* χ describes the direction that the aircraft is traveling to. It is the angle between the x-axis of the local NED frame and the projection of the ground velocity vector of the aircraft on horizontal plane. If the aircraft flies a clockwise circle pattern on the horizontal plane seen from above, the course angle will be continuously changing in the positive sense. The intervals, in which the flight path and course angles are defined in this work, are presented below.

$$-90^\circ \leq \gamma \leq 90^\circ \quad -180^\circ \leq \chi \leq 180^\circ \tag{2.2}$$

Although the definitional ranges of the roll, pitch and flight path angles are as given in eqs. (2.1) and (2.2), in the simulations used in this work, the magnitudes of the angles ϕ, θ and γ get values, which are well below 90°.

2.3.5.3 Aerodynamic Angles

For six-degree-of-freedom, rigid-body aircraft equations of motion the aerodynamic forces and moments acting on the aircraft are the functions of the aircraft's orientation

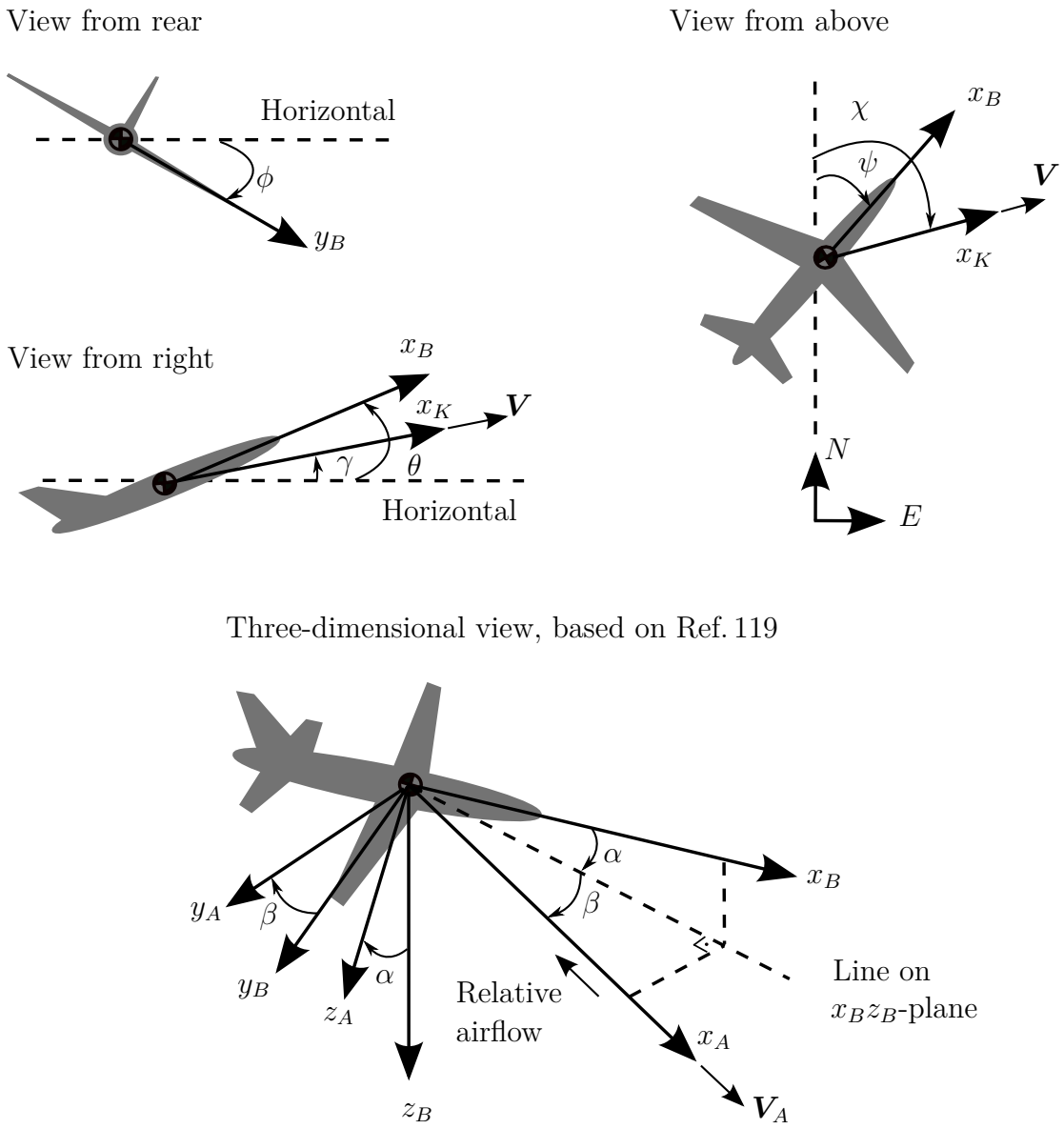

Figure 2.2: Angular relations between the NED, body-fixed, kinematic and aerodynamic reference frames. For each two-dimensional view the angles, which are not shown, are considered to be zero.

with respect to the airflow around it [119]. The angles that define this orientation are called *aerodynamic angles*, which are the *angle of attack* α, and the *angle of sideslip* β. Equation (2.3) defines the *aerodynamic velocity* $\boldsymbol{V}_A$, the velocity of the aircraft, with respect to the surrounding air. In eq. (2.3), $\boldsymbol{V}$ is the ground velocity - i.e., the velocity of the aircraft with respect to the local inertial reference frame, and $\boldsymbol{V}_W$ is the wind velocity - i.e., the velocity of the air with respect to the local inertial reference frame.

$$\boldsymbol{V}_A = \boldsymbol{V} - \boldsymbol{V}_W \tag{2.3}$$

The aerodynamic angles are shown in Figure 2.2. As shown in the figure the angles α and β are defined as the angles between the aircraft's body-frame x-axis and aerodynamic velocity vector $\boldsymbol{V}_A$. The signs of α and β are defined positive in the direction shown in Figure 2.2.

2.3.6 Conversion Between Different Reference Frames

Positive and negative rotations of the axis systems are defined by the right hand rule (Section 2.2).

The transformation matrix from NED frame to the kinematic frame is given by eq. (2.4). It can be obtained if a sequence of positive rotations is applied to the NED-frame z-axis and the intermediate y-axis through the angles χ and γ sequentially.

$$\boldsymbol{T}_{K0} = \begin{bmatrix} \cos\chi\cos\gamma & \sin\chi\cos\gamma & -\sin\gamma \\ -\sin\chi & \cos\chi & 0 \\ \cos\chi\sin\gamma & \sin\chi\sin\gamma & \cos\gamma \end{bmatrix} \tag{2.4}$$

Similarly, applying the sequence of positive ψ, θ, ϕ rotations to the NED-frame on the axes of z, and then intermediate y and x axes respectively, the transformation matrix from NED frame to the body-fixed frame can be obtained. It is given by eq. (2.5).

$$\boldsymbol{T}_{B0} = \begin{bmatrix} \cos\psi\cos\theta & \sin\psi\cos\theta & -\sin\theta \\ \cos\psi\sin\theta\sin\phi - \sin\psi\cos\phi & \sin\psi\sin\theta\sin\phi + \cos\psi\cos\phi & \cos\theta\sin\phi \\ \cos\psi\sin\theta\cos\phi + \sin\psi\sin\phi & \sin\psi\sin\theta\cos\phi - \cos\psi\sin\phi & \cos\theta\cos\phi \end{bmatrix} \tag{2.5}$$

Applying a negative rotation about the y-axis of the body-fixed frame with an amount of α, and then a positive rotation about the new z-axis with an amount of β, the transformation matrix from body-fixed frame to aerodynamic frame can be obtained. The transformation matrix is given by eq. (2.6).

$$\boldsymbol{T}_{AB} = \begin{bmatrix} \cos\alpha\cos\beta & \sin\beta & \sin\alpha\cos\beta \\ -\cos\alpha\sin\beta & \cos\beta & -\sin\alpha\sin\beta \\ -\sin\alpha & 0 & \cos\alpha \end{bmatrix} \tag{2.6}$$

Since the transformation matrices are orthogonal, their inverses equal their transposes [118]. Therefore, as given in eqs. (2.7) to (2.9), the transformation matrices from kinematic frame to the NED frame ($\boldsymbol{T}_{0K}$), from body-fixed frame to the NED frame ($\boldsymbol{T}_{0B}$), and the transformation matrix from aerodynamic frame to the body

frame ($\boldsymbol{T}_{BA}$) are the transposes of the transformation matrices given in eqs. (2.4) to (2.6), respectively.

$$\boldsymbol{T}_{0K} = \boldsymbol{T}'_{K0} \tag{2.7}$$

$$\boldsymbol{T}_{0B} = \boldsymbol{T}'_{B0} \tag{2.8}$$

$$\boldsymbol{T}_{BA} = \boldsymbol{T}'_{AB} \tag{2.9}$$

With the knowledge of the transformation matrices $\boldsymbol{T}_{0B}$ and $\boldsymbol{T}_{K0}$, the transformation matrix from body-fixed frame to the kinematic frame can be written directly as the product of the two in the multiplication order given in eq. (2.10).

$$\boldsymbol{T}_{KB} = \boldsymbol{T}_{K0}\boldsymbol{T}_{0B} \tag{2.10}$$

2.4 Vector Notation

The vector notation followed in this work is illustrated by the examples given in this section.

2.4.1 Position Vector Notation

The position of leader aircraft reference point L, with respect to the origin of the local NED frame 0 (i.e., local reference point), with components expressed in leader body-fixed reference frame B_L can be written as $\left(\boldsymbol{r}^{0L}\right)_{B_L}$. Since the local NED frame is used as the default inertial reference frame, this vector is simply written as $\left(\boldsymbol{r}^{L}\right)_{B_L}$, without explicitly referring to the local NED reference frame 0.

Similarly, the position of the follower aircraft reference point F, with respect to the leader aircraft reference point L, with components expressed in the kinematic frame of the leader aircraft K_L can be written as $\left(\boldsymbol{r}^{LF}\right)_{K_L}$.

Equation (2.11) illustrates the component notation of the follower's relative position vector with respect to the leader, $\left(\boldsymbol{r}^{LF}\right)_{K_L}$. The components of the position vectors are denoted by x, y and z respectively, expressing the position components along the x, y and z axes of the respective reference frame. In some occasions the components of the vector can be individually mentioned, i.e., without being shown in vector parenthesis along with other vector components. In such cases, the vector components can be shown with or without the corresponding reference frame, i.e., as $\left(x^{LF}\right)_{K_L}$ or x^{LF}, depending on the context and clarity. This applies also to other vector entities.

$$\left(\boldsymbol{r}^{LF}\right)_{K_L} = \begin{bmatrix} x^{LF} \\ y^{LF} \\ z^{LF} \end{bmatrix}_{K_L} \tag{2.11}$$

Commas can be used for separating different superscripts for clarity. For instance, the x-component of the position of the aircraft center of gravity cg with respect to the horizontal stabilizer's neutral point npt is denoted by $x^{npt,cg}$.

2.4.2 Velocity Vector Notation

The ground velocity of the follower aircraft reference point F, with respect to the leader aircraft reference point L, with components expressed in the kinematic frame of the leader aircraft K_L can be written as $\left(\boldsymbol{V}_g^{LF}\right)_{K_L}$. The subscript g denotes that the velocities of the both aircraft are with respect to the ground, i.e., with respect to the local NED reference frame. The subscript g is however omitted in the notation followed in this work, assuming that the term velocity is ground velocity, unless otherwise defined. Therefore $\left(\boldsymbol{V}^{LF}\right)_{K_L} = \left(\boldsymbol{V}_g^{LF}\right)_{K_L}$.

Velocity vector components are represented by u, v and w, which correspond to the x, y and z axes of the respective reference frame. Equation (2.12) gives an example, showing the ground velocity of the follower aircraft F, with respect to the leader aircraft L, with the velocity components expressed in the leader's kinematic frame, K_L.

$$\left(\boldsymbol{V}^{LF}\right)_{K_L} = \begin{bmatrix} u^{LF} \\ v^{LF} \\ w^{LF} \end{bmatrix}_{K_L} \tag{2.12}$$

2.4.3 Angular Velocity Vector Notation

The angular velocity vectors are denoted by $\boldsymbol{\Omega}$. For instance, the angular velocity of the aircraft body-fixed frame with respect to the vehicle-carried NED frame, whose components are decomposed on the body-fixed frame, can be written as $\left(\boldsymbol{\Omega}^{0B}\right)_B$. The components of the angular velocity vector are represented by p, q and r, as illustrated by eq. (2.13). For this specific example, which describes the body angular rates of the aircraft, the superscripts over the angular velocity components are omitted.

$$\left(\boldsymbol{\Omega}^{0B}\right)_B = \begin{bmatrix} p^{0B} \\ q^{0B} \\ r^{0B} \end{bmatrix}_B = \begin{bmatrix} p \\ q \\ r \end{bmatrix}_B \tag{2.13}$$

Subscripts are used in order to refer to different types of angular velocities, such as the use of the subscript W for referring to the angular wind velocity.

2.4.4 Force Vector Notation

The force vectors are denoted by $\boldsymbol{F}$. The type of the force is shown by the subscripts. For instance, aerodynamic force, whose components are expressed in body-fixed reference frame is shown by $(\boldsymbol{F}_A)_B$. The components of the force vectors are shown by X, Y and Z, as illustrated by eq. (2.14).

$$(\boldsymbol{F}_A)_B = \begin{bmatrix} X_A \\ Y_A \\ Z_A \end{bmatrix}_B \tag{2.14}$$

2.4.5 Moment Vector Notation

Moment vectors are shown by $\boldsymbol{M}$. Two subscripts can be used in moment notation, with the first subscript showing the type of the moment and the second one showing the action point of the moment. For instance, the propulsive (subscript P) moment, acting on the center of the gravity (subscript, cg) of the aircraft, whose components are expressed in the aircraft body-fixed frame, can be written as $(\boldsymbol{M}_{P,cg})_B$. For simplicity, one of the subscripts can be omitted depending on the contextual clarity.

The moment components are denoted by the letters l, m and n, corresponding to the x, y and z axes of the respective reference frame. Equation (2.15) shows the propulsive moment $(\boldsymbol{M}_{P,cg})_B$ with its components.

$$(\boldsymbol{M}_{P,cg})_B = \begin{bmatrix} l_{P,cg} \\ m_{P,cg} \\ n_{P,cg} \end{bmatrix}_B \tag{2.15}$$

Chapter 3

Theoretical Background

This chapter summarizes the theoretical foundations, which are applied in this work. The first section of the chapter briefly presents the three-sigma rule, which is used in chapters 1 and 7. The second section outlines dynamical scaling and describes its use in this work. Finally, the third section of the chapter states relevant definitions from linear systems theory, which are applied in Chapter 8.

3.1 Three-Sigma Rule

A data set of arbitrary probability distribution is considered. The data set has the standard deviation σ (sigma) and the mean μ. The three-sigma rule states that, nearly all the samples in the data set are located within an interval defined by the boundaries $\mu - 3\sigma$ and $\mu + 3\sigma$. The statement, "nearly all the samples", can be described more specifically. According to Chebyshev's rule, which can be applied to data sets of any probability distribution, a minimum of 89% of the samples lie within an interval of three standard deviations on both sides of the mean. According to empirical rule, which assumes a data set of normal probability distribution, 99.7% of the samples lie within the aforementioned interval [120].

The three-sigma rule is applied in this work in order to find an approximation of the maximum value of a data set, using solely the knowledge of the standard deviation and assuming zero mean. That is, the maximum value within the data set is approximated in absolute terms as 3σ.

3.2 Dynamic Scaling

3.2.1 Background and Definitions

In aircraft design applications, use of lower-scale models of the designed aircraft for certain experimental work is a common procedure due to costs and safety reasons

[121, 122]. However, in order to apply the experiment results of the model aircraft to the full-scale aircraft, certain similarity relations must exist between the two aircraft. Depending on the type of similarity demanded, these relations may include similarity in Reynolds number, Froude number, Mach number or further similarity measures, in addition to the most basic geometric and angle of attack similarities [123]. Similarity in any of these parameters means that, the parameter has the same value for both the lower-scale and the full-scale aircraft. Nevertheless, in most cases, it is not possible to accomplish similarity in all these similarity measures simultaneously [124]. Hence, similarity is realized only in certain parameters [123], which are the most relevant to the phenomena under investigation. For instance, if the compressibility effects are the main focus of the investigation, the lower-scale model and its test conditions are adjusted to match the Mach number of the full-scale aircraft [125].

The *dynamic similarity* is the type of similarity, under which the forces and the motion of the dynamically-scaled lower-scale aircraft simulate those of the full-scale aircraft. In order to achieve this similarity, the lower-scale aircraft is produced so that, its geometry and mass distribution is the same as those of the full-scale aircraft. Additionally, it is required that the following force ratios are the same for both aircraft [124].

$$Froude\,Number = \frac{Vehicle\,inertial\,force}{Vehicle\,weight} = \frac{mV^2/l}{W} = \frac{mV^2/l}{mg} = \frac{V^2}{gl} \tag{3.1}$$

$$Mass\,ratio = \frac{Vehicle\,inertial\,force}{Aerodynamic\,force} = \frac{mV^2/l}{\rho V^2 l^2} = \frac{m}{\rho l^3} = \frac{W}{\rho g l^3} \tag{3.2}$$

In eqs. (3.1) and (3.2) the terms m, W, and V are the mass, weight, and the speed of the flight vehicle respectively. The terms ρ and g are the air density and the gravitational acceleration at the altitude of interest. The term l is the characteristic length of the flight vehicle.

Based on the definitions given above, the term *dynamical scaling* is used for referring to obtaining a scaled aircraft from another aircraft by complying with the dynamical similarity requirements stated above.

3.2.2 Dynamic Scaling Coefficients

The scale factors for the quantities, which are used in this work, are derived below. Assuming that:

1. An aircraft, *aircraft-2*, is the scaled version of an existing aircraft, *aircraft-1*, with the same geometry,

2. The aircraft dimensions, as well as the densities and gravitational accelerations belonging to each aircraft's flight conditions are known,

then the following relations are readily available.

$$R_l = \frac{l_2}{l_1} \tag{3.3}$$

$$R_\rho = \frac{\rho_2}{\rho_1} \tag{3.4}$$

$$R_g = \frac{g_2}{g_1} \tag{3.5}$$

Adhering to the notation of Gainer and Hoffman [124], the terms R_l, R_ρ and R_g are the *length, density* and *gravity scale factors*, respectively. The term *scale factor* in general is defined as the ratio of any quantity belonging to aircraft-2 to the same quantity of aircraft-1.

Starting from the assumptions given above, using the dynamical scaling requirements stated in previous section, as well as the scaling factors given in eqs. (3.3) to (3.5), the scaling factors for further quantities can be written as shown below.

Since both aircraft are of the same geometry, from eq. (3.3) the *area and volume scale factors* of the aircraft can be written as R_l^2 and R_l^3, respectively.

Since the Froude number must have the same value for both dynamically-scaled aircraft, eq. (3.6) can be written.

$$\frac{V_1^2}{g_1\, l_1} = \frac{V_2^2}{g_2\, l_2} \tag{3.6}$$

Inserting eqs. (3.3) and (3.5) and rearranging the terms, the *velocity scale factor* can be written as given in eq. (3.7).

$$\frac{V_2}{V_1} = \sqrt{R_g}\sqrt{R_l} \tag{3.7}$$

Equating the mass ratios (eq. (3.2)) of both aircraft, eqs. (3.8) and (3.9) are obtained.

$$\frac{m_1}{\rho_1\, l_1^3} = \frac{m_2}{\rho_2\, l_2^3} \tag{3.8}$$

$$\frac{W_1}{\rho_1\, g_1\, l_1^3} = \frac{W_2}{\rho_2\, g_2\, l_2^3} \tag{3.9}$$

Inserting the scale factors given in eqs. (3.3) to (3.5) and rearranging, the *mass and weight scale factors* can be written as given in eqs. (3.10) and (3.11). Since the

weight is a force quantity, the weight scale factor is also the *force scale factor*.

$$\frac{m_2}{m_1} = R_\rho R_l^3 \tag{3.10}$$

$$\frac{W_2}{W_1} = R_\rho R_g R_l^3 \tag{3.11}$$

Looking at the moment of inertia formulas of rigid bodies [126], it can be seen that the moment of inertia I is proportional to the length and mass of the object, such that $I \propto ml^2$. Based on this, the moment of inertia ratio of the two aircraft about same axes can be written as given in eq. (3.12).

$$\frac{I_2}{I_1} = \frac{m_2}{m_1}\left(\frac{l_2}{l_1}\right)^2 \tag{3.12}$$

Placing the mass and length scale factors into eq. (3.12), the *moment of inertia scale factor* can be written as stated in eq. (3.13).

$$\frac{I_2}{I_1} = R_\rho R_l^5 \tag{3.13}$$

The *angular velocity scale factor* can be derived based on the relation between the translational and angular velocity. Considering an aerodynamic control surface of the aircraft of chord l as an example, the translational velocity of the surface's tip under the angular velocity ω can be written as $V = \omega l$. Based on this relation, the angular velocity ratios of both aircraft can be written as given in eq. (3.14).

$$\frac{\omega_2}{\omega_1} = \frac{V_2}{V_1}\frac{l_1}{l_2} \tag{3.14}$$

Inserting the velocity and length scale factors into eq. (3.14), the angular velocity scale factor can be written as eq. (3.15).

$$\frac{\omega_2}{\omega_1} = \frac{\sqrt{R_g}}{\sqrt{R_l}} \tag{3.15}$$

Since angle is a dimensionless quantity, the dimension of the angular velocity is the reciprocal of the time. Therefore, using eq. (3.15), the *time scale factor* can be written as given in eq. (3.16).

$$\frac{t_2}{t_1} = \frac{\sqrt{R_l}}{\sqrt{R_g}} \tag{3.16}$$

3.2.3 Using Dynamic Scaling

This work uses simulation in order to answer the research question stated in Section 1.3.3. Keeping the leader and follower aircraft identical, it is also investigated in this work, how the answer to the question varies with different sizes of aircraft. Therefore, two separate simulation sets made up of different scales of aircraft are used. Dynamical scaling is used for generating an aircraft of different scale from one existing aircraft flight dynamical model. Then the simulations are performed with each scale of dynamically-scaled aircraft.

In order to obtain a dynamically-scaled aircraft model from an existing aircraft model, the scaling factors derived in the previous section are used. For calculating a quantity of the derived aircraft from the same quantity of an existing aircraft, the quantity is multiplied with the corresponding scale factor. For instance, eqs. (3.17) and (3.18) show the derivation of the flight velocity and mass of the derived aircraft, aircraft-2 from an existing aircraft, aircraft-1.

$$V_2 = \sqrt{R_g}\sqrt{R_l}V_1 \tag{3.17}$$

$$m_2 = R_\rho R_l^3 m_1 \tag{3.18}$$

3.3 Linear Systems Theory

3.3.1 Transfer Functions

Transfer functions are mathematical models defining the input-output relations of linear, time-invariant dynamical systems with zero initial conditions [127]. They define the ratio of the Laplace transforms of the system's output to the system's input regardless of the type of the input signal acting on the system [127].

First and second-order transfer functions are used in this work for approximation of certain dynamical behavior. Equations (3.19) and (3.20) give the the first and second-order transfer functions of unity steady-state gains, in the form that they are used in this work.

$$G(s) = \frac{Y(s)}{U(s)} = \frac{1}{\tau s + 1} \tag{3.19}$$

$$G(s) = \frac{Y(s)}{U(s)} = \frac{\omega_0^2}{s^2 + 2\zeta\omega_0 s + \omega_0^2} \tag{3.20}$$

In eqs. (3.19) and (3.20), the terms $Y(s)$ and $U(s)$ are the Laplace transforms of the output and the input, where the term s is the Laplace variable. The terms τ, ζ and ω_0 are the time constant, damping ratio and the natural frequency of the

corresponding transfer function, respectively.

As shown in eqs. (3.19) and (3.20), a first-order transfer function can be defined by a single parameter, τ. On the other hand, the second-order transfer functions are defined by two parameters, ζ and ω_0. Therefore, for the sake of simplicity, certain second-order transfer functions are approximated in this work by first-order transfer functions. This is done by writing the time constants of the first-order transfer function in terms of the damping ratio and natural frequency of the second-order transfer functions using the relation given in eq. (3.21). The relation is given by Ogata [127], assuming an underdamped second-order transfer function ($0 < \zeta < 1$).

$$\tau = \frac{1}{\zeta \omega_0} \tag{3.21}$$

Step response curve of the first-order transfer function, which is formed by using eq. (3.21), corresponds to the envelope curves of the step-response of the second-order transfer function [127]. This relation is depicted in figure 3.1.

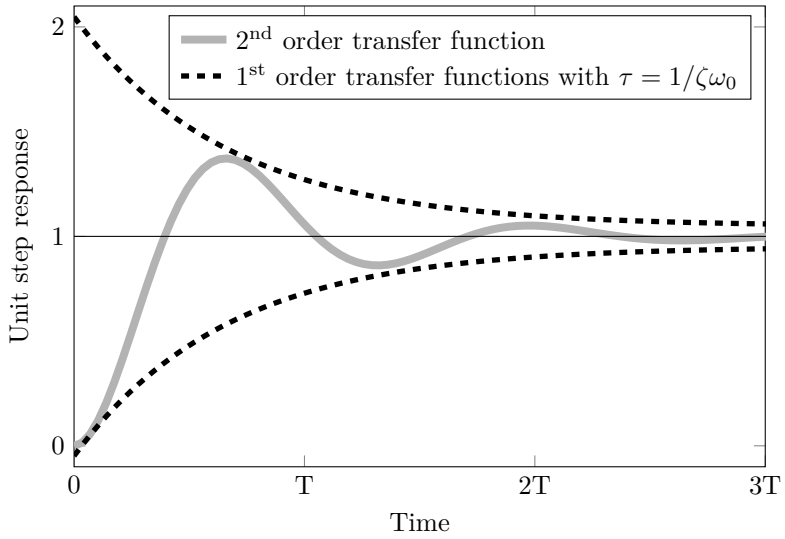

Figure 3.1: Unit step response of a second-order transfer function with envelope curves as first-order transfer function step response curves. The plot was generated based on Ogata [127].

3.3.2 Signals and Systems With Time Delay

A pure time delay with a duration of λ seconds is considered. Based on Franklin et al. [128], the following two expressions regarding the time delay are given.

A delayed time-domain signal $y_d(t)$ can be written in terms of its delay-free counterpart $y(t)$ as given in eq. (3.22).

$$y_d(t) = y(t - \lambda) \tag{3.22}$$

The time delay is represented in frequency domain as $e^{-s\lambda}$. Hence, eq. (3.22) can be written in frequency domain as given in eq. (3.23).

$$Y_d(s) = e^{-s\lambda}Y(s) \tag{3.23}$$

As a system containing time delay, the time-delayed version of the first-order transfer function given in eq. (3.19) is considered. Figure 3.2 shows two block diagrams, the first one representing the delay-free first-order system given by eq. (3.19), and the second one depicting the same system with internal delay on the feedback channel.

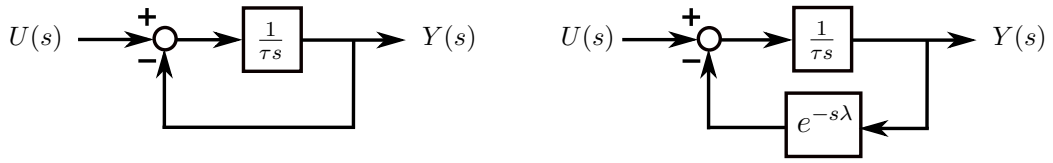

Figure 3.2: Block diagram representations of first order transfer functions without and with internal time delay.

The first-order system with internal delay depicted in figure 3.2 can be written in transfer function form as given in eq. (3.24). This is the type of time-delayed transfer function applied in this work.

$$\frac{Y(s)}{U(s)} = \frac{1}{\tau s + e^{-s\lambda}} \tag{3.24}$$

3.3.3 Frequency Response

Frequency response methods investigate the steady-state responses of linear dynamical systems under sinusoidal input signals, regarding the frequency of the sinusoid as variable [127]. The resulting sinusoidal response of the dynamical system is then quantified in terms of its magnitude and phase with respect to those of the input sinusoid. In this work frequency response magnitude representations of the first order transfer functions are used.

Considering a transfer function under a sinusoidal input signal of frequency ω, the amplitude ratio of the transfer function's steady-state output to its input can be found by replacing the Laplace variable s in the transfer function with the term $j\omega$ and calculating the magnitude of the resulting complex number [127]. Applying this to the first-order transfer function given in eq. (3.19), eq. (3.25) is obtained.

$$|G(jw)| = \left|\frac{Y(j\omega)}{U(j\omega)}\right| = \left|\frac{1}{j\tau\omega + 1}\right| \tag{3.25}$$

In eq. (3.25), the sign j is the imaginary unit and the absolute value signs represent the magnitude of the complex number $G(jw)$.

In order to calculate $|G(jw)|$, the complex number $G(jw)$ is first divided into its real and imaginary parts as given in eq. (3.26).

$$G(jw) = \frac{1}{(\tau\omega)^2 + 1} + j\frac{-\tau\omega}{(\tau\omega)^2 + 1} \tag{3.26}$$

Then the magnitude of the complex number is calculated by summing the squares of the real and imaginary parts of eq. (3.26) and square-rooting the sum, as given in eq. (3.27). This operation yields the expression given in eq. (3.28).

$$|G(jw)| = \sqrt{\frac{1}{((\tau\omega)^2 + 1)^2} + \frac{(\tau\omega)^2}{((\tau\omega)^2 + 1)^2}} \tag{3.27}$$

$$|G(jw)| = \frac{1}{\sqrt{1 + (\tau\omega)^2}} \tag{3.28}$$

Equation (3.28) shows how much the sinusoidal input's magnitude is attenuated or amplified by the first-order transfer function at the frequency ω.

3.3.4 H_2 Norms of Dynamical Systems

In order to quantify the size of the outputs of dynamical systems under known inputs, dynamical system norms are used as measure [129]. In other words, system norms are different ways of defining the dynamical system gains, i.e. the amplification or attenuation of signals through the system [130]. This work utilizes H_2 norms of linear, time-invariant, single input, single output, stable dynamical systems. The mathematical definition of the H_2 norm for such a system, which is defined by the transfer function G, is given in eq. (3.29) [130].

$$||G||_2 = \sqrt{\frac{1}{2\pi}\int_{-\infty}^{+\infty} |G(j\omega)|^2 \, d\omega} \tag{3.29}$$

Looking at the integral in eq. (3.29), it can be seen that the H_2 norm sums the square of the frequency response magnitude, i.e. the gain, of the system G over all frequencies. From this aspect, H_2 norm can be interpreted as a measure of the average system gain taken over all frequencies [131].

In this work, H_2 norms of first-order systems with and without time delays are used. First, the H_2 norm relation is given below for first-order systems without the time delay. The system defined in eq. (3.19) is considered. The H_2 norm of this system can be calculated by placing its frequency response magnitude relation, i.e. eq. (3.28), into eq. (3.29), as given in eq. (3.30).

$$\left|\left|\frac{1}{\tau s + 1}\right|\right|_2 = \sqrt{\frac{1}{2\pi}\int_{-\infty}^{+\infty} \frac{1}{1 + (\tau\omega)^2} \, d\omega} \tag{3.30}$$

Integration[1] gives eq. (3.31).

$$\left\|\frac{1}{\tau s+1}\right\|_2 = \sqrt{\frac{1}{2\pi}\left.\frac{\tan^{-1}(\tau\omega)}{\tau}\right|_{-\infty}^{+\infty}} \tag{3.31}$$

Evaluation of eq. (3.31) yields eq. (3.32).

$$\left\|\frac{1}{\tau s+1}\right\|_2 = \frac{1}{\sqrt{2\tau}} \tag{3.32}$$

3.3.4.1 H_2 Norms of First-Order Systems With Time Delay

As presented above, the H_2 norm of a simple transfer function without time delay, such as the one given in eq. (3.19), can be calculated analytically in a straightforward fashion. However, following the same approach for the time-delayed transfer function given in eq. (3.24), the antiderivative of the term $|G(j\omega)|^2$ in eq. (3.29) could not be expressed in terms of standard mathematical functions[1]. Therefore, in order to obtain a representation of the average gain of a time-delayed system in terms of the delay, an alternative method is followed.

On the calculation of H_2 norms for systems containing delays, Jarlebring et al. [132] present a method, which is based on solution of Lyapunov equation. Based on their method, they present the H_2 norm relation for a first-order, scalar, linear system given by eq. (3.33).

$$\begin{aligned} \dot{x}(t) &= -ax(t-\lambda) + bu(t) \\ y(t) &= cx(t) \end{aligned} \tag{3.33}$$

In the system given in eq. (3.33), which is written in time domain, the terms u, y, and x are the input, output and system's state variable, respectively. The terms a, b, and c are the coefficients defining the system's dynamics, its input-state and state-output relations, respectively. Finally the terms t and λ represent the time and the time delay. Assuming that the system is stable, the H_2 norm of this system is given in terms of its parameters by eq. (3.34)[132].

$$\sqrt{\frac{c^2b^2}{2a}\frac{\cos(a\lambda)}{1-\sin(a\lambda)}} \tag{3.34}$$

The H_2 norm of the time-delayed transfer function given in eq. (3.24) can be written based on eq. (3.34). Therefore the system given in eq. (3.33) is written in the form of the time-delayed transfer function given in eq. (3.24). Assuming that the output of the system given in eq. (3.33) is its state, the parameter c becomes 1.

[1]Wolfram Alpha Online Integral Calculator. URL: `http://www.wolframalpha.com/calculators/integral-calculator/`. Accessed: 04 February 2017.

Therefore, $y(t) = x(t)$. Using this equality, the system dynamics can be written in terms of the output $y(t)$ as given in eq. (3.35).

$$\dot{y}(t) = -ay(t-\lambda) + bu(t) \tag{3.35}$$

Taking the Laplace transform of eq. (3.35) with zero initial conditions, eq. (3.36) is obtained.

$$sY(s) = -ae^{-s\lambda}Y(s) + bU(s) \tag{3.36}$$

Rearranging the terms give eqs. (3.37) and (3.38), respectively.

$$Y(s) = \frac{b}{s + ae^{-s\lambda}}\,U(s) \tag{3.37}$$

$$Y(s) = \frac{b/a}{(1/a)s + e^{-s\lambda}}\,U(s) \tag{3.38}$$

Equation (3.38) is in the same form as the delayed transfer function given in eq. (3.24). One-to-one comparison of the coefficients gives that, $1/a = \tau$, $b/a = 1$, and therefore $a = b = 1/\tau$. Inserting this relation with $c = 1$ into eq. (3.34), the H_2 norm relation of the time-delayed transfer function given in eq. (3.24) can be found. Equation (3.39) gives this relation.

$$||G_d(s)||_2 = \frac{1}{\sqrt{2\tau}}\sqrt{\frac{\cos(\lambda/\tau)}{1-\sin(\lambda/\tau)}} \tag{3.39}$$

Comparing eq. (3.39) with the H_2 norm of the delay-free transfer function given in eq. (3.32), it can be seen that the second multiplier term in eq. (3.39) becomes one if the system has no delay ($\lambda = 0$), yielding the same relation as that given in eq. (3.32).

3.3.5 Representation of Sample Time as Delay

This work involves sampled signals, whose values are updated at discrete time instants. However for the representation and analysis of the dynamical systems, linear systems theory in continuous time is used. Therefore continuous-time representation of sampled signals is considered.

Franklin et al. [128] study a continuous signal together with its sampled and held version, such as the ones shown in figure 3.3. They state that, a good approximation of sampled and held signals in continuous time is representing them as signals with pure time delay. That is, a signal, which is sampled and held by T-second intervals, is represented in continuous time as the original signal delayed by $T/2$ seconds.

Figure 3.3 depicts an example continuous signal along with its sampled and held

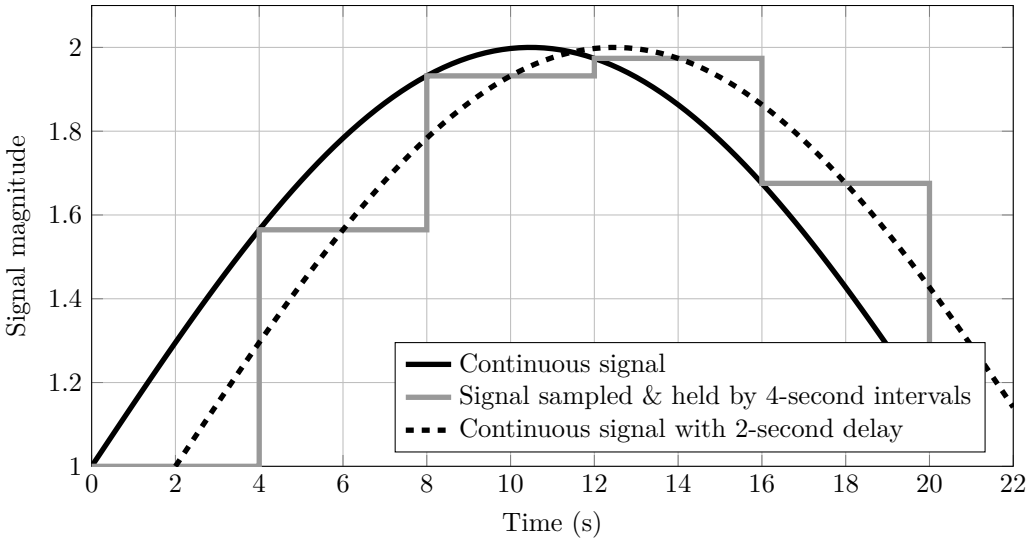

Figure 3.3: Continuous-time representation of a sampled and held signal. The plot was generated based on Franklin et al. [128].

counterpart. The sampling period of the sampled and held signal is 4 seconds. By delaying the original continuous signal by 2 seconds, i.e. by the half of the update period, another continuous signal is obtained. As shown, this continuous signal fits on the sampled signal, having the same value as the sampled signal at the mid-instants between two updates.

Chapter 4

Aircraft Flight-Dynamical Models and Simulation

This chapter gives detailed descriptions of the flight-dynamical models of the leader and follower aircraft. Both aircraft are identical, and they are represented in the simulation environment by different instances of the same flight-dynamical model.

As outlined in Section 1.3.3, two sets of formation flight simulations are performed in this work, each with different scales of aircraft. For both scales of aircraft pairs, the above-described conditions and the similarities between the leader and the follower aircraft apply. The different scales of aircraft are described by the same flight-dynamical model. The differences between each scale lie in the dimensional entities of the flight-dynamical model, such as mass, wingspan, maximum thrust, actuator slew rates, etc.

The lower-scale aircraft model describes an unmanned fixed-wing aircraft of 3.2-meter wingspan and 22.5-kg operative mass. The aircraft [133, 134], which is depicted in figure 4.1, is designed and operated by the Institute of Flight Systems of the German Aerospace Center (DLR) in Braunschweig, Germany. The higher-scale aircraft flight-dynamical model is derived from this aircraft by applying the dynamical scaling laws presented in Chapter 3. The wingspan of the higher-scale aircraft is selected as 20 meters, which corresponds to medium-altitude-long-endurance UAVs. Basic specifications of the lower-scale and higher-scale aircraft are summarized in table 4.1.

The flight altitude of the higher-scale aircraft is designated to be the same altitude as that of the lower-scale aircraft within the scope of this work, in order to simplify the dynamical scaling relations between the lower-scale and higher-scale aircraft. With the knowledge of the ratio of the characteristic lengths of both scales of aircraft along with the air density and the gravitational acceleration at their flight altitude, the dynamical scaling coefficients are determined. If the higher-scale and lower-scale aircraft fly at the same altitude, the density and gravity scale factors will be unity. Hence, all dynamic scaling coefficients become a function of solely the ratio of the

characteristic lengths of both scales of aircraft, i.e. the length scale factor $R_l = 6.25$.

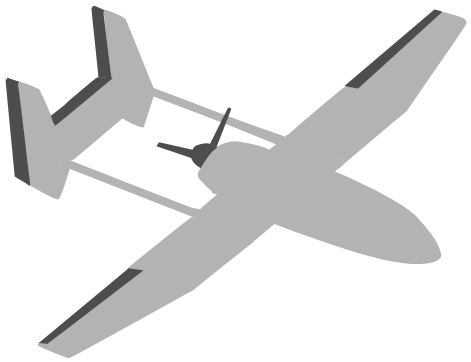

Figure 4.1: Configuration of the UAV operated by DLR Institute of Flight Systems, which is used in this work as the lower-scale aircraft. The plot was generated based on Ref. 134.

	Lower scale	**Higher scale**	**Units**
b	3.2	20	m
S	1.0846	42.3672	m^2
$\mathcal{AR}$	9.4413	9.4413	–
$\bar{c}$	0.3485	2.1781	m
m	22.5	5493.16	kg

Table 4.1: Aircraft geometric and mass specifications.

4.1 Equations of Motion

The dynamics of the aircraft is modeled by nonlinear, six-degree-of-freedom, rigid-body equations of motion given by Stevens and Lewis [119]. These equations, which define the aircraft's motion about its center of gravity, are stated below.

$$\dot{u} = rv - qw - g\sin\theta + \frac{1}{\mathrm{m}}\left(\frac{1}{2}\rho {V_A}^2 S C_X\right) + \frac{X_P}{\mathrm{m}} \tag{4.1}$$

$$\dot{v} = -ru + pw + g\sin\phi\cos\theta + \frac{1}{\mathrm{m}}\left(\frac{1}{2}\rho {V_A}^2 S C_Y\right) + \frac{Y_P}{\mathrm{m}} \tag{4.2}$$

$$\dot{w} = qu - pv + g\cos\phi\cos\theta + \frac{1}{\mathrm{m}}\left(\frac{1}{2}\rho {V_A}^2 S C_Z\right) + \frac{Z_P}{\mathrm{m}} \tag{4.3}$$

Equations (4.1) to (4.3) are the *force equations* and they define the translational velocity dynamics of the aircraft. The terms u, v and w are the components of the aircraft's ground velocity, which are expressed on the axes of body-fixed reference

frame. The terms p, q and r are the components of the aircraft's angular velocity, which are expressed on the axes of body-fixed reference frame. They are also called *roll rate*, *pitch rate* and *yaw rate*, respectively. The angles ϕ and θ are the bank and pitch angles. The terms g and ρ are the gravitational acceleration and air density, respectively. The terms m and S are the aircraft mass and wing area. The term V_A is the magnitude of the aerodynamic velocity, defined later in this section in eq. (4.40). The terms C_X, C_Y, C_Z and X_P, Y_P, Z_P are the aerodynamic force coefficients and propulsive force components along the axes of the body-fixed reference frame. These terms are explained in eq. (4.25) and eq. (4.20) respectively.

The next set of equations define the attitude dynamics and are called *kinematic equations* [119]. They are given below in eqs. (4.4) to (4.7). In this work, the attitude dynamics of the aircraft is represented using *quaternions* [119], in order to avoid the occurrence of singularity in attitude-angle-based kinematic equations [119] at θ values near ± 90 degrees.

$$\dot{q}_0 = \frac{1}{2}\left(-pq_1 - qq_2 - rq_3\right) \tag{4.4}$$

$$\dot{q}_1 = \frac{1}{2}\left(pq_0 + rq_2 - qq_3\right) \tag{4.5}$$

$$\dot{q}_2 = \frac{1}{2}\left(qq_0 - rq_1 + pq_3\right) \tag{4.6}$$

$$\dot{q}_3 = \frac{1}{2}\left(rq_0 + qq_1 - pq_2\right) \tag{4.7}$$

Since the attitude angles have direct physical meaning, the attitude of the aircraft is represented by the attitude angles. The attitude angles can be calculated from quaternions using eqs. (4.8) to (4.10).

$$\tan\phi = \frac{2(q_0q_1 + q_2q_3)}{q_0^2 - q_1^2 - q_2^2 + q_3^2} \tag{4.8}$$

$$\sin\theta = 2(q_0q_2 - q_1q_3) \tag{4.9}$$

$$\tan\psi = \frac{2(q_0q_3 + q_1q_2)}{q_0^2 + q_1^2 - q_2^2 - q_3^2} \tag{4.10}$$

Equations (4.11) to (4.13) give the *moment equations*, which define the rotational velocity dynamics of the aircraft. The rotational velocity components p, q, r are expressed on the axes of the aircraft's body-fixed frame.

$$\dot{p} = \left(\frac{(I_{yy} - I_{zz})I_{zz} - I_{xz}^2}{I_{xx}I_{zz} - I_{xz}^2} r + \frac{(I_{xx} - I_{yy} + I_{zz})I_{xz}}{I_{xx}I_{zz} - I_{xz}^2} p \right) q + \frac{I_{zz}}{I_{xx}I_{zz} - I_{xz}^2} l + \frac{I_{xz}}{I_{xx}I_{zz} - I_{xz}^2} n \tag{4.11}$$

$$\dot{q} = \frac{I_{zz} - I_{xx}}{I_{yy}} pr - \frac{I_{xz}}{I_{yy}}(p^2 - r^2) + \frac{1}{I_{yy}} m \tag{4.12}$$

$$\dot{r} = \left(\frac{I_{xx}(I_{xx} - I_{yy}) + I_{xz}^2}{I_{xx}I_{zz} - I_{xz}^2} p - \frac{(I_{xx} - I_{yy} + I_{zz})I_{xz}}{I_{xx}I_{zz} - I_{xz}^2} r \right) q + \frac{I_{xz}}{I_{xx}I_{zz} - I_{xz}^2} l + \frac{I_{xx}}{I_{xx}I_{zz} - I_{xz}^2} n \tag{4.13}$$

In the moment equations, the l, m and n terms are the moment components about the center of gravity of the aircraft, which are expressed on the axes of body-fixed reference frame. The terms I_{xx}, I_{yy}, I_{zz} and I_{xz} are the moments of inertia and the cross product of inertia, respectively. Since the aircraft's body axes xz-plane is a plane of symmetry, cross products of inertia, I_{xy} and I_{yz}, are zero and thus do not appear in the moment equations.

The moment components are further expanded as given in eqs. (4.14) to (4.16) below. As shown, the moments have two components: aerodynamic and propulsive. The propulsive moment components l_P, m_P and n_P include the influence of the engine. The remaining terms are the aerodynamic moments, which are the functions of the aerodynamic moment coefficients of the aircraft, C_l, C_m and C_n. The term b is the wing span of the aircraft and $\bar{c}$ is the mean aerodynamic chord of the aircraft wing. The remaining terms are already explained above in this section.

$$l = \frac{1}{2}\rho {V_A}^2 S \frac{b}{2} C_l + l_P \tag{4.14}$$

$$m = \frac{1}{2}\rho {V_A}^2 S \bar{c} C_m + m_P \tag{4.15}$$

$$n = \frac{1}{2}\rho {V_A}^2 S \frac{b}{2} C_n + n_P \tag{4.16}$$

The propulsive moment components are further expanded as given in eqs. (4.17) to (4.19).

$$l_P = -Y_P \, (z^{cg,trst})_B + Z_p \, (y^{cg,trst})_B \tag{4.17}$$

$$m_P = X_P\,(z^{cg,trst})_B - Z_p\,(x^{cg,trst})_B \tag{4.18}$$

$$n_P = -X_P\,(y^{cg,trst})_B + Y_p\,(x^{cg,trst})_B \tag{4.19}$$

The thrust components X_P, Y_P, Z_P, which are expressed in the body-fixed frame, are expanded in eq. (4.20).

$$\begin{bmatrix} X_p \\ Y_P \\ Z_P \end{bmatrix}_B = \begin{bmatrix} T\cos i_{trst} \\ 0 \\ -T\sin i_{trst} \end{bmatrix}_B \tag{4.20}$$

In eqs. (4.17) to (4.20), the terms $(x^{cg,trst})_B$, $(y^{cg,trst})_B$ and $(z^{cg,trst})_B$ are the components of the relative position vector of the thrust vector action point with respect to the center of gravity location, expressed in body-fixed frame. The term T is the thrust force magnitude and the i_{trst} is the thrust vector incidence angle with respect to the body fixed frame. The incidence angle lies only on the $x_B z_B$ plane, therefore the sidewards propulsive force component Y_P is zero. A positive incidence angle results in a thrust component in the negative direction of the body-fixed frame z-axis.

The thrust T is determined by the formula given in eq. (4.21), in which T_{max} is the air density and the aerodynamic velocity-dependent maximum thrust and δ_t is the thrust setting, expressed as percentage of the maximum thrust, with maximum value of 1 and minimum value of 0.

$$T = T_{max}\,\delta_t \tag{4.21}$$

The final set of equations of motion are the *navigation equations*, which govern the position dynamics of the aircraft. They are given by eqs. (4.22) to (4.24). The rate of change of position is defined with respect to the local NED frame, on whose axes the components $\dot{x}, \dot{y}, \dot{z}$ are also expressed.

$$\begin{aligned} \dot{x} =& u\cos\theta\cos\psi + v(-\cos\phi\sin\psi + \sin\phi\sin\theta\cos\psi) \\ &+ w(\sin\phi\sin\psi + \cos\phi\sin\theta\cos\psi) \end{aligned} \tag{4.22}$$

$$\begin{aligned} \dot{y} =& u\cos\theta\sin\psi + v(\cos\phi\cos\psi + \sin\phi\sin\theta\sin\psi) \\ &+ w(-\sin\phi\cos\psi + \cos\phi\sin\theta\sin\psi) \end{aligned} \tag{4.23}$$

$$\dot{z} = -u\sin\theta + v\sin\phi\cos\theta + w\cos\phi\cos\theta \tag{4.24}$$

The coordinate transformation relations for the reference frames used in this section are given in Section 2.3.6.

4.2 Aerodynamics

4.2.1 Force and Moment Coefficients

The aerodynamic force and moment coefficients C_X, C_Y, C_Z and C_l, C_m, C_n which appear in the force and moment equations, are expanded in this section [79, 118, 119].

Based on the angular relations between the aerodynamic velocity vector and the aircraft's body (α and β in figure 2.2), and the definitions of the lift and drag forces, the force coefficients C_X and C_Z can be written in terms of lift and drag coefficients. Since the positive drag force points to the negative direction of the x_A axis, and the positive lift is defined along the negative direction of the z_A axis, Equation (4.25) can be written using the transformation matrix $\boldsymbol{T}_{BA}$ (eq. (2.9)).

$$\begin{bmatrix} C_X \\ C_Y \\ C_Z \end{bmatrix}_B = \boldsymbol{T}_{BA} \begin{bmatrix} -C_D \\ C_Y \\ -C_L \end{bmatrix}_A \tag{4.25}$$

The coefficients C_L, C_D and C_Y, which belong to the entire aircraft geometry, are written in terms of dimensionless aerodynamic derivatives as given below.

$$C_L = C_{L_0} + C_{L_\alpha}(\alpha + i_w) + \frac{S_t \overline{q}_t}{S\overline{q}} C_{L_t} \tag{4.26}$$

$$C_{L_t} = C_{L_{t\alpha_t}} \alpha_t + C_{L_{t\delta_e}} \delta_e \tag{4.27}$$

$$C_D = C_{D_0} + \frac{C_L^2}{\pi\, \mathcal{AR}\, e} \tag{4.28}$$

$$C_Y = C_{Y_\beta}\beta + C_{Y_p} p^* + C_{Y_r} r^* + C_{Y_{\delta_a}} \delta_a + C_{Y_{\delta_r}} \delta_r \tag{4.29}$$

In eqs. (4.26) to (4.29) the terms with subscript t are the properties of the horizontal stabilizer. The term i_w is the wing incidence angle, the angle on $x_B z_B$ plane and between the body-fixed frame's x-axis and the wing's mean aerodynamic chord. A positive incidence angle is obtained if the wing section is rotated about the y_B-axis in the positive direction. The term $\overline{q}$ is the dynamic pressure, which is defined by the relation $\overline{q} = \frac{1}{2}\rho V_A^2$. The term $\overline{q}_t$ is the dynamic pressure at the horizontal stabilizer. In this work, for the calculation of the $\overline{q}_t$, the downwash and propeller effects on the horizontal stabilizer are neglected. Therefore the horizontal stabilizer dynamic pressure equals the aircraft dynamic pressure, $\overline{q}$. The term C_{L_0} is the lift coefficient

of the aircraft wing and body combination at $\alpha = 0$, noting that $i_w = 0$. The terms S and S_t are the areas of the aircraft's wing and horizontal stabilizer, respectively. The symbol $\mathcal{AR}$ represents the aspect ratio of the aircraft's wing, which is defined by b^2/S, with b representing the wing span. The terms p^* and r^* are dimensionless roll and yaw rates, which are defined later in this section. The terms δ_e, δ_a and δ_r are the deflections of the elevator, aileron and rudder, respectively. The sign convention for the aerodynamic control surface deflections are as follows. A positive elevator deflection is obtained if the elevator is deflected downwards. For the ailerons, positive deflection is defined by the downward deflection of the right aileron and upward deflection of the left aileron. For the rudder, the deflection to the left defines the positive direction.

The aerodynamic derivatives define the change of the force or moment coefficients with respect to the change of the corresponding control or state variable written as subscript. For example the aerodynamic derivative C_{Y_β} define the change of the side force coefficient C_Y with respect to the sideslip angle, β. Mathematical descriptions of the aerodynamic derivatives that appear in eqs. (4.26) to (4.29) are summarized in Table 4.2 on page 75.

In the aerodynamic database used, the aerodynamic derivatives for the moment coefficients were calculated about a fixed location on the aircraft, which is called *moment reference point*. This point is abbreviated as *mrp*. The components of the moment coefficients are expressed on the axes of the aerodynamic frame. These are given below in eqs. (4.30) to (4.32).

$$(C_{l,mrp})_A = (C_{l_{\beta_\alpha}}\alpha + C_{l_\beta})\beta + C_{l_p}p^* + C_{l_r}r^* + C_{l_{\delta_a}}\delta_a + C_{l_{\delta_r}}\delta_r \tag{4.30}$$

$$(C_{m,mrp})_A = C_{m_0} - \frac{S_t\overline{q}_t}{S\overline{q}}C_{L_t}\frac{(x^{npt,mrp})_A}{\overline{c}} + C_{m_q}q^* \tag{4.31}$$

$$(C_{n,mrp})_A = C_{n_\beta}\beta + C_{n_p}p^* + C_{n_r}r^* + C_{n_{\delta_a}}\delta_a + C_{n_{\delta_r}}\delta_r \tag{4.32}$$

The subscripts A on the right hand side of the parentheses mean that the moment coefficient component is expressed on the corresponding axes of the aerodynamic frame. The term $\overline{c}$ is the wing's mean aerodynamic chord. The term C_{m_0} in eq. (4.31) is the moment coefficient of the aircraft wing and body combination at steady state ($q = 0$), with $\alpha = 0$. The term $(x^{npt,mrp})_A$ is the longitudinal position of the moment reference point with respect to the horizontal stabilizer's neutral point, expressed in the aerodynamic frame. Since the aerodynamic frame can rotate during the flight with respect to the aircraft body, the distance term is defined in the body-frame as given in eq. (4.33).

$$(x^{npt,mrp})_A = \cos\alpha\cos\beta(x^{npt,mrp})_B \tag{4.33}$$

Similar to the procedure shown in eq. (4.25), the moment coefficient components given in eqs. (4.30) to (4.32) can be transformed from aerodynamic frame into body-fixed frame as shown in eq. (4.34).

$$\begin{bmatrix} C_{l,mrp} \\ C_{m,mrp} \\ C_{n,mrp} \end{bmatrix}_B = \boldsymbol{T}_{BA} \begin{bmatrix} C_{l,mrp} \\ C_{m,mrp} \\ C_{n,mrp} \end{bmatrix}_A \tag{4.34}$$

Since the moment components l, m and n of eqs. (4.14) to (4.16) are the moments about the aircraft center of gravity, the moment coefficients C_l, C_m, C_n, that appear in those equations should also be written about the aircraft center of gravity. Hence, the moment coefficients given in left hand side of eq. (4.34) can be written about the aircraft center of gravity, as given in eqs. (4.35) to (4.37).

$$C_l = (C_{l,cg})_B = (C_{l,mrp})_B - C_Y \frac{(z^{cg,mrp})_B}{b/2} + C_Z \frac{(y^{cg,mrp})_B}{b/2} \tag{4.35}$$

$$C_m = (C_{m,cg})_B = (C_{m,mrp})_B + C_X \frac{(z^{cg,mrp})_B}{\overline{c}} - C_Z \frac{(x^{cg,mrp})_B}{\overline{c}} \tag{4.36}$$

$$C_n = (C_{n,cg})_B = (C_{n,mrp})_B - C_X \frac{(y^{cg,mrp})_B}{b/2} + C_Y \frac{(x^{cg,mrp})_B}{b/2} \tag{4.37}$$

In eqs. (4.35) to (4.37) the terms $(x^{cg,mrp})_B$, $(y^{cg,mrp})_B$ and $(z^{cg,mrp})_B$ are the longitudinal, lateral and vertical components of the distance from the aircraft center of gravity to the moment reference point, expressed on the body-fixed reference frame. The mathematical descriptions of the aerodynamic derivatives, that appear in eqs. (4.26) to (4.32) are summarized in Table 4.2.

4.2.2 Aerodynamic Velocities and Angles

The rigid-body equations of motion (eqs. (4.1) to (4.7), (4.11) to (4.13) and (4.22) to (4.24)) describe the motion of the aircraft with respect to the inertial reference frame. However, the forces and moments that govern these equations of motion are functions of the aircraft's motion with respect to the relative airflow. This section gives the aerodynamic velocities and angles [118], on which the aerodynamic moments and forces, as well as the force and moment coefficients depend.

As already mentioned in Chapter 2, the velocity of the aircraft with respect to the surrounding air is called aerodynamic velocity of the aircraft. Equations (4.38) and (4.39) give the translational and rotational aerodynamic velocities of the aircraft, $\boldsymbol{V}_A$ and $\boldsymbol{\Omega}_A$ respectively. The vectors are decomposed on the axes of the aircraft's body-fixed frame. In these equations, the terms $\boldsymbol{V}_W$ and $\boldsymbol{\Omega}_W$ are the translational and rotational wind velocity vectors with respect to the inertial reference frame. The

$C_{L_\alpha} = \dfrac{\partial C_L}{\partial \alpha}$	$C_{L_{t\alpha_t}} = \dfrac{\partial C_{L_t}}{\partial \alpha_t}$	$C_{L_{t\delta_e}} = \dfrac{\partial C_{L_t}}{\partial \delta_e}$	$C_{Y_\beta} = \dfrac{\partial C_Y}{\partial \beta}$
$C_{Y_p} = \dfrac{V_A}{b/2}\dfrac{\partial C_Y}{\partial p}$	$C_{Y_r} = \dfrac{V_A}{b/2}\dfrac{\partial C_Y}{\partial r}$	$C_{Y_{\delta_a}} = \dfrac{\partial C_Y}{\partial \delta_a}$	$C_{Y_{\delta_r}} = \dfrac{\partial C_Y}{\partial \delta_r}$
$C_{l_{\beta_\alpha}} = \dfrac{\partial C_{Y_\beta}}{\partial \alpha}$	$C_{l_\beta} = \dfrac{\partial C_l}{\partial \beta}$	$C_{l_p} = \dfrac{V_A}{b/2}\dfrac{\partial C_l}{\partial p}$	$C_{l_r} = \dfrac{V_A}{b/2}\dfrac{\partial C_l}{\partial r}$
$C_{l_{\delta_a}} = \dfrac{\partial C_l}{\partial \delta_a}$	$C_{l_{\delta_r}} = \dfrac{\partial C_l}{\partial \delta_r}$	$C_{m_q} = \dfrac{V_A}{\bar{c}}\dfrac{\partial C_m}{\partial q}$	$C_{n_\beta} = \dfrac{\partial C_n}{\partial \beta}$
$C_{n_p} = \dfrac{V_A}{b/2}\dfrac{\partial C_n}{\partial p}$	$C_{n_r} = \dfrac{V_A}{b/2}\dfrac{\partial C_n}{\partial r}$	$C_{n_{\delta_a}} = \dfrac{\partial C_n}{\partial \delta_a}$	$C_{n_{\delta_r}} = \dfrac{\partial C_n}{\partial \delta_r}$

Table 4.2: Mathematical descriptions of the aerodynamic derivatives defining the aerodynamic characteristics of the aircraft used in this work.

terms $\boldsymbol{V}$ and $\boldsymbol{\Omega}$ are the translational and rotational velocity vectors of the aircraft with respect to the inertial reference frame.

$$\boldsymbol{V}_A = \boldsymbol{V} - \boldsymbol{V}_W = \begin{bmatrix} u_A \\ v_A \\ w_A \end{bmatrix}_B = \begin{bmatrix} u \\ v \\ w \end{bmatrix}_B - \begin{bmatrix} u_W \\ v_W \\ w_W \end{bmatrix}_B \tag{4.38}$$

$$\boldsymbol{\Omega}_A = \boldsymbol{\Omega} - \boldsymbol{\Omega}_W = \begin{bmatrix} p_A \\ q_A \\ r_A \end{bmatrix}_B = \begin{bmatrix} p \\ q \\ r \end{bmatrix}_B - \begin{bmatrix} p_W \\ q_W \\ r_W \end{bmatrix}_B \tag{4.39}$$

Based on eq. (4.38) the magnitude of the translational aerodynamic velocity $\boldsymbol{V}_A$ can be written as given in eq. (4.40).

$$||\boldsymbol{V}_A|| = \sqrt{u_A^2 + v_A^2 + w_A^2} = V_A \tag{4.40}$$

Based on eqs. (4.38) and (4.40) the aerodynamic angle relations can be written as given in eqs. (4.41) and (4.42).

$$\tan\alpha = \frac{w_A}{u_A} \tag{4.41}$$

$$\sin\beta = \frac{v_A}{V_A} \tag{4.42}$$

Equation (4.27) also includes the term α_t, which is the effective angle of attack of the horizontal stabilizer. Based on the angle of attack and pitch rate of the aircraft,

this effective angle of attack is defined by eq. (4.43).

$$\alpha_t = \alpha + i_t + \frac{(q_A)_B (x^{npt,cg})_B}{V_A} - \varepsilon_{t_0} + \frac{\partial \varepsilon_t}{\partial \alpha}\alpha \tag{4.43}$$

In eq. (4.43), the term i_t is the incidence angle of the horizontal stabilizer, defined positive in the same way as the wing incidence angle. The term $(x^{npt,cg})_B$ is the distance of the aircraft center of gravity cg with respect to the horizontal stabilizer neutral point npt, expressed in the body-fixed frame. The term ε_t is the downwash angle at the horizontal stabilizer. The term ε_{t_0} is the downwash angle at the horizontal stabilizer, at $\alpha = 0$.

Finally, the non-dimensional aerodynamic rotational velocities p^*, q^* and r^* are defined, which appear in the moment coefficient build-up equations, namely eqs. (4.30) to (4.32).

$$p^* = \frac{b(p_A)_A}{2V_A} \tag{4.44}$$

$$q^* = \frac{\overline{c}(q_A)_A}{V_A} \tag{4.45}$$

$$r^* = \frac{b(r_A)_A}{2V_A} \tag{4.46}$$

The $(p_A)_A$, $(q_A)_A$ and $(r_A)_A$ are the aerodynamic rotational rates, which are expressed in the aerodynamic frame. They can be calculated using eq. (4.47) with eq. (4.39).

$$\begin{bmatrix} p_A \\ q_A \\ r_A \end{bmatrix}_A = \boldsymbol{T}_{AB} \begin{bmatrix} p_A \\ q_A \\ r_A \end{bmatrix}_B \tag{4.47}$$

4.3 Actuator Models

The actuator models describe the dynamics of the aircraft actuators, which deflect the control surfaces and set the throttle. The actuator models are defined by second-order dynamics with limits in deflections and deflection rates [134].

Figure 4.2 depicts the second-order actuator dynamics in block diagram form using the elevator channel as example. The terms ω_0 and ζ are the natural frequency and the damping ratio of the second-order dynamics, respectively. The upper and lower limits of the deflections and deflection rates are also included in the figure. The term δ_{e_c} is the commanded elevator deflection, the term δ_e is the actual value of the elevator deflection. The commanded values of the control variables are set by the aircraft autopilot. The actual values of the control variables act on the aircraft's

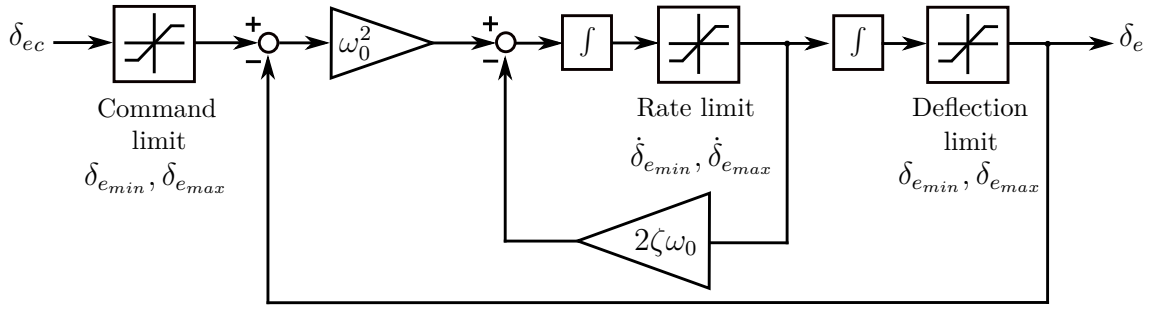

Figure 4.2: Second-order actuator model with deflection and rate limits.

equations of motion. The remaining control channels (δ_a, δ_r, δ_t) are described by the same type of dynamics as the one shown in figure 4.2. Each actuator is specified by its own parameter values.

4.4 Solution of the Equations of Motion

The nonlinear equations of motion given by eqs. (4.1) to (4.7), (4.11) to (4.13) and (4.22) to (4.24) describe the dynamics of the aircraft, using the aerodynamic, engine and actuator characteristics stated above.

The state and control variables of the aircraft model are given in eqs. (4.48) and (4.49).

$$\boldsymbol{x} = [u\, v\, w\, q_0\, q_1\, q_2\, q_3\, p\, q\, r\, x\, y\, z]' \tag{4.48}$$

$$\boldsymbol{u} = [\delta_e\, \delta_a\, \delta_r\, \delta_t]' \tag{4.49}$$

The equations of motion are numerically solved for the state variables $\boldsymbol{x}$ using the explicit Euler integration scheme given in eq. (4.50). In eq. (4.50) the term t defines the current simulation time, and Δt is the simulation time step size. The step size is fixed and taken as 0.005 s for the simulations of both the lower-scale and higher-scale aircraft. The derivative term $\dot{\boldsymbol{x}}(t)$ is obtained by evaluating the nonlinear equations of motion with the state variables of the respective time instant, i.e. $\boldsymbol{x}(t)$. The integration is initialized with desired initial values of the state variables shown in eq. (4.48).

A preliminary comparison of explicit Euler and fourth order Runge-Kutta integration methods on lower-scale aircraft simulations with aforementioned time step size indicated that, the Runge-Kutta method provides an accuracy gain of less than 1.5 millimeters on all three axes of the follower's relative position with respect to the leader while causing substantial increase in simulation time. Hence explicit Euler method was chosen as it provides good balance between solution accuracy and computational overhead for the simulation set up with the selected time step size.

$$\boldsymbol{x}(t+\Delta t) = \boldsymbol{x}(t) + \Delta t\, \dot{\boldsymbol{x}}(t) \tag{4.50}$$

For initialization of the quaternion state variables, desired initial Euler angles are used. These initial Euler angles are then converted to their quaternion counterparts using eq. (4.51) [119].

$$\begin{bmatrix} q_0 \\ q_1 \\ q_2 \\ q_3 \end{bmatrix} = \begin{bmatrix} \cos(\phi/2)\cos(\theta/2)\cos(\psi/2) + \sin(\phi/2)\sin(\theta/2)\sin(\psi/2) \\ \sin(\phi/2)\cos(\theta/2)\cos(\psi/2) - \cos(\phi/2)\sin(\theta/2)\sin(\psi/2) \\ \cos(\phi/2)\sin(\theta/2)\cos(\psi/2) + \sin(\phi/2)\cos(\theta/2)\sin(\psi/2) \\ \cos(\phi/2)\cos(\theta/2)\sin(\psi/2) - \sin(\phi/2)\sin(\theta/2)\cos(\psi/2) \end{bmatrix} \tag{4.51}$$

Chapter 5

Automatic Control of the Aircraft

This chapter details the automatic control aspects of the leader and follower aircraft. Descriptions of the autopilots of the follower and the leader aircraft, the leader's path-following algorithm, and the follower aircraft's formation-hold controller are given. Since the leader and the follower are identical aircraft, their autopilots are identical. The setpoints of the leader aircraft's autopilot are generated by its path-following algorithm. Follower aircraft's autopilot is driven by its formation hold controller.

As stated previously, two sets of formation flight simulations are performed in this work, each with different scales of aircraft. Both scales of aircraft share the same control systems, which are detailed in this chapter. The only difference between the control systems of the lower-scale aircraft and their higher-scale counterparts are the numerical values of the control system gains and tuning parameters. The numerical values of these entities are presented for each scale of aircraft in Appendix A.

As part of the numerical flight simulation scheme employed in this work, the automatic pilots and the guidance algorithms of the aircraft operate at a frequency of 100 Hz.

5.1 Autopilots

The aircraft autopilots are of velocity-hold autopilot type. The autopilot inputs are the commanded values of the ground speed V on the longitudinal channel, the climb angle γ on the vertical channel, and the course angle χ on the lateral channel. This type of autopilot is selected not specifically for the automated formation flight application, but also for obtaining an autopilot compatible with other common UAV missions such as path following and automated landing.

Successive loop closure approach [79] is used in order to keep the overall structure of the autopilot simple. The method suggests the design of successive simple feedback controllers, from fastest to slowest plant dynamics, instead of a more complex single control system. The resulting controller in cascaded form enables a controlled re-

sponse and better disturbance rejection on faster inner-loop state variables. Integral control actions are used on each channel in order to achieve zero steady-state error on each velocity component. Combined with the relative position controller presented in Section 5.3, the follower aircraft autopilot yields a structure comparable to the feedback-control-based formation control approaches outlined in Section 1.4.1.

For the speed control, a single feedback loop is used. This control loop generates throttle command based on the difference between commanded and actual velocity, as given in eq. (5.1). A proportional and integral control action is used.

$$\delta_{t_c} = K_{P_V}(V_c - V) + K_{I_V} \int (V_c - V)\, dt \tag{5.1}$$

The flight path angle control consists of an inner feedback loop for the pitch angle θ, which generates elevator commands using proportional control action on the pitch angle error $\theta_c - \theta$. The setpoint of the pitch angle controller is generated by the outer flight path angle control loop. The flight path angle controller uses proportional and integral control action in order to drive the flight path angle error toward zero. Equations (5.2) and (5.3) give the control actions on the vertical channel.

$$\delta_{e_c} = K_{P_\theta}(\theta_c - \theta) \tag{5.2}$$

$$\theta_c = K_{P_\gamma}(\gamma_c - \gamma) + K_{I_\gamma} \int (\gamma_c - \gamma)\, dt \tag{5.3}$$

On the lateral channel of the autopilot, the outermost course angle control loop generates roll angle command using proportional control action. The inner feedback loop applies another proportional control action on roll angle error in order to generate a roll rate command. The innermost control loop on roll rate uses a proportional and integral control action in order to generate the aileron command. Here a stability augmentation loop is included as adding the fed-back roll rate with proportional action on the aileron command, in order to enhance roll rate damping characteristics. The controller is described in eqs. (5.4) to (5.6).

$$\delta_{a_c} = K_{P_p}(p_c - p) + K_{I_p} \int (p_c - p)\, dt \; + \; K_{damp}\, p \tag{5.4}$$

$$p_c = K_{P_\phi}(\phi_c - \phi) \tag{5.5}$$

$$\phi_c = K_{P_\chi}(\chi_c - \chi) \tag{5.6}$$

The roll rate control loop has an additional importance, considering that the autopilot described above is used in a formation flight application. As described in Chapter 1 and Chapter 6, depending on the relative position of the follower aircraft with respect to the leader, the follower aircraft may experience significant roll distur-

bance, due to the wake flow field of the leader aircraft. Using a roll-rate control loop helps reject this disturbance, before it causes significant relative position errors.

In the present setting of the autopilot, the use of rudder is not required, which is normally the case also in formation flight applications, such as aerial refueling [52].

In eqs. (5.1) to (5.6), the K-terms are the constant gains for the respective control actions. The gain values that are used for lower and higher-scale aircraft are given in Appendix A.

5.2 Leader's Path-Following Guidance

The task of the leader aircraft's guidance is to calculate the commanded state variables, γ_c and χ_c, which are then tracked by the autopilot, so that the aircraft follows a predefined flight path. In this work, the leader aircraft is commanded to fly with constant ground speed, i.e. the designated speed of the formation flight, therefore the commanded ground speed V_c is specified independently from the guidance algorithm.

The leader aircraft's guidance method is based on the approach presented by Park et al. [135]. They present a path-following algorithm, which generates lateral acceleration commands for their autopilot in order to track straight and curved paths on horizontal plane. In this work, their path-following method is modified, so that it can be used with the autopilot presented above. The approach is also extended for compensation of the path offsets in the vertical plane.

Figure 5.1 depicts the main geometrical relations for the path-following guidance method. The aircraft L is depicted in a position, in which it has horizontal (d_1) and vertical (d_2) offsets with respect to the desired path. The point L' represents the projection of the aircraft's position on the horizontal plane, on which the desired flight path also lies. The vehicle-carried NED frame is also centered at this projection point. The guidance algorithm considers a reference point R on the desired path, which moves along the path in such a way that, it always stays at a fixed distance from the aircraft's projection L' on the plane of the path. This means that the two-dimensional vector $\boldsymbol{r}^{L'R}$ always has the constant length l.

As seen in figure 5.1, the vector $\boldsymbol{r}^{L'R}$ makes an angle η_1 with the x-axis of vehicle-carried NED frame. This angle is set as the desired course angle of the vehicle at that moment, in order to eventually eliminate its lateral offset d_1 with the desired path. In order to drive the vertical path offset d_2 to zero, the guidance algorithm determines the desired flight path angle as the angle that the vector $\boldsymbol{r}^{LR}$ makes with the horizontal plane. Both of the angles, η_1 and η_2 can be calculated with the knowledge of the coordinates of the points L, L' and R.

In relation with figure 5.1, eqs. (5.7) and (5.8) give the desired course and flight path angles determined by the path following guidance algorithm.

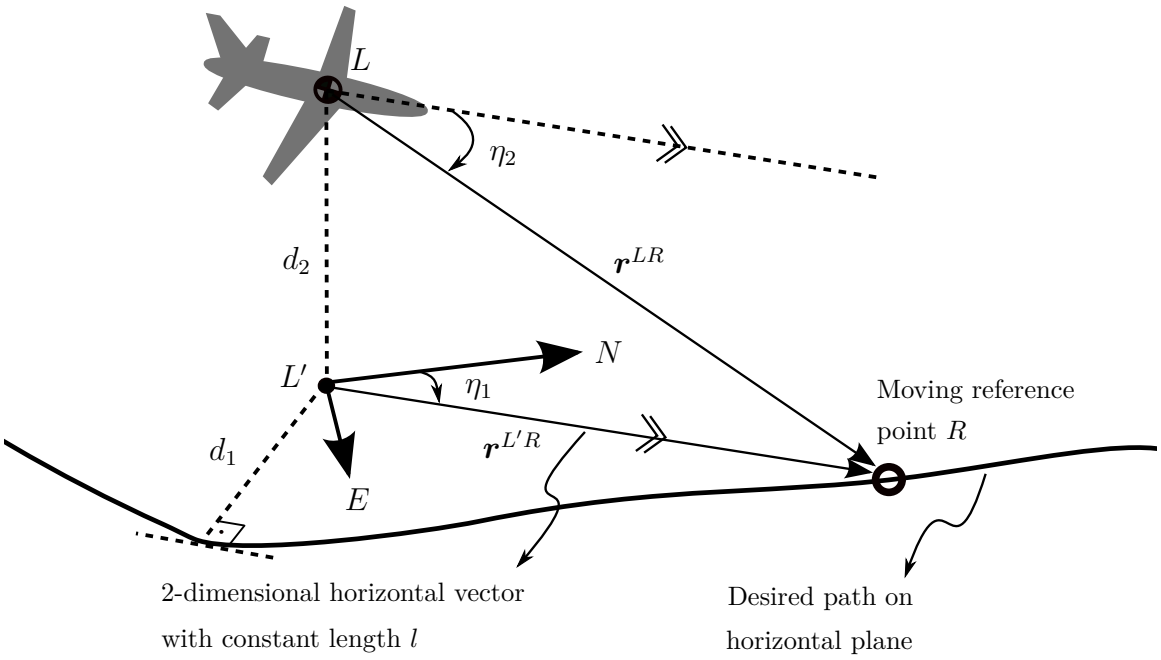

Figure 5.1: Geometric relations for the leader's path-following guidance.

$$\chi_d = \eta_1 \tag{5.7}$$

$$\gamma_d = \eta_2 \tag{5.8}$$

The constant length l of the vector $\boldsymbol{r}^{L'R}$ is the parameter of the path-following guidance algorithm. Its value can be selected so that the vehicle follows the path with desired accuracy.

5.3 Follower's Formation Flight Controller

The task of the formation flight controller is generating the velocity commands V_c, γ_c and χ_c for the follower aircraft autopilot, so that the aircraft follows the leader aircraft at a commanded relative position.

The formation flight controller is designed for keeping the formation without steady-state error during flight on a straight and level path. Straight and level paths are the type of paths, which are used in most applications of the formation flight, such as aerial refueling and aerodynamic drag reduction. The aerial refueling applications usually take place on the racetrack paths, whose straight legs can be considerably longer than the circular segments, depending on the size of the tanker aircraft [9]. Even for larger and faster tanker aircraft, which require greater turn radii, racetrack flight paths are used [9], whose straight segments are still at least about 71 % of

the complete racetrack path. For smaller and slower tankers, this ratio can go up to a value of about 88 % a minimum [9]. In the drag reduction-based applications of the formation flight, the most convenient flight phase is the cruising flight, which is essentially made up of a set of straight and level flight paths.

An assumption for the design of the formation flight control is that the follower aircraft stays well apart from the cores of the wake vortices generated by the leader aircraft. This is also the case for the applications of the formation flight: aerial refueling [52, 68] and aerodynamic drag reduction [14]. In the aerial refueling applications, the aircraft is always below the leader aircraft, so it is vertically separated from the wake vortex core. If the aerial refueling drogue is attached to the fuselage of the leader aircraft, which is likely to be the case on the unmanned automated aerial refueling applications in the first place, or if the boom and receptacle refueling method is used, the follower aircraft has also an additional lateral separation with respect to the core of the leader aircraft wake vortices. On the drag reduction applications of the formation flight, the follower aircraft's fuselage centerline has a lateral separation from the core of the leader aircraft vortices. This separation is about 0.3 times the leader aircraft wingspan, according to the study presented by Okolo et al. [14].

Similar to most of the automated formation control methods presented in the literature [3, 4, 41, 44, 49, 52, 53, 59], the formation controller requires the relative position of the follower aircraft with respect to the leader aircraft. By comparing this relative position information to the commanded relative position, the velocity commands are generated using proportional or proportional and integral control actions.

Knowing the relative position vector of the follower aircraft with respect to the leader aircraft, the next point is to select the reference frame, on whose axes the commanded relative position will be defined. The selected reference frame affects the amount of position error which is seen by the respective formation control channel [52]. Ross et al. [52] discuss the use of different reference frames for this purpose, such as the leader or follower body-fixed frames. Using body frames of the leader and follower is not recommended, because these axis systems rotate with the bodies of the aircraft. As the body-fixed reference frames rotate with the airframes, the change in attitude of the respective aircraft can create additional position error components.

In this work, leader aircraft's kinematic frame is selected as the base reference frame for the formation flight control. The frame is fixed to the leader aircraft and the axes are aligned with respect to the leader's ground velocity vector (see Chapter 2). Since the frame does not rotate with leader's body, the relative position error information, that the follower aircraft processes, does not directly depend on the attitude changes of the leader aircraft.

The positions of the leader and follower aircraft with respect to the earth-fixed, local NED reference frame are available in the simulation environment. These are $\boldsymbol{r}^L$ and $\boldsymbol{r}^F$, respectively. The position of the follower aircraft, relative to the leader aircraft is given by eq. (5.9). This vector is then expressed in the leader's kinematic

frame as shown in eq. (5.10)

$$\boldsymbol{r}^{LF} = \boldsymbol{r}^{F} - \boldsymbol{r}^{L} \tag{5.9}$$

$$\left(\boldsymbol{r}^{LF}\right)_{K_L} = \boldsymbol{T}_{K_L 0}\, \boldsymbol{r}^{LF} \tag{5.10}$$

The desired position of the follower aircraft with respect to the leader is defined by eq. (5.11). Since the leader's kinematic frame is selected as formation flight reference frame, the components of the desired relative position is decomposed on the axes of the leader's kinematic frame.

$$\boldsymbol{r}_d = \begin{bmatrix} x_d \\ y_d \\ z_d \end{bmatrix}_{K_L} \tag{5.11}$$

The desired relative position is used directly as the setpoint of the formation-hold position controller presented below. Therefore the *desired relative position* is the *commanded relative position*. Both terms are used interchangeably throughout the text.

The relative position error during the formation flight is defined by eq. (5.12). It is the difference between the desired relative position and the instant relative position of the follower aircraft with respect to the leader.

$$\boldsymbol{e}_r = \boldsymbol{r}_d - \left(\boldsymbol{r}^{LF}\right)_{K_L} = \begin{bmatrix} x_d \\ y_d \\ z_d \end{bmatrix}_{K_L} - \begin{bmatrix} x^{LF} \\ y^{LF} \\ z^{LF} \end{bmatrix}_{K_L} = \begin{bmatrix} e_x \\ e_y \\ e_z \end{bmatrix}_{K_L} \tag{5.12}$$

For the formation control, each component of the relative position error $\boldsymbol{e}_r$ is handled by different channels of the autopilot. Following the approach of the previous formation flight control applications [44, 45, 52, 53], the throttle channel is allocated for the control of the longitudinal error component. The aileron channel is allocated for the control of the lateral position error and the elevator channel controls the vertical position error component.

In order to cope with the longitudinal relative position error e_x, a proportional control action is applied to the error signal in order to obtain a corrective incremental speed. The corrective speed increment, ΔV is added to the designated speed of the formation flight in order to obtain the commanded speed value for the follower aircraft autopilot. Due to the presence of the integral control action on the velocity-hold autopilot, the use of proportional-only control action on the longitudinal position control proved sufficient for eliminating the steady-state error on the straight and level flight path. Equations (5.13) and (5.14) give the longitudinal position control.

$$V_c = V_d + \Delta V \tag{5.13}$$

$$\Delta V = K_{P_x}\, e_x \tag{5.14}$$

In order to handle the lateral error component e_y, proportional control action is used. With proportional-only control action on the lateral position controller, the closed-loop dynamics allows obtaining zero steady-state position error during the formation flight on a straight and level path. Equations (5.15) and (5.16) give the control of the lateral position. The autopilot's commanded course angle, χ_c is calculated by adding an incremental corrective course angle $\Delta\chi$ to the desired course angle of the formation flight, χ_d.

$$\chi_c = \chi_d + \Delta\chi \tag{5.15}$$

$$\Delta\chi = K_{P_y}\, e_y \tag{5.16}$$

On the vertical channel, the relative position error e_z is handled by application of a proportional control action. As shown in eqs. (5.17) and (5.18), the output of this control action is added to the desired flight path angle as a corrective incremental flight path angle, $\Delta\gamma$. The desired flight path angle is that of the formation flight path, which is zero in the case considered in this work. Similar to the longitudinal channel, the integral control action in the vertical channel of the autopilot helps achieve zero steady state error with proportional-only control action on the vertical position controller.

$$\gamma_c = \gamma_d + \Delta\gamma \tag{5.17}$$

$$\Delta\gamma = K_{P_z}\, e_z \tag{5.18}$$

In eqs. (5.13) to (5.18), the terms K_{P_x}, K_{P_y} and K_{P_z} are the constant gains for the proportional control actions, acting on the three components of the relative position error. The gains are tuned to achieve 5 % overshoot a maximum under a unit step response. The gain values are given in Appendix A.

Figure 5.2 shows the responses of the lower-scale and higher-scale follower aircraft to a unit increment on the commanded relative position at their corresponding flight conditions. The plots are generated using the nonlinear formation flight simulation without aerodynamic disturbances and without imperfections of the relative position information processed by the follower aircraft formation flight controller.

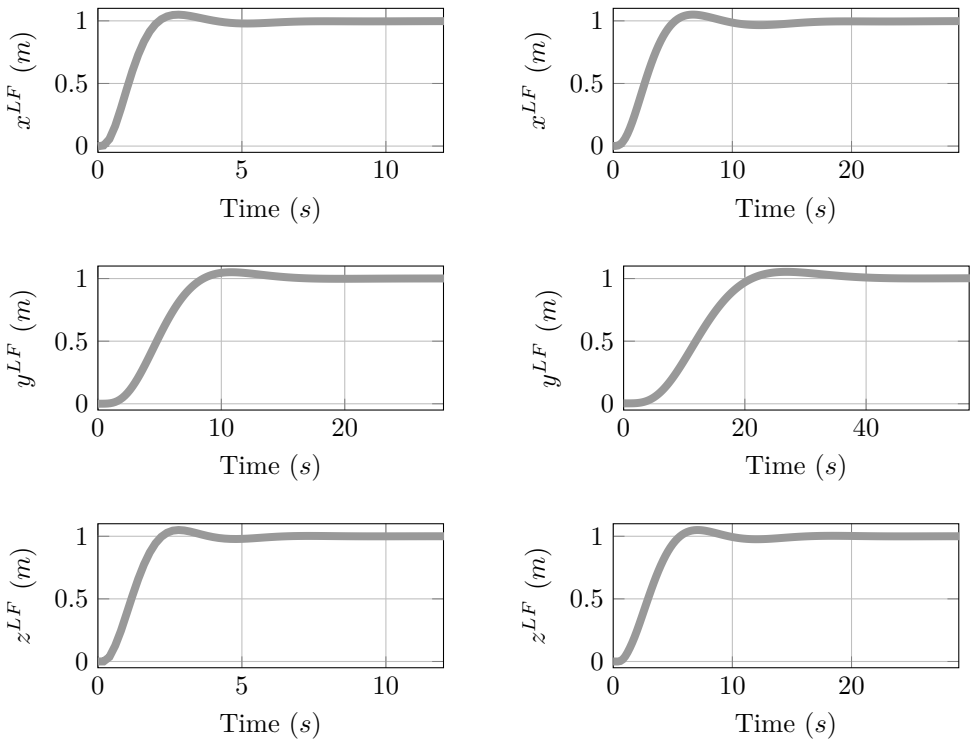

Figure 5.2: Responses to a unit step command given at $t = 0$ s. Left and right-hand-side figures correspond to the lower-scale and higher-scale aircraft respectively.

Chapter 6

Modeling of the Wake Vortex Effects

This chapter details the wake vortex model, describing the flow field behind the leader aircraft, as well as the aerodynamic disturbances acting on the follower aircraft due to the leader's wake flow field. The wake vortex model is based on the approaches presented by Pachter et al. [41] and Dogan et al. [110].

6.1 Velocities Induced by the Leader Aircraft at an Arbitrary Point in Space

A simplified horseshoe vortex [13] is placed on the wing of the leader aircraft as shown in figure 6.1(a). Assuming elliptic lift distribution along the geometric span b_L of the leader's wing, the leader wing is approximated by a wing with constant lift distribution along a span of b'_L. This reduced wingspan is also the span of the bound vortex and defined in eq. (6.1).

$$b'_L = \frac{\pi}{4} b_L \tag{6.1}$$

The constant lift distribution is determined by the constant vortex strength per unit length, Γ, as given in eq. (6.2) [41]. In eq. (6.2) the subscript L denotes that, the corresponding term belongs to the leader aircraft. The terms L, ρ and V are the lift force, ground speed and air density, respectively. The lift is assumed to equal the weight of the leader aircraft. Since no prevailing wind is considered in this work, the ground speed equals the aerodynamic speed.

$$\Gamma = \frac{L_L}{\rho V b'_L} = \frac{4 L_L}{\rho V \pi b_L} \tag{6.2}$$

Combining the Hallock-Burnham vortex-induced velocity profile [136] and Biot-

Savart Law for induced-velocity calculations from finite and semi-infinite, linear vortex filaments [13], eqs. (6.3) to (6.5) can be written. Together with figure 6.2, these equations define the induced velocity vectors at a point P, occurring due to the finite and semi infinite vortices placed on the wing of the leader aircraft.

The leader's horseshoe vortex is defined with respect to the aircraft's kinematic frame and its semi-infinite components A and B remains parallel to the x-axis of the leader's kinematic frame, x_{K_L}. This means that the semi-infinite vortices remain parallel to the ground velocity of the aircraft. Throughout the approach, leader's kinematic frame K_L is used as the main reference frame for defining the components of the vector quantities.

$$\boldsymbol{V}_{w_A} = \frac{\Gamma}{4\pi} \frac{r_A}{r_A^2 + r_c^2} \left(\cos\alpha_A + 1\right) \hat{\boldsymbol{e}}_A \tag{6.3}$$

$$\boldsymbol{V}_{w_B} = \frac{\Gamma}{4\pi} \frac{r_B}{r_B^2 + r_c^2} \left(\cos\alpha_B + 1\right) \hat{\boldsymbol{e}}_B \tag{6.4}$$

$$\boldsymbol{V}_{w_{AB}} = \frac{\Gamma}{4\pi} \frac{r_{AB}}{r_{AB}^2 + r_c^2} \left(\cos\beta_A + \cos\beta_B\right) \hat{\boldsymbol{e}}_{AB} \tag{6.5}$$

The sum of the velocities induced by each vortex filament gives the total induced velocity at an arbitrary point, which is given in eq. (6.6) with components expressed in the K_L-frame. The subscript w is used to denote the wake of the leader aircraft, which induces the velocities.

$$\left(\boldsymbol{V}_w\right)_{K_L} = \left(\boldsymbol{V}_{w_A}\right)_{K_L} + \left(\boldsymbol{V}_{w_B}\right)_{K_L} + \left(\boldsymbol{V}_{w_{AB}}\right)_{K_L} = \begin{bmatrix} u_w \\ v_w \\ w_w \end{bmatrix}_{K_L} \tag{6.6}$$

In eqs. (6.3) to (6.5) and figure 6.2, the terms r_A, r_B and r_{AB} are the orthogonal distances from point P to the semi-infinite and finite vortices. The $\hat{\boldsymbol{e}}_A$, $\hat{\boldsymbol{e}}_B$ and $\hat{\boldsymbol{e}}_{AB}$ terms are the unit vectors, defining the orientation of the velocities induced by the respective vortex filament. The term r_c is the vortex core radius, which is taken in literature as 1 to 5 percent of the wingspan of the vortex-generating aircraft [12]. Schwarz et al. [12] specify the r_c value as 3.5 % of the wingspan based on flight test results. Based on this, here the r_c value is also taken as 3.5 % of b_L.

In order to define the distance, trigonometric and the unit vector terms in eqs. (6.3) to (6.5), the following vector relations should be defined. Based on figure 6.1, the position of an arbitrary point P around the follower aircraft with respect to the points A and B on the leader aircraft can be written as eqs. (6.7) and (6.8).

$$\left(\boldsymbol{r}^{AP}\right)_{K_L} = \left(\boldsymbol{r}^{LF}\right)_{K_L} + \left(\boldsymbol{r}^{AL}\right)_{K_L} + \left(\boldsymbol{r}^{FP}\right)_{K_L} \tag{6.7}$$

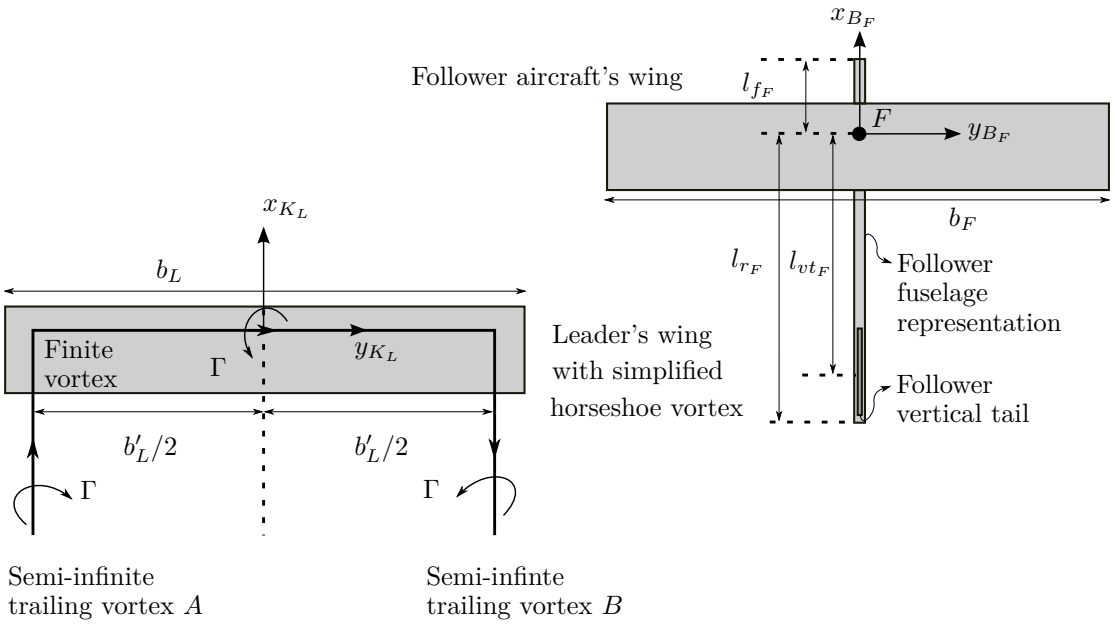

(a) Top view of the two aircraft

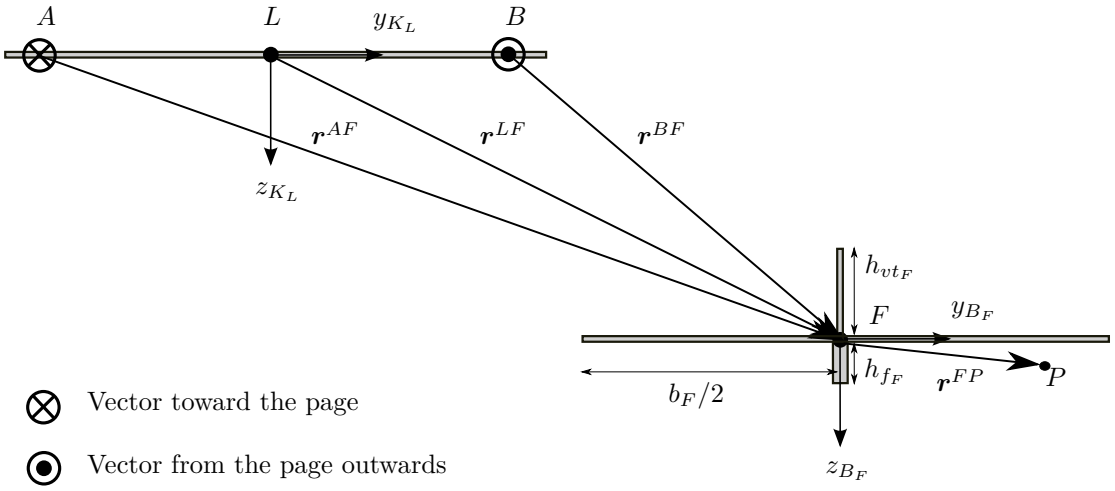

(b) Rear view of the two aircraft

Figure 6.1: Aircraft geometries and reference frames used for vortex effect modeling.

$$\left(\boldsymbol{r}^{BP}\right)_{K_L} = \left(\boldsymbol{r}^{LF}\right)_{K_L} + \left(\boldsymbol{r}^{BL}\right)_{K_L} + \left(\boldsymbol{r}^{FP}\right)_{K_L} \tag{6.8}$$

Each term in eqs. (6.7) and (6.8) are expanded in Equations (6.9) to (6.12).

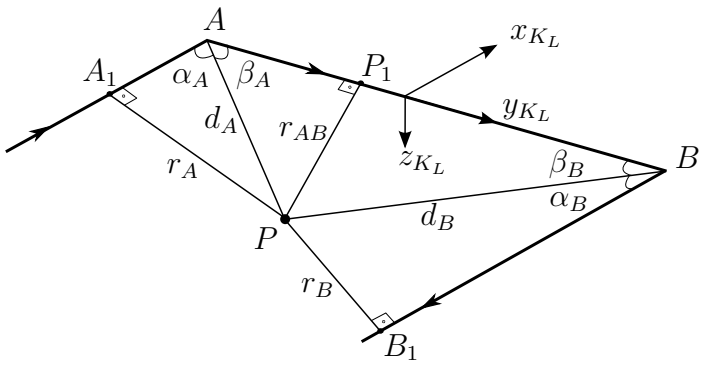

Figure 6.2: Angular and distance relations between the point P and the horseshoe vortex. Equations (6.3) to (6.5) are defined based on this figure.

$$\left(\boldsymbol{r}^{LF}\right)_{K_L} = \begin{bmatrix} x^{LF} \\ y^{LF} \\ z^{LF} \end{bmatrix}_{K_L} \tag{6.9}$$

$$\left(\boldsymbol{r}^{AL}\right)_{K_L} = \begin{bmatrix} 0 \\ b'_L/2 \\ 0 \end{bmatrix}_{K_L} \tag{6.10}$$

$$\left(\boldsymbol{r}^{BL}\right)_{K_L} = \begin{bmatrix} 0 \\ -b'_L/2 \\ 0 \end{bmatrix}_{K_L} \tag{6.11}$$

$$\left(\boldsymbol{r}^{FP}\right)_{K_L} = \boldsymbol{M}_{K_L B_F} \left(\boldsymbol{r}^{FP}\right)_{B_F} = \boldsymbol{M}_{K_L B_F} \begin{bmatrix} x^{FP} \\ y^{FP} \\ z^{FP} \end{bmatrix}_{B_F} \tag{6.12}$$

In eq. (6.12), the term $\boldsymbol{M}_{K_L B_F}$ is the transformation matrix from the follower body-fixed frame, B_F to the leader kinematic frame, K_L. During the formation flight of two aircraft on the same path, both airframes are regarded as parallel and non-rotating with respect to each other. Therefore it is assumed that B_F-frame is parallel with respect to K_L-frame. Based on this assumption, which is followed by Pachter et al. [41], the transformation matrix $\boldsymbol{M}_{K_L B_F}$ becomes identity matrix and the components of $(\boldsymbol{r}^{FP})_{B_F}$ becomes equal to those of $(\boldsymbol{r}^{FP})_{K_L}$.

Inserting eqs. (6.9) to (6.12) into eqs. (6.7) and (6.8), with the above assumption that $\boldsymbol{M}_{K_L B_F} = I$, eqs. (6.13) and (6.14) are obtained.

$$\left(\boldsymbol{r}^{AP}\right)_{K_L} = \begin{bmatrix} x^{LF} + x^{FP} \\ y^{LF} + b'_L/2 + y^{FP} \\ z^{LF} + z^{FP} \end{bmatrix}_{K_L} \tag{6.13}$$

$$\left(\boldsymbol{r}^{BP}\right)_{K_L} = \begin{bmatrix} x^{LF} + x^{FP} \\ y^{LF} - b'_L/2 + y^{FP} \\ z^{LF} + z^{FP} \end{bmatrix}_{K_L} \tag{6.14}$$

Using eqs. (6.13) and (6.14), all the unknown terms in eqs. (6.3) to (6.5) can now be defined as given below. By applying law of sines on AA_1P triangle of figure 6.2, the relation $\sin\alpha_A = r_A/d_A$ can be obtained. By combining this with the trigonometric relation $\sin^2\alpha_A + \cos^2\alpha_A = 1$, the cosine term in eq. (6.3) can be written as eq. (6.15).

$$\cos\alpha_A = \sqrt{1 - r_A^2/d_A^2} \tag{6.15}$$

Since eq. (6.15) can only define the $\cos\alpha_A$ in the interval of $[0, 90°]$, it is rewritten in eq. (6.16) using the x-component of eq. (6.13). In this way, it also defines the $\cos\alpha_A$ in the ranges, where α_A is greater than 90°.

$$\cos\alpha_A = \begin{cases} \sqrt{1 - r_A^2/d_A^2}, & \text{if } x^{LF} + x^{FP} \leq 0 \\ -\sqrt{1 - r_A^2/d_A^2}, & \text{if } x^{LF} + x^{FP} > 0 \end{cases} \tag{6.16}$$

Using eq. (6.13), the r_A and d_A terms can be defined as given in eqs. (6.17) and (6.18).

$$r_A^2 = (y^{LF} + b'_L/2 + y^{FP})^2 + (z^{LF} + z^{FP})^2 \tag{6.17}$$

$$d_A^2 = (x^{LF} + x^{FP})^2 + r_A^2 \tag{6.18}$$

By applying law of sines on BB_1P triangle and using the components of eq. (6.14), eqs. (6.19) to (6.21) can be obtained in the same fashion shown above.

$$\cos\alpha_B = \begin{cases} \sqrt{1 - r_B^2/d_B^2}, & \text{if } x^{LF} + x^{FP} \leq 0 \\ -\sqrt{1 - r_B^2/d_B^2}, & \text{if } x^{LF} + x^{FP} > 0 \end{cases} \tag{6.19}$$

$$r_B^2 = (y^{LF} - b'_L/2 + y^{FP})^2 + (z^{LF} + z^{FP})^2 \tag{6.20}$$

$$d_B^2 = (x^{LF} + x^{FP})^2 + r_B^2 \tag{6.21}$$

Similarly, by applying law of sines on AP_1P and BP_1P triangles and using the components of eqs. (6.13) and (6.14), eqs. (6.22) to (6.24) can be obtained.

$$\cos\beta_A = \begin{cases} \sqrt{1 - r_{AB}^2/d_A^2}, & \text{if } y^{LF} + b'_L/2 + y^{FP} \geq 0 \\ -\sqrt{1 - r_{AB}^2/d_A^2}, & \text{if } y^{LF} + b'_L/2 + y^{FP} < 0 \end{cases} \tag{6.22}$$

$$\cos\beta_B = \begin{cases} \sqrt{1 - r_{AB}^2/d_B^2}, & \text{if } y^{LF} - b'_L/2 + y^{FP} \leq 0 \\ -\sqrt{1 - r_{AB}^2/d_B^2}, & \text{if } y^{LF} - b'_L/2 + y^{FP} > 0 \end{cases} \tag{6.23}$$

$$r_{AB}^2 = (x^{LF} + x^{FP})^2 + (z^{LF} + z^{FP})^2 \tag{6.24}$$

Finally, taking the vortex directions of rotation (figures 6.1 and 6.2) into account and using the components of eqs. (6.13) and (6.14), the unit vectors of the induced velocities from each vortex filament can be written. Noting that the semi-infinite vortex filaments only induce velocities in the yz-plane of the K_L-frame and the finite vortex filament only induces velocity in the xz-plane of the K_L-frame, the unit vectors $\hat{\boldsymbol{e}}_A$, $\hat{\boldsymbol{e}}_B$ and $\hat{\boldsymbol{e}}_{AB}$ are defined below.

$$(\hat{\boldsymbol{e}}_A)_{K_L} = \frac{1}{r_A} \begin{bmatrix} 0 \\ -z^{LF} - z^{FP} \\ y^{LF} + b'_T/2 + y^{FP} \end{bmatrix}_{K_L} \tag{6.25}$$

$$(\hat{\boldsymbol{e}}_B)_{K_L} = \frac{1}{r_B} \begin{bmatrix} 0 \\ z^{LF} + z^{FP} \\ -y^{LF} + b'_T/2 - y^{FP} \end{bmatrix}_{K_L} \tag{6.26}$$

$$(\hat{\boldsymbol{e}}_{AB})_{K_L} = \frac{1}{r_{AB}} \begin{bmatrix} z^{LF} + z^{FP} \\ 0 \\ -x^{LF} - x^{FP} \end{bmatrix}_{K_L} \tag{6.27}$$

Equations (6.16) to (6.27) defines all the terms required for eq. (6.6), with which the total induced velocity at any point can be calculated. Inserting the terms defined by eqs. (6.16) to (6.27) in eq. (6.6), the total induced velocity, $(\boldsymbol{V}_w)_{K_L}$, will be the function of $\boldsymbol{r}^{LF}$ and $\boldsymbol{r}^{FP}$.

Figure 6.3 visualizes the flow field behind the leader aircraft on the yz-plane of the leader frame. The flow field is plotted using Equation (6.6), using the terms defined in Equations (6.16) to (6.27). The plot is generated by evaluating Equation (6.6) at multiple points on the yz-plane at $x = -b_L$. In the figure, the horizontal gray-black line represents the wing of the leader aircraft, seen from behind. The arrow directions show the direction of the air flow. The lengths of the arrows represent the magnitude of the local flow velocity, relative to the magnitudes of the neighboring flow velocities.

Figure B.1 is included in Appendix B, which also show the flow field behind the leader aircraft, but at a much closer distance of $x = -0.15b_L$. The main difference between the flow fields shown in Figures 6.3 and B.1 is the effect of the bound vortex. In Figure B.1, the effect of the bound vortex is visible in form of a stronger downwash between the wingtips.

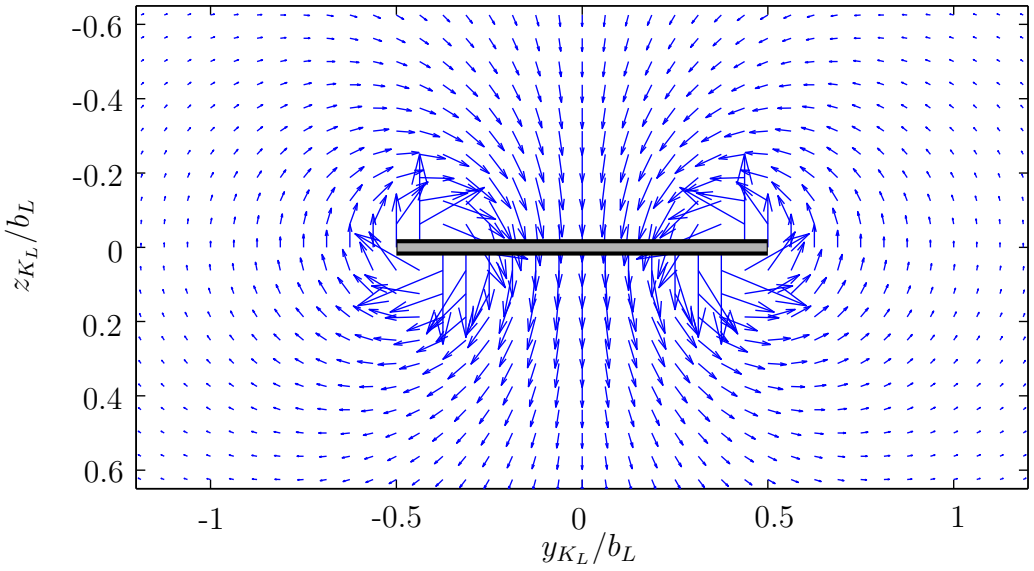

Figure 6.3: Leader wake flow field seen from behind the wing, at $x = -b_L$.

6.2 Effective Aerodynamic Disturbance Acting on the Follower Aircraft

6.2.1 Translational Components

As stated above, as the follower-to-leader relative position $\boldsymbol{r}^{LF}$ changes, the induced velocity around the follower aircraft will change. Furthermore, for any given $\boldsymbol{r}^{LF}$, the vortex-induced velocities will act differently at different points over the surfaces of the follower aircraft, as the follower aircraft is not a point mass. Therefore, in order to approximate the effective aerodynamic disturbance that the follower aircraft experiences, the induced velocity effects are averaged over the surfaces of the follower aircraft. Here the term averaging means, for any given $\boldsymbol{r}^{LF}$, evaluating $(\boldsymbol{V}_w)_{K_L}$ at different $\boldsymbol{r}^{FP}$ and calculating the mean disturbance $(\overline{\boldsymbol{V}}_w)_{K_L}$.

For the averaging, one option would be applying the mean value theorem [137], which requires analytical integration of the components of $(\boldsymbol{V}_w)_{K_L}$ with respect to the respective components of $\boldsymbol{r}^{FP}$. However, due to the polynomial terms in the denominators of the components of $(\boldsymbol{V}_w)_{K_L}$, the analytical integration produces results with inverse hyperbolic tangent terms, which only produces real values for its arguments lying in the interval of $[-1, 1]$. Since this property may produce physically non-meaningful results for specific values of inter-aircraft relative position vector, $\boldsymbol{r}^{LF}$, instead of analytical integration, numerical integration is used.

The numerical integration of $(\boldsymbol{V}_w)_{K_L}$ with respect to $\boldsymbol{r}^{FP}$ means the integration of u_w, v_w and w_w with respect to x^{FP}, y^{FP} or z^{FP}, which is described below in detail. This numerical integration requires the step size of the corresponding integration

variable (x^{FP}, y^{FP} or z^{FP}) to be small enough, for producing results as close to those of the analytical integration as possible [137]. In other words, the greater the number of integration stations, the more accurate the numerical integration will be. This makes the numerical integration process computationally expensive, and if the calculations are carried out during the formation flight simulation, it slows down the entire simulation substantially. Therefore, in order to achieve an accurate numerical integration without slowing down the simulation, the average disturbance values acting on the follower are calculated prior to the formation flight simulation runs at predetermined group of points, i.e. $\boldsymbol{r}^{LF}$ locations, around the leader aircraft. The calculated disturbance data are recorded as look-up table data. Then during the formation flight simulations, the averaged vortex disturbance effects are taken from the look-up table data, generated for different values of inter-aircraft relative position $\boldsymbol{r}^{LF}$.

For the generation of the look-up table data, first the nodes around the leader aircraft are determined, at which the averaged induced velocities acting on the follower aircraft will be calculated. Three sets of nodes are used. The first set of nodes are located within an imaginary rectangular prism around the leader aircraft, which is defined by the intervals, $|x^{LF}| \leq 0.5b_L$, $|y^{LF}| \leq 1.5b_L$ and $|z^{LF}| \leq b_L$. Within this prism the nodes are the densest, with a node-to-node distance of $b_L/32$ along each dimension. This is because, at the points close to the leader aircraft wingtips, the change of the magnitude and the direction of the airflow per unit distance is the highest, which means a more nonlinear flow pattern. Therefore smaller distance between the nodes are required in order to capture these nonlinearities. At stations further away from the leader aircraft wingtips, the change of the magnitude and direction of the vortex-induced airflow becomes weaker per unit distance. Therefore, the flow properties can still be captured by selection of sparser grid points. So for the second set of nodes, sparser grid points are used from the inner rectangular prism defined above, outwards up to the inner boundary of a greater rectangular prism defined by the intervals given as $|x^{LF}| \leq 3b_L$, $|y^{LF}| \leq 4b_L$ and $|z^{LF}| \leq 3b_L$. These sparser grid points are distributed with a separation of $b_L/2$ along each dimension. For the third set of nodes, another rectangular prism is used, which is defined by $|x^{LF}| \leq 8b_L$, $|y^{LF}| \leq 8b_L$ and $|z^{LF}| \leq 8b_L$. As the last set of nodes, the rectangular prism's corners and edge-midpoints are selected. This last set of nodes defines the boundary of the grid. The main reason of using these nodes are for the look-up table to easily interpolate from the values around the leader to zero at the boundary. At these boundary points and further apart from them, the induced velocities are negligibly small.

At each node, the non-averaged wind velocities acting on different sections of the follower aircraft will only be the function of $\boldsymbol{r}^{FP}$, that is: $u_w = u_w(x^{FP}, y^{FP}, z^{FP})$, similarly, $v_w = v_w(x^{FP}, y^{FP}, z^{FP})$, and $w_w = w_w(x^{FP}, y^{FP}, z^{FP})$. Therefore for each node, the effective wind velocities acting on the follower aircraft is calculated as

follows. The x-component of the total induced velocity, u_w, which is also addressed here as *frontwash*, is averaged over its values along the follower aircraft wingspan and the height of the aircraft from the bottom of the follower's fuselage to the tip of the vertical stabilizer. Equations (6.28) and (6.29) show averaging of the frontwash values at different stations along left and right wings of the follower aircraft respectively. Equations (6.30) and (6.31) show the average frontwash along the total height of the aircraft, including the vertical tail and fuselage height. The term n denotes the number of points on which the average is calculated from one wing tip to another. The term m are the number of nodes along the vertical tail height of the follower aircraft and the term a is the number of nodes along the height of the follower fuselage. The terms h_{vt_F} and h_{f_F} are the height of the vertical stabilizer and the fuselage respectively. They are also shown on figure 6.1. Using the average frontwash at different sections of the follower aircraft (eqs. (6.28) to (6.31)) the effective frontwash, $\overline{u}_w$, acting at the follower aircraft is calculated as given in in eq. (6.32).

$$\overline{u}_{w,left} = \frac{1}{n}\sum_{i=1}^{n} u_w(0, y_i, 0), \text{ with } y_1 = -b_F/2,\ y_n = 0 \tag{6.28}$$

$$\overline{u}_{w,right} = \frac{1}{n}\sum_{i=1}^{n} u_w(0, y_i, 0), \text{ with } y_1 = 0,\ y_n = b_F/2 \tag{6.29}$$

$$\overline{u}_{w,up} = \frac{1}{m}\sum_{i=1}^{m} u_w(0, 0, z_i), \text{ with } z_1 = -h_{vt_F},\ z_m = 0 \tag{6.30}$$

$$\overline{u}_{w,down} = \frac{1}{a}\sum_{i=1}^{a} u_w(0, 0, z_i), \text{ with } z_1 = 0,\ z_a = h_{f_F} \tag{6.31}$$

$$\overline{u}_w = \frac{1}{4}\left(\overline{u}_{w,left} + \overline{u}_{w,right} + \overline{u}_{w,up} + \overline{u}_{w,down}\right) \tag{6.32}$$

The *sidewash*, v_w, is averaged over its values along the length of the follower aircraft and the total height of the vertical tail and fuselage. Equations (6.33) and (6.34) show the averaging of the sidewash on the points along the rear and front parts of the fuselage. Equations (6.35) and (6.36) show the averaging of the sidewash on the points along the vertical stabilizer and fuselage height. The terms c and d denote the number of nodes selected on the rear and front parts of the fuselage respectively. The terms l_{r_F} and l_{f_F} are the length of the rear and front fuselage sections respectively, and are also shown on figure 6.1. Equation (6.37) shows the calculation of the effective sidewash acting on the follower aircraft, $\overline{v}_w$.

$$\overline{v}_{w,rear} = \frac{1}{c}\sum_{i=1}^{c} v_w(x_i, 0, 0), \text{ with } x_1 = -l_{r_F},\ x_c = 0 \tag{6.33}$$

$$\overline{v}_{w,front} = \frac{1}{d}\sum_{i=1}^{d} v_w(x_i, 0, 0), \text{ with } x_1 = 0,\ x_d = l_{f_F} \tag{6.34}$$

$$\overline{v}_{w,up} = \frac{1}{m}\sum_{i=1}^{m} v_w(0, 0, z_i), \text{ with } z_1 = -h_{vt_F},\ z_m = 0 \tag{6.35}$$

$$\overline{v}_{w,down} = \frac{1}{a}\sum_{i=1}^{a} v_w(0, 0, z_i), \text{ with } z_1 = 0,\ z_a = h_{f_F} \tag{6.36}$$

$$\overline{v}_w = \frac{1}{4}\left(\overline{v}_{w,rear} + \overline{v}_{w,front} + \overline{v}_{w,up} + \overline{v}_{w,down}\right) \tag{6.37}$$

The *downwash* or *upwash*, w_w, is averaged over the wingspan and length of the follower aircraft. Equations (6.38) and (6.39) show the averaging of the downwash over the rear and front sections of the follower fuselage. Equations (6.40) and (6.41) show the averaging of the downwash over the left and right wings. Equation (6.42) shows the effective downwash acting on the follower aircraft.

$$\overline{w}_{w,rear} = \frac{1}{c}\sum_{i=1}^{c} w_w(x_i, 0, 0), \text{ with } x_1 = -l_{r_F},\ x_c = 0 \tag{6.38}$$

$$\overline{w}_{w,front} = \frac{1}{d}\sum_{i=1}^{d} w_w(x_i, 0, 0), \text{ with } x_1 = 0,\ x_d = l_{f_F} \tag{6.39}$$

$$\overline{w}_{w,left} = \frac{1}{n}\sum_{i=1}^{n} w_w(0, y_i, 0), \text{ with } y_1 = -b_L/2,\ y_n = 0 \tag{6.40}$$

$$\overline{w}_{w,right} = \frac{1}{n}\sum_{i=1}^{n} w_w(0, y_i, 0), \text{ with } y_1 = 0,\ y_n = b_L/2 \tag{6.41}$$

$$\overline{w}_w = \frac{1}{4}\left(\overline{w}_{w,rear} + \overline{w}_{w,front} + \overline{w}_{w,left} + \overline{w}_{w,right}\right) \tag{6.42}$$

Equations (6.32), (6.37) and (6.42) show the effective translational induced velocities acting on the follower aircraft. However, modeling the wake disturbance on the follower aircraft only by translational induced velocities does not fully cover the scope of the disturbance which is present in reality. Since the translational wake vortex disturbance act on the different sections of the follower aircraft differently, there will be airflow gradients over the dimensions of the follower aircraft, which will be nonzero [110]. Due to these gradients, rotational induced velocities will also be present as disturbances affecting the follower aircraft. The calculation of these rotational induced velocity components is presented in the following section.

6.2.2 Rotational Components

Based on the relations shown by Dogan et al. [110], the velocity component gradients along the different dimensions of the follower aircraft can be written as given below. The axes components x, y and z are that of the follower aircraft's body-fixed reference frame, which are shown without subscripts for the sake of simplicity.

The gradients shown in Equations (6.43) and (6.44) represent the change of front-wash along the y and z-axes of the body-fixed frame of the follower aircraft.

$$\frac{\partial u_w}{\partial y} = \frac{1}{b_F/2} \left(\overline{u}_{w,right} - \overline{u}_{w,left} \right) \tag{6.43}$$

$$\frac{\partial u_w}{\partial z} = \frac{1}{(h_{vt_F} + h_{f_F})/2} \left(\overline{u}_{w,down} - \overline{u}_{w,up} \right) \tag{6.44}$$

Equations (6.45) and (6.46) show the sidewash gradients representing the change of sidewash along the x and z-axes of the follower aircraft body-fixed frame.

$$\frac{\partial v_w}{\partial x} = \frac{1}{(l_{f_F} + l_{r_F})/2} \left(\overline{v}_{w,front} - \overline{v}_{w,rear} \right) \tag{6.45}$$

$$\frac{\partial v_w}{\partial z} = \frac{1}{(h_{vt_F} + h_{f_F})/2} \left(\overline{v}_{w,down} - \overline{v}_{w,up} \right) \tag{6.46}$$

The downwash gradients, which represent the change of downwash along the x and y-axes of the follower aircraft body-fixed frame, are shown in Equations (6.47) and (6.48).

$$\frac{\partial w_w}{\partial x} = \frac{1}{(l_{f_F} + l_{r_F})/2} \left(\overline{w}_{w,front} - \overline{w}_{w,rear} \right) \tag{6.47}$$

$$\frac{\partial w_w}{\partial y} = \frac{1}{b_F/2} \left(\overline{w}_{w,right} - \overline{w}_{w,left} \right) \tag{6.48}$$

The average induced velocity terms, which are required by the gradient equations are already defined above in eqs. (6.28) to (6.41). Finally, using the gradient equations shown above, the effective rotational induced velocities acting on the follower aircraft can be defined [110] as given below.

$$\overline{p}_w = \frac{\partial w_w}{\partial y} - \frac{\partial v_w}{\partial z} \tag{6.49}$$

$$\overline{q}_w = \frac{\partial u_w}{\partial z} - \frac{\partial w_w}{\partial x} \tag{6.50}$$

$$\overline{r}_w = \frac{\partial v_w}{\partial x} - \frac{\partial u_w}{\partial y} \tag{6.51}$$

Equations (6.49) to (6.51) show the induced roll, pitch and yaw velocities acting on the follower aircraft. Together with eqs. (6.32), (6.37) and (6.42), they define the effective aerodynamic disturbance that acts on the follower aircraft due to the wake of the leader aircraft.

Figure 6.4 shows the components of the effective wake disturbance that the follower aircraft experiences, based on its relative position with respect to the leader aircraft. The longitudinal separation between the aircraft is kept fixed at $x^{LF} = -2b_L$. The disturbances shown in figure 6.4 are generated with the lower-scale leader and follower aircraft pair, which fly at an altitude of 400 meters with the speed of 35 m/s. The effective wake disturbance acting on the follower aircraft at the longitudinal separation $x^{LF} = -b_L$ is shown on figure B.2 on page 164. The flight condition and the scale of the aircraft remain the same as those for figure 6.4.

Figure 6.4 shows that, at the longitudinal separation of $x^{LF} = -2b_L$, the main disturbances acting on the follower aircraft are the sidewash, upwash and the roll disturbance effects. At this longitudinal separation, the effect of the bound vortex filament, which is placed along the span of the leader's wing, is negligible. Therefore, the semi-infinite vortices spanning downstream from the tips of the leader's wing dominate the flow field. On the sidewash plot, figure 6.4(c), it can be seen that, the follower, who follows the leader at a lower vertical position and from behind, will experience a sidewash to the right (positive sidewash, i.e., along its y_B-axis) if the follower is at the right-hand side of the leader. If the follower is at the left-hand side of the leader, it experiences a sidewash to the left. The experienced sidewash reaches its maximum value if the follower is laterally aligned with the vortex cores. As the follower aircraft increase its vertical distance with respect to the leader, the magnitude of the disturbance reduces. If the follower aircraft is exactly at the same level as the leader, figure 6.4(c) shows no sidewash. This is because, the flow magnitudes on the leader's yz-plane at upper and lower sides of the leader's wing are about the same but opposite in direction, which can also be seen in figure 6.3. This flow pattern yields zero effective sidewash, when summed along the total height of the follower aircraft.

In figure 6.4(e) the effective downwash acting on the follower aircraft is shown. It can be seen that if the follower is laterally in between the tips of the leader's wing, it experiences a positive downwash, i.e., a downward airflow. If the follower aircraft is at the same vertical position as the leader or slightly below, it experiences a negative downwash in the left-hand-side and right-hand-side regions of the left and right wings respectively. This negative downwash is an upward airflow, which reduces the induced drag of the follower aircraft and therefore enables it to cruise more efficiently. The figure shows that for $z^{LF} = 0$, the downwash curve shows steep changes with respect to the lateral relative position. This is due to the highly nonlinear airflow induced by the trailing vortices, that is, the airflow changing direction over a short distance. As the vertical separation increases, the follower aircraft moves apart from the trailing vortex cores, where the flow pattern nonlinearities are high. Therefore the downwash

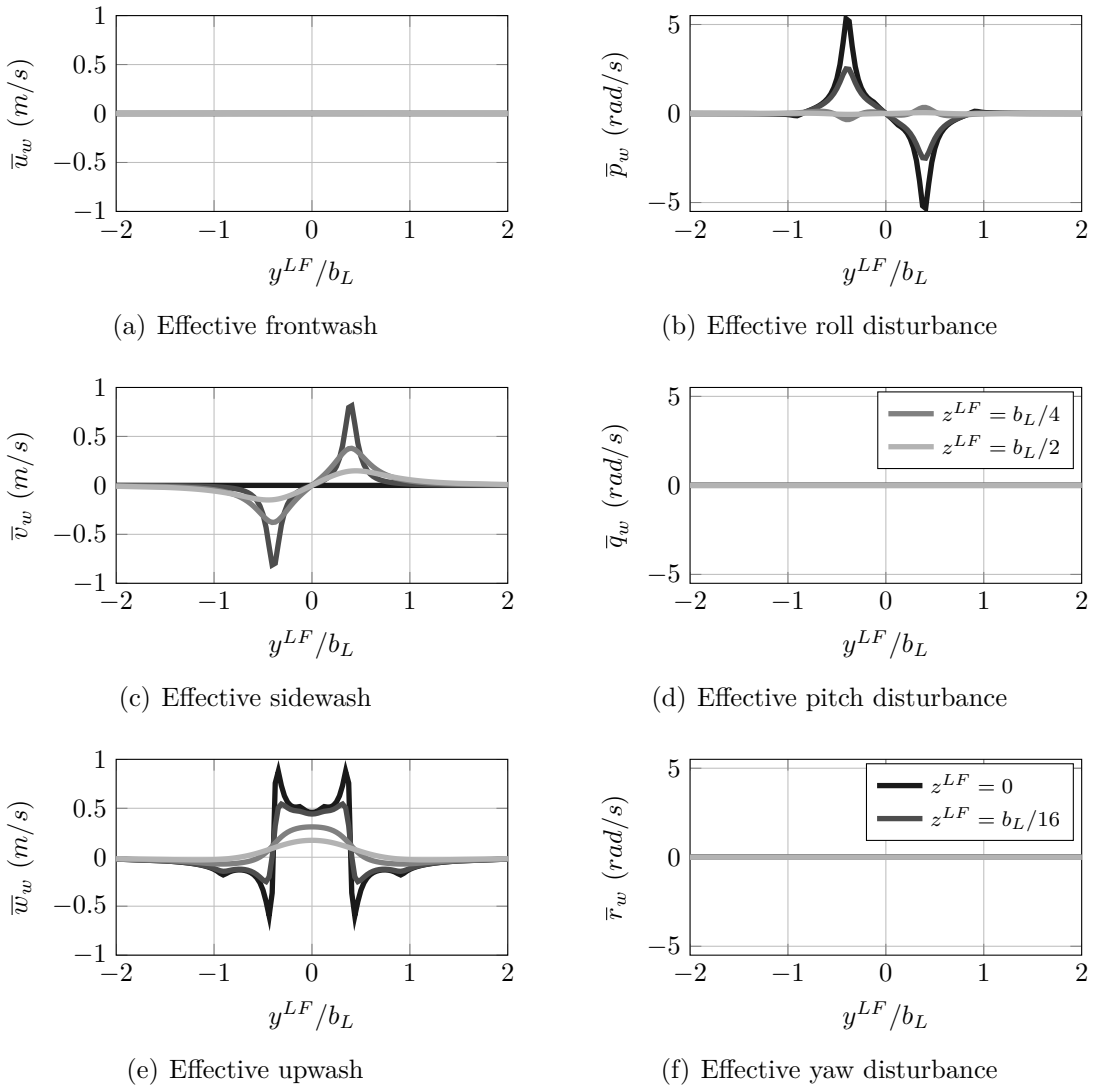

(a) Effective frontwash

(b) Effective roll disturbance

(c) Effective sidewash

(d) Effective pitch disturbance

(e) Effective upwash

(f) Effective yaw disturbance

Figure 6.4: Effective aerodynamic disturbance components acting on the follower aircraft, due to the wake of the leader aircraft, plotted as a function of the follower to leader relative position. The follower to leader longitudinal position is kept fixed at $x^{LF} = -2b_L$.

curves become smoother as the vertical separation between the aircraft increases.

In figure 6.4(b) the change of the effective roll disturbance is shown. Since the aircraft are symmetric laterally, at the $y^{LF} = 0$ location, the induced roll disturbance is zero. At a given vertical separation with respect to the leader, the highest roll disturbance is experienced by the follower, if it is laterally aligned with the trailing vortex lines. The roll disturbance takes its maximum value, if the vertical separation is zero. With increasing vertical separation the roll disturbance magnitude reduces and eventually reaches zero, as shown by the curve of $z^{LF} = b_L/2$ in figure 6.4(b). If the follower aircraft is in the vicinity of the trailing vortex cores, a positive roll disturbance acts on the follower if it is on the left hand side of the leader's longitudinal

axis. In a positive roll disturbance, the follower is in the tendency to roll to the right. On the right hand side of the leader aircraft, the follower aircraft experiences a roll disturbance to the left, if it is in the vicinity of the right-side trailing vortex. As shown by the curve of $z^{LF} = b_L/4$ in figure 6.4(b), the direction of the roll disturbance is reversed, if the follower aircraft is sufficiently below the leader aircraft and laterally aligned with the vortex cores. This is mainly due to the vortex-induced airflow still affecting the vertical stabilizer of the follower aircraft, although its fuselage and wings are effectively outside the rotating flow region.

Figure B.2 on page 164 shows the wake-induced disturbance acting on the follower aircraft at a longitudinal separation of $x^{LF} = -b_L$. The comparison of figure 6.4 with figure B.2 shows no noticeable change on the disturbance patterns and magnitudes. This is mainly due to the fact that the effect of the bound vortex cannot be sensed at both longitudinal separations, $x^{LF} = -2b_L$ and $x^{LF} = -b_L$.

Chapter 7

Simulation-Based Analysis: Design and Results

Along with Chapter 8, this chapter presents the answer to the main research question stated in Section 1.3. The chapter begins with the introduction of the simulation-based tests, which are designed to obtain answers to the research question. The simulation's inputs, outputs and configuration parameters, which are of relevance to the analysis, are stated. The simulation results are then presented in graphical form for both lower-scale and higher-scale aircraft. The corresponding discussions are presented alongside the simulation results.

This chapter is built upon Section 1.3, in which the problem statement and the methodology followed in this work are given. As the discussions and justifications regarding the approach to the problem are already presented in Section 1.3, they are not repeated in this chapter for brevity.

7.1 Simulation-Based Analysis Methodology

7.1.1 Simulation Environment Set up and Overview

Recalling from Chapter 1, the main parameters, whose effects on the follower's formation keeping performance are investigated, are the following specifications of the leader-follower relative position information: Error magnitude, sampling period, and delay. These entities are used as the *parameters* of the simulation-based analysis and are also addressed as the *independent variables* of the analysis. The simulation-based analysis relies on varying these independent variables among repeated runs of the simulation. By this means the effects of the independent variables on the formation flight performance are found. The performance of the formation flight is characterized by the maximum position error during a predefined duration of the formation flight.

Figure 7.1 depicts the overview of the simulation environment, which was set up

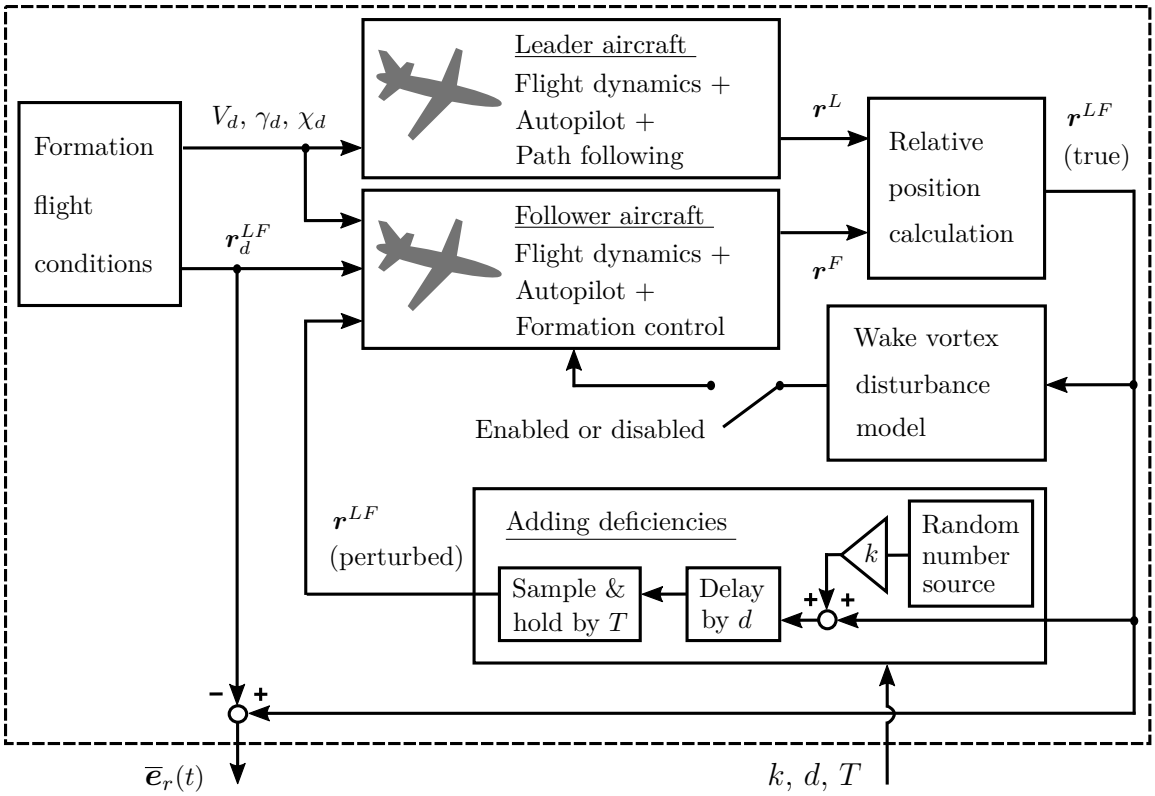

Figure 7.1: Simulation environment, set up for analyzing the effects of the independent variables on the performance of formation flight. Shown are only the signals, which are of direct relevance to the analysis.

and used in order to carry out the analysis outlined above. The simulation environment includes closed loop leader and follower aircraft models, which are made up of their nonlinear flight dynamics, driven by the automatic pilots and corresponding guidance algorithms. The leader and the follower aircraft are commanded to fly a common formation speed, at a predefined constant altitude ($\gamma_d = 0$) and a common course. Additionally, the follower aircraft is commanded to maintain the formation at a desired relative position $\left(\boldsymbol{r}_d^{LF}\right)$ with respect to the leader aircraft. These conditions of the formation flight are kept constant for both scales of aircraft in this work.

Using the *actual* or *true* positions of the leader and follower aircraft, the true relative position of the follower with respect to the leader aircraft is calculated using eqs. (5.9) and (5.10). The relative position vector's components are expressed in the leader's kinematic reference frame. The subscript addressing the reference frame, on which the vector's components are decomposed, is not shown for simplicity. The difference between the desired relative position and the actual relative position is called actual or true relative position error. This term is shown by $\overline{\boldsymbol{e}}_r$ in order to distinguish it from the relative position error, which is seen by the follower's formation flight controller. The true relative position and the true relative position error do not

contain the deficiencies of the relative position vector, that the follower aircraft's formation controller processes. The term $\overline{\boldsymbol{e}}_r$, which is a vector with components $\overline{e}_x$, $\overline{e}_y$ and $\overline{e}_z$, is recorded as a time series at the end of each simulation run in order to assess the performance of the formation flight. The scalar term $\overline{e}_r$ is also used in the subsequent sections of the text, in order to refer to any component of the vector $\overline{\boldsymbol{e}}_r$.

As shown in figure 7.1 the simulation environment includes a module, which adds the predetermined amounts of deficiencies to the relative position information. The output of the module is the *perturbed* relative position information, which includes the added deficiencies. The perturbed relative position information is then processed by the follower aircraft's formation controller. The module receives the actual values of the deficiencies as input. The values of the deficiencies are the parameters of the simulation and they are varied within predefined ranges among each individual run of the simulation sets. The parameters remain constant during each run of the simulation, and they are shown by the terms k, d, and T. The term d represents the delay of the relative position information, which is measured in seconds. The term T is the period of the sample and hold action, measured in seconds. The term k is a dimensionless, non-negative real number, controlling the magnitude of the error added to the relative position information. The module uses a random number generator as the error source, which generates random numbers of Gaussian probability distribution. The term k is multiplied by the output of the random number generator, before the addition of the error to the true relative position. Therefore, any value of the parameter k, which is less than 1 but greater than zero, attenuates the error magnitude added to the relative position information. For $k = 0$, no error is added to the relative position information. For the values of k, which are greater than 1, the random error values are amplified by the factor given by k. As the relative position information is a vector with components on longitudinal, lateral and vertical axes of the leader kinematic reference frame, the random number source generates the numbers for all three axes. The numbers generated for all axes are uncorrelated with each other, by means of initializing each random number generator with different seeds. However, the term k affects the magnitudes of all the components commonly and in the same fashion.

The simulation environment also includes the wake disturbance model, which generates the wind velocities acting on the follower aircraft, based on the true relative position between the aircraft. The simulations were run with both wake vortex disturbance disabled and enabled. The initial sets of simulation runs were carried out with disabled wake vortex effects in order to solely obtain the effects of the independent variables on the formation flight, without the interfering effects of external disturbances. Simulations with the wake vortex effects were performed in order to find out the impact of this external disturbance on the results obtained without the wake vortex disturbance.

In case of disabled wake vortex disturbance, the commanded relative position of

the aircraft does not play a role on the formation flight performance. That is, the same result will be obtained if the follower aircraft is commanded to maintain the formation at different relative positions with respect to the leader. However, in a simulation with the wake vortex effects, the relative position of the aircraft during the formation flight gain importance as an additional parameter affecting the performance of the formation flight. This is due to the nonuniform flow field at the leader's wake, which produces different disturbance on the follower aircraft at different relative positions. A separate analysis for describing the relation between the formation keeping performance and the formation relative position is beyond the scope of this work. In order to limit the parameters of the simulation-based analysis only to those characterizing the relative position information, a single commanded relative position is used in this work. The commanded relative position of the formation was selected as the relative position, which is used during probe and drogue aerial refueling. Mao and Eke [138] state the typical separation between the tanker and receiver aircraft during the aerial refueling as approximately two wingspans of longitudinal and a quarter wingspan of vertical separation with the receiver below and aft of the tanker and the aircraft are laterally aligned.

7.1.2 Simulation Parameters

Some general requirements were set for the determination of the ranges of the simulation parameters. It is desired to have a wide enough range for each parameter, so that the effect of each parameter becomes clearly visible on the performance of the formation keeping. Since for each parameter value combination one complete run of formation flight simulation is performed, the number of values for each parameter directly affects the overall simulation time. Therefore, in order to keep the time required for the analysis in reasonable limits, as well as for the efficient use of the computational resources, the total number of values for the parameters are desired to be small. The parameter upper limits were selected low enough, in order to ensure that the formation keeping dynamics always remain stable. Additionally, it was aimed to have parameter upper limits, which are sufficiently small, in order not to let the deficiencies cause high position errors during automated formation flight, which would be safety-critical in practical formation flight applications. Therefore previous formation flight applications were taken as basis for selecting the parameter values. Recalling that table 1.1 summarizes the relative position information characteristics obtained from available means of relative position information gathering techniques for formation flight, the values in table 1.1 were regarded as reference for the determination of the parameter upper limits. The parameters were selected as presented in table 7.1.

Table 7.1 presents the sets of values for each parameter in terms of their lower limits, upper limits and the step sizes. The sets of values for each parameter start

Parmeter (unit)	Lower limit	Step size	Upper limit
k (–)	0	Wake disabled: $0.\bar{3}$ and $0.\bar{6}$ Wake enabled: $0.\bar{3}$	1 and 2 1
d (s)	0	0.01	Lower-scale: 0.6 Higher-scale: 1
T (s)	0.01	0.01	1

Table 7.1: Ranges of the simulation's parameters.

from the lower limit values and span up to the upper limit values by the values of the step sizes. For each parameter, the lower limit values represent the ideal case for the corresponding attribute of the relative position information. For the parameter k, the lower limit, zero, means that no error is added to the true relative position shown on figure 7.1. Therefore the follower's formation controller processes error-free relative position information, in case $k = 0$. Similarly, the lower limit of the delay parameter represents that, delay-free relative position information is used by the follower's formation controller. As stated earlier, the autopilot and the formation flight controller of the follower aircraft execute at a frequency of $100\,Hz$. For the sampling period of the relative position information, the lower limit of $0.01\,s$ represents the case, in which a new relative position information is available to the follower's formation controller, at each instant of its execution. The step size was selected also as $0.01\,s$, so that every element in the value set of the parameter T is an integer multiple of the formation controller's period of execution.

Parameter upper limits were selected based on the values presented in table 1.1. The upper limit of the relative position information delay, as well as the sampling period upper limit were selected for the higher-scale aircraft as $1\,s$, which are double the maximum values of the corresponding parameters shown on table 1.1. This selection was made in order to take into account possible unfavorable effects, which may influence the gathering of the relative position information by the follower aircraft. These effects, such as jamming, or the temporary loss of connection for wireless-based data gathering, are discussed in Section 1.4.2. For the lower-scale aircraft, the upper limit of the delay was selected as $0.6\,s$, in order to avoid system instability due to using up from the system's available delay margin.

For the uppermost value and the step size of the parameter k, two different selections are used. For the simulations with wake vortex effects disabled, the uppermost value was selected as 2. This means that, the error generated by the random number generator is added to the relative position information, with its magnitude doubled. For the increment of the parameter k from the value 0 up to 2, a step size of $0.\bar{6}$ was used. This selection of the step size was solely made for the sake of a clearer depiction of the results. As will be presented in the following sections, simulation

results of different k are plotted on the same figure. Therefore, selecting the step size sufficiently high reduces the number of curves to be plotted and thus enables a clearer distinction between the curves of different k values.

For the simulations with the wake vortex effects enabled, the uppermost value of the parameter k was set to 1. This choice was made in order to reduce the position keeping error of the follower aircraft. Hence, the nearing of the aircraft to the vicinity of the leader's wake vortex cores is avoided. The corresponding parameter step size was selected as $0.\bar{3}$. Using this selection of upper limit and step size values, simulations were performed also with disabled wake vortex disturbance. This way, more directly comparable results with and without the wake vortex effects were obtained.

The standard deviation of the error generated by the random number source was selected as 0.14 meters in order to match the three-dimensional maximum relative position error on the full-scale automated aerial refueling experiment presented by Hansen et al. [53] and Dibley et al. [68]. This value is used in all three axes for the generation of the random error.

7.1.3 Formation Flight Performance Representation

As stated earlier, the performance of the follower aircraft's formation keeping is represented by the maximum position error during a predefined period of automated formation keeping. The maximum position error is determined separately for each axis: Longitudinal, lateral and vertical. Therefore, the time history of the true relative position error, $\overline{\boldsymbol{e}}_r$, is taken from the simulation component-wise as output. The output is recorded for a period of time, before which the transients due to the initialization of the simulation are already died out. An example time history of $\overline{\boldsymbol{e}}_r$, which was obtained from a 10-minute formation flight simulation with higher-scale aircraft is shown in figure 7.2. The simulation was performed with maximum sampling period and minimum delay values shown in table 7.1. Another example time history, which is taken from a simulation with maximum delay and minimum sampling period values, is given in Appendix B, on figure B.3.

In order to obtain the maximum position error during the recorded period of formation flight, the method of simply taking the maximum value in the $\overline{e}_x$, $\overline{e}_y$ and $\overline{e}_z$ time histories is not applied. Because this method ignores the information in the entire data set, except the single points on each $\overline{\boldsymbol{e}}_r$ component, at which the relative position error reaches to a maximum. In order to facilitate the information carried by the entire length of the data, the maximum error is approximated as three times the standard deviation of the time series for each axis, applying the three-sigma rule (Section 3.1). Therefore, the maximum, true relative position error during the formation flight, $\overline{\boldsymbol{e}}_{r,max}$, is represented component-wise as given in eqs. (7.1) to (7.3). The terms $\sigma_{\overline{e}_x(t)}$, $\sigma_{\overline{e}_y(t)}$, and $\sigma_{\overline{e}_z(t)}$ represent the standard deviations of the respective error components during the entire length of the simulation, shown as t.

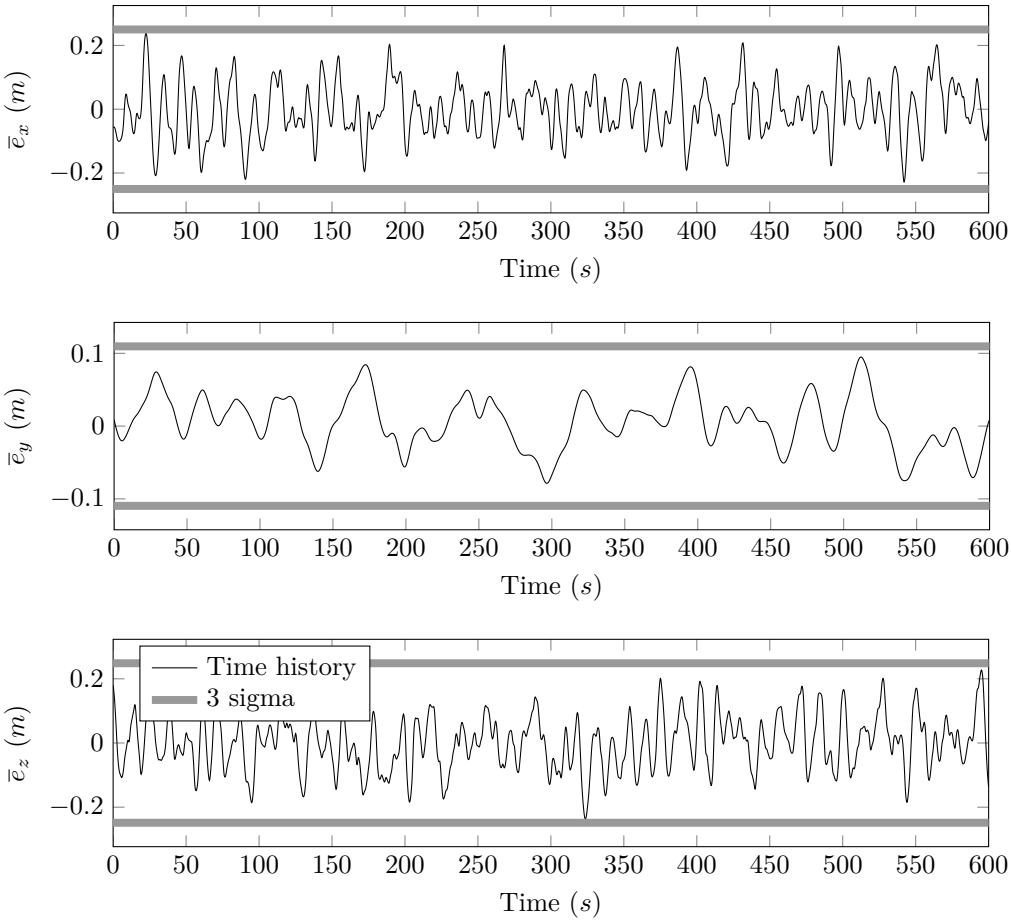

Figure 7.2: Example time history of $\overline{\boldsymbol{e}}_r$ taken from the simulation environment.[1]

$$\overline{e}_{x,max} = 3\,\sigma_{\overline{e}_x(t)} \tag{7.1}$$

$$\overline{e}_{y,max} = 3\,\sigma_{\overline{e}_y(t)} \tag{7.2}$$

$$\overline{e}_{z,max} = 3\,\sigma_{\overline{e}_z(t)} \tag{7.3}$$

Figures 7.2 and B.3 also depict the three-standard-deviation-based maximum approximations to both sides of the time histories. It can be seen that the approximated maximums closely match the actual maximums.

[1]The time history was obtained from a single simulation run, in which the following parameter set was used: $k = 1$, $d = 0\,s$, $T = 1\,s$. Higher-scale aircraft models were used and wake vortex effects were disabled. The lower frequency and magnitude of $\overline{e}_y$ is due to the slower closed-loop dynamics on lateral control channel than that on longitudinal and vertical channels, as depicted by figure 5.2 on page 86. The development of the error, as well as the reaction against the already-developed error is slower due to the slower lateral closed-loop dynamics.

7.1.3.1 Determination of the Simulation Duration

Another aspect of determining the maximum relative position error during the formation flight simulation is the duration of the simulation, based on which the maximum error is calculated. It is desired to obtain a time history from the simulation, which is sufficiently long, in order to allow the deficiencies of the relative position information to manifest their effect on the formation keeping to a more complete extent, as well as, in order to give sufficient time to the follower aircraft to react. On the other hand, it is desired to have a simulation duration, which is sufficiently short, in order to reduce the size of data needs to be stored, as well as, in order to shorten the overall time required for the simulation. Taking the above considerations into account, the time span, during which the simulation output $\overline{\boldsymbol{e}}_r$ is recorded, was iteratively determined as 600 seconds for the higher-scale aircraft. The time span, during which $\overline{\boldsymbol{e}}_r$ is recorded is simply referred to by *simulation duration* throughout the text.

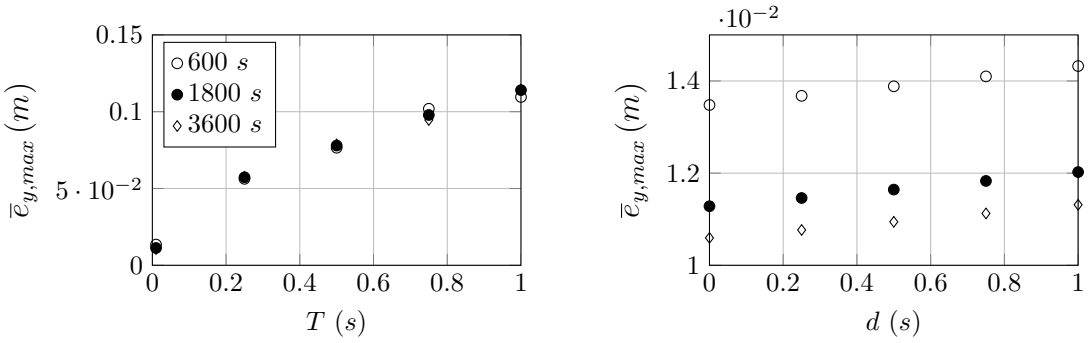

Figure 7.3: Change of determined $\overline{e}_{y,max}$ with respect to different simulation durations. The plots are based on simulations with higher-scale aircraft and $k = 1$.

Figure 7.3 shows the effect of a subset of simulation parameters on the lateral error component, which was determined according to eq. (7.2) with varying durations of simulation. Only the lateral error component is shown here, because the closed loop dynamics is the slowest on the lateral axis. Therefore it requires a longer observation duration for a more complete representation of the formation keeping performance. Equivalent plots for the remaining error components are given in Appendix B on figure B.4.

On figure 7.3, error representations based on 10-minute, 30-minute and 1-hour simulations are shown with different markers. Simulations were performed with higher-scale aircraft, using reduced number of delay and sampling period values at constant k. The plot on the left depicts the change of $\overline{e}_{y,max}$ with respect to the sampling period, T. The figure on the right depicts the change of $\overline{e}_{y,max}$ with respect to the delay d. As shown, at any specific T or d value, the magnitude of $\overline{e}_{y,max}$ varies with different durations of the simulation. This change is present, due to the random nature of the error time history, added to the relative position information that the

follower aircraft's formation controller processes. Due to this randomness and the fact that the $\overline{\boldsymbol{e}}_{r,max}$ is determined using the entire $\overline{\boldsymbol{e}}_r(t)$ recorded, depending on the error time history, the magnitudes of the $\overline{\boldsymbol{e}}_{r,max}$ components can be estimated higher or lower with simulations of different duration. For instance, the determined $\overline{e}_{y,max}$ on a 600-second simulation could be higher than that on a 1800-second simulation, should the error time series contain a section, which causes less position error at the part of the simulation, where $600\,s < t \leq 1800\,s$. This random change of the error magnitude depending on simulation duration can also be exemplified by comparing the right-hand side plots of the y-component on figure 7.3 and the x-component on figure B.4 on page 166. Recalling that the random error sources are initialized with different seeds for each axis, it can be seen on the y-component, that the magnitude of the error is the greatest at the 600-second simulation. However on the x-component, the error magnitude is the lowest at the 600-second simulation.

Unlike the magnitude of the components of $\overline{\boldsymbol{e}}_{r,max}$, the dependency of $\overline{\boldsymbol{e}}_{r,max}$ on the parameters d and T remain nearly unchanged at different durations of the simulation. Therefore, the change of formation keeping performance can be described nearly as well with an 10-minute simulation, as with simulations of 30-minute and 1-hour durations.

Having the duration of the simulation for the higher-scale aircraft determined as 600 seconds, the simulation duration for the lower-scale aircraft was derived from that of the higher-scale aircraft. The closed-loop dynamics of the lower-scale aircraft is approximately 2.5 times faster than that of the higher-scale aircraft on all three axes[2]. This means, that the lower-scale follower aircraft will react to the gathered relative position information in a shorter period of time. Therefore, a shorter simulation duration can be used for obtaining a representation of the formation keeping performance. Hence, the simulation duration of the lower-scale aircraft was selected as 1/2.5 times that of the higher-scale aircraft. This yields a simulation duration of 240 seconds, i.e., 4 minutes.

7.1.3.2 Simulation Data Recording

The final aspect considered as part of the formation keeping performance representation is the frequency, at which the simulation outputs are recorded. The recording rate of the simulation output $\overline{\boldsymbol{e}}_r$ was selected as $5\,Hz$ for the higher-scale aircraft. This recording rate enables the capture of the time variations on all components of $\overline{\boldsymbol{e}}_r$ without causing notable loss of accuracy. A sample simulation with a parameter set

[2]Figure 8.2 on page 127 shows the time responses of the closed-loop formation keeping system to a unit increase of commanded relative position. The figure also depicts the unit step responses of second-order transfer functions, which approximate the system responses. Table 8.1 on page 127 presents the natural frequencies of the fitted transfer functions for each scale of aircraft on each axis. The natural frequencies of the lower-scale aircraft is 2.5 times higher on each axis than those of the higher-scale aircraft.

of $k = 1$, $d = 1\,s$ and $T = 0.01\,s$ showed that, selecting the recording rate 40 times the value mentioned above only brings an accuracy gain of under $0.075\,\%$ on all three components of $\overline{\boldsymbol{e}}_{r,max}$. For the simulations with the lower-scale aircraft, the recording rate was selected 2.5 times faster than that of the higher-scale aircraft, according to the logic outlined above. This corresponds to a recording rate of $12.5\,Hz$.

7.2 Simulation Results

After performing the simulations according to the procedure presented above, in this section, the simulation results are presented in graphical form and discussed.

Figure 7.4 presents the results obtained from the lower-scale aircraft simulation, with wake vortex effects disabled. For each parameter, the value sets given in table 7.1 were used for the simulations. For each set of parameters, the simulation was run once for the specified duration and the corresponding $\overline{\boldsymbol{e}}_{r,max}$ was calculated. In order to observe the effects of the delay and sampling period parameters distinctly, these two parameters were varied independently. That is, for the variation of one parameter, the other parameter was kept constant at its minimum value. The parameter sweeps for the parameters d and T were repeated for each value of k.

Figures 7.4(a)-(f) present the variation of the components of $\overline{\boldsymbol{e}}_{r,max}$, with respect to the change of the parameters k, d and T. The left column of figure 7.4 depicts the effects of the parameters d and k on the components of the $\overline{\boldsymbol{e}}_{r,max}$. On the right column, the variation of the components of $\overline{\boldsymbol{e}}_{r,max}$ is shown, depending on the parameters T and k. On each figure, each data point is based on a separate simulation run with the respective set of parameters. Each figure has multiple sets of data points. Each set corresponds to a different value of k. The data point sets are shown with different darkness levels for distinction. The darkest and the lightest data sets were obtained from the simulations with the uppermost and lowermost values of k respectively. The data sets lying in between correspond to the intermediate values on the value set of the parameter k, with the darker data set corresponding to a higher value of k.

7.2.1 The Effects of d and T on Closed-Loop Dynamics

Before discussing the effects of the parameters k, d and T on $\overline{\boldsymbol{e}}_{r,max}$ based on figure 7.4, this section briefly presents the effects of the parameters d and T on closed-loop system dynamics. This facilitates the discussions presented in subsequent sections.

Figure 7.5 presents the responses of the follower aircraft's formation controller to unit changes in commanded relative positions along x, y and z axes. Three step responses were obtained for each axis from three different formation flight simulations using lower-scale aircraft. Each simulation was performed with different values of the

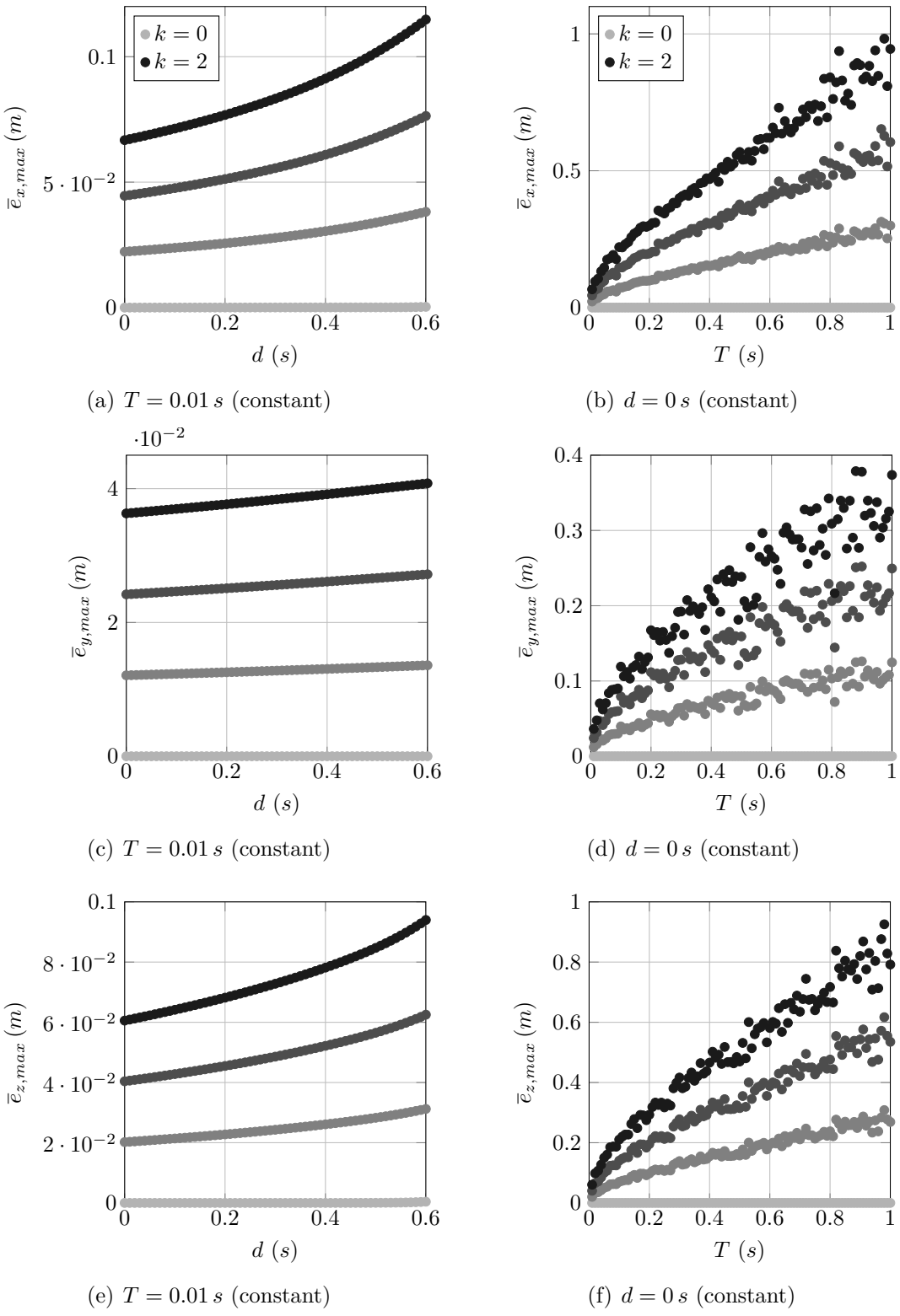

(a) $T = 0.01\,s$ (constant)

(b) $d = 0\,s$ (constant)

(c) $T = 0.01\,s$ (constant)

(d) $d = 0\,s$ (constant)

(e) $T = 0.01\,s$ (constant)

(f) $d = 0\,s$ (constant)

Figure 7.4: Component-wise variation of $\overline{e}_{r,max}$ with parameters k, d and T. Results belong to the simulations with lower-scale aircraft and wake vortex effects disabled. $k = \{0, 0.\overline{6}, 1.\overline{3}, 2\}$. The legend shows only the uppermost and lowermost values from the k-set.

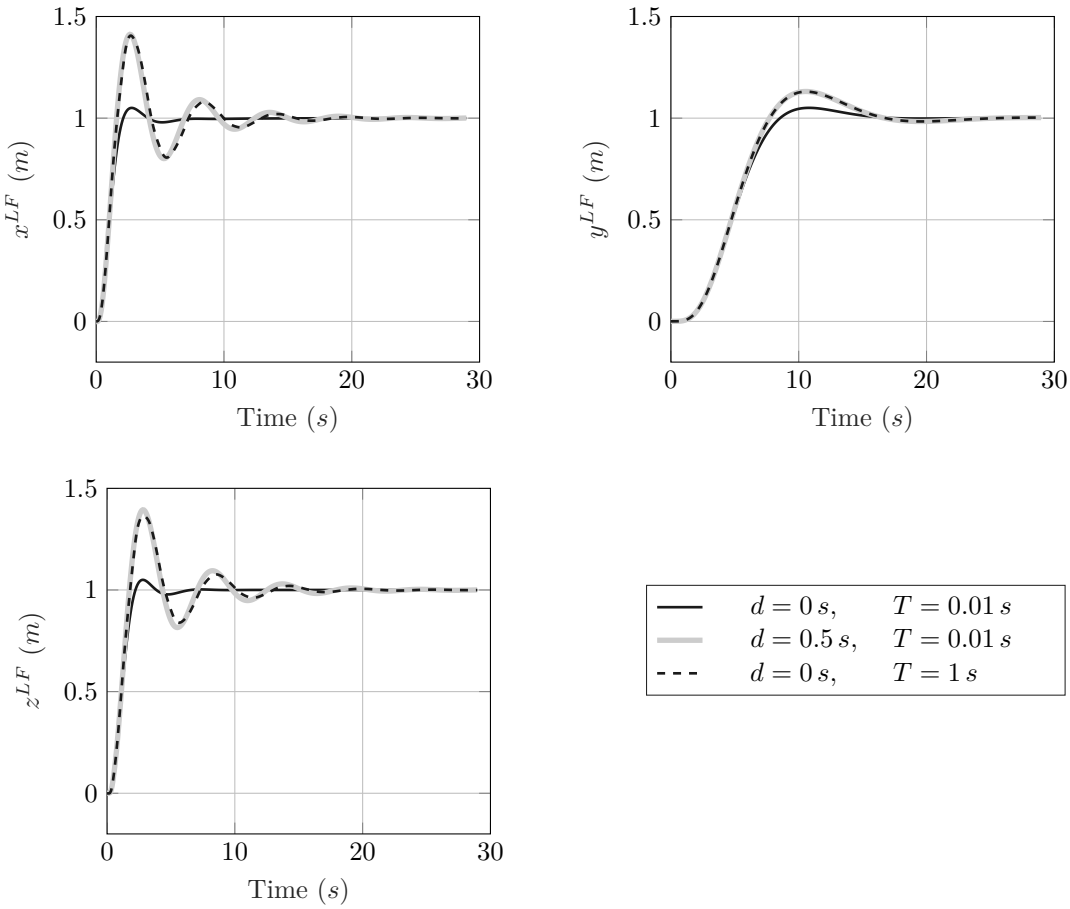

Figure 7.5: Change of closed-loop system's unit step responses with d and T. The system responses were obtained from simulations with $k = 0$, lower-scale aircraft and wake effects disabled.

parameters d and T, while keeping all other conditions unchanged. For each axis, the resulting three step responses were plotted together. The first plot is the step response of the formation controller with ideal conditions, namely, no delay in relative position information and minimum amount of sampling period. The second plot shows the response with the relative position information available at minimum sampling period but with a delay of 0.5 seconds. Finally the third plot depicts the step response of the controller, with delay-free relative position information, but at maximum amount of sampling period, i.e., $T = 1\,s$. Hence, referring to the approximation presented in Section 3.3.5, the sampling period is two times as long as the delay of the second plot.

Figure 7.5 shows that, with $k = 0$, the increase of delay and sampling period influences the closed loop dynamics in the same way. The step responses corresponding to the systems with increased delay and sampling period show less damped behavior

in comparison to the original system. Greater overshoots and undershoots as well as longer settling times are observed. Furthermore, it can be seen that, the step responses corresponding to $d = 0.5\,s$ and $T = 1\,s$ are almost identical. That is, 1-second-sampled relative position information makes approximately the same effect as 0.5-second-delayed relative position information on the closed-loop system dynamics. This complies with the sampling period approximation presented in Section 3.3.5.

7.2.2 The Effect of d on $\overline{e}_{r,max}$

The effect of delay on the x, y and z components of the maximum formation keeping error is depicted on figures 7.4(a), 7.4(c) and 7.4(e), respectively. On all three axes, it can be seen that the increase of the delay on relative position information causes a rise on the maximum position error during the formation keeping.

The effect of delay on $\overline{e}_{r,max}$ is not observed on the cases, in which the formation controller processes error-free relative position information ($k = 0$). In this case the follower aircraft is already settled at the desired formation keeping position and there is no external influence that causes the follower aircraft to deviate from the desired position. Therefore, the formation controller maintains its equilibrium state, rather than reacting to a dynamic effect. Hence, the effect of the delay on the system's behavior remains invisible. In case the relative position information contains randomly changing error, the formation controller is in a dynamic state, as it tracks the dynamic information that it receives. The effect of the delay on the formation keeping system can then be observed.

The mechanism, through which the delay on the relative position information influences the follower aircraft's formation keeping is illustrated by figure 7.6. As an example case, the figure shows excerpts from the $\overline{e}_y$ time histories of four different simulations, each of which only differs in the value of the delay parameter, d. Darker curves correspond to the greater values of d. The parameter values are given in the figure's explanation.

Figure 7.6 presents time histories, which were taken from simulations with random error in relative position information. The formation keeping system inevitably tracks the random error within the relative position information, also in case of delay-free relative position information. For the cases of delayed relative position information, the existence of the delay at the measurement channel of the control loop makes the controller use outdated information of the system state [139]. Hence the controller's actions are based on the past state of the system. As presented in Section 7.2.1, this causes increased overshoots and undershoots on the controller's reaction while it is tracking a signal. Therefore increased extrema are observed on the true relative position error time history, $\overline{e}_y(t)$. As the magnitude of delay increases, the peak magnitudes become higher. This directly translates into higher $\overline{e}_{y,max}$.

As depicted by figures 7.4(a), 7.4(c) and 7.4(e), the magnitude of the random

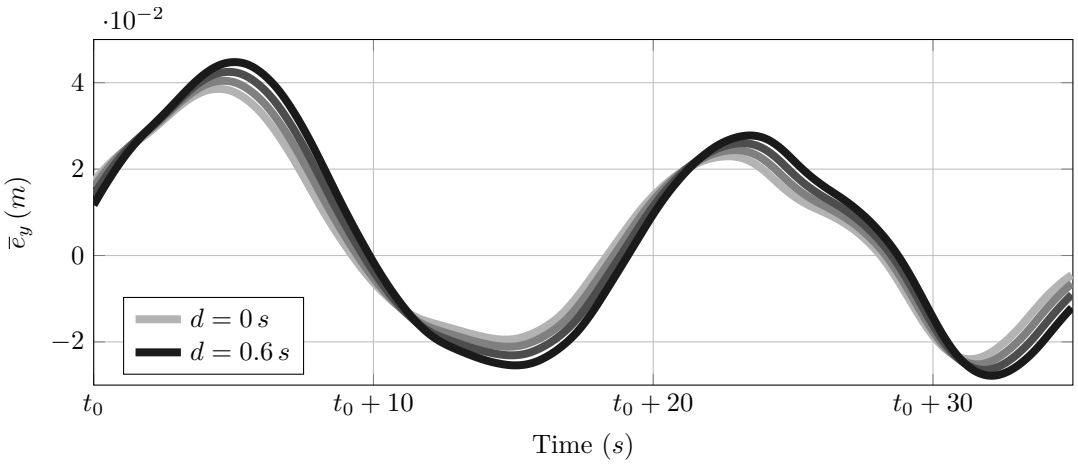

Figure 7.6: A 35-second sample time history of $\overline{e}_y$ for different values of d. The plot was generated using the same simulation data as figure 7.4. Parameter values: $k = 2, T = 0.01\,s$, $d = \{0, 0.2, 0.4, 0.6\}\,s$. The legend shows only the uppermost and lowermost values from the d-set. Corresponding time histories for x and z axes are presented by figure B.5 in Appendix B on page 167.

error carried by the relative position information is a factor on its own, which directly affects the maximum formation keeping error. For the delay-free case, comparing the magnitudes of $\overline{e}_{r,max}$ at $k = 0.\overline{6}$ and $k = 1.\overline{3}$, it can be seen that, as the magnitude of k is doubled, the value of $\overline{e}_{r,max}$ is also doubled. This relation between the magnitudes of k and $\overline{e}_{r,max}$ is observed also for nonzero delay values with minor variation.

The above-mentioned relation between k and $\overline{e}_{r,max}$ also implies that, the increase of $\overline{e}_{r,max}$ due to delay is affected by the magnitude of error carried by the relative position information. This can be seen as the increase of the slopes of $\overline{e}_{r,max}$ vs. d curves at a given d with increasing k. That is, for a given increment of delay, the more the magnitude of error in the relative position information, the more the extra increase on $\overline{e}_{r,max}$ is observed due to the delay.

Another aspect of the relations illustrated by figures 7.4(a), 7.4(c) and 7.4(e) is that, the $\overline{e}_{r,max}$ vs. d curves are different on each axis. First of all, the magnitude of $\overline{e}_{r,max}$ on y axis is considerably lower than that on x and z axes. Furthermore, the relation between $\overline{e}_{r,max}$ and d show more linear behavior on y axis than that on x and z axes. Secondly, although the curvatures of the $\overline{e}_{r,max}$ vs. d point sets are similar on x and z axes, the magnitude of $\overline{e}_{z,max}$ is lower than that of $\overline{e}_{x,max}$ at a given value of d and k.

As stated in Section 7.1, uncorrelated random errors are used for each axis in the simulations, by means of initializing the random error generators with different seeds. Additionally, as illustrated by Figure 5.2 on page 86, the speed of the closed loop dynamics are different along each axis. It is shown that, the lateral closed-loop dynamics is considerably slower than the longitudinal and vertical closed-loop

dynamics. Neglecting the coupling effects among the three axes of motion, the above-mentioned differences of $\overline{e}_{r,max}$ between the axes are attributed to these two factors, namely, the seed of the error and the speed of the closed loop dynamics.

The difference of $\overline{e}_{y,max}$ as compared to the other components is mainly the result of the slower lateral closed-loop dynamics . The details of this subject is not presented here, as the effect of the speed of the closed-loop system on $\overline{e}_{r,max}$ is covered separately in Section 7.2.4. For the x and z axes however, the speeds of the closed-loop dynamics are similar. Hence, the difference of magnitudes among $\overline{e}_{x,max}$ and $\overline{e}_{z,max}$ is attributed not mainly to the closed-loop dynamics, but to the different random error time histories processed by the formation controller along these axes. In order to test this, additional simulations were performed after swapping the seeds of the random number generators of x and z axes, but keeping all other conditions the same as those in figure 7.4. Figure 7.7 is based on the results of this set of simulations. Figures 7.7(a) and 7.7(b) present the change of $\overline{e}_{x,max}$ and $\overline{e}_{z,max}$ with respect to k and d, in the same fashion as figures 7.4(a) and 7.4(e).

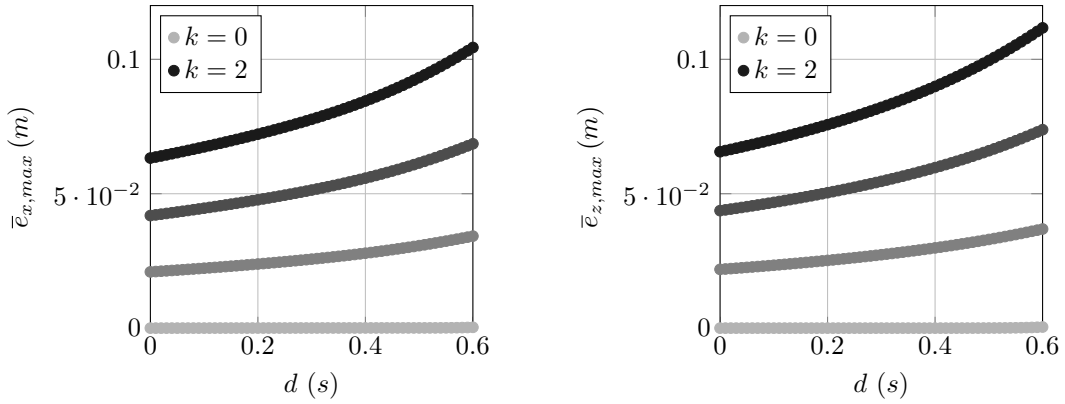

(a) $T = 0.01\,s$ (constant)

(b) $T = 0.01\,s$ (constant)

Figure 7.7: Change of $\overline{\boldsymbol{e}}_{r,max}$ with k and d with swapped random error among x and z axes. All other conditions are the same as those for figure 7.4.

In figures 7.4(a) and 7.4(e), the magnitude of $\overline{e}_{x,max}$ is higher than that of $\overline{e}_{z,max}$, at a given k and d. After swapping the random error, no exact swap of the magnitudes of $\overline{e}_{x,max}$ and $\overline{e}_{z,max}$ are observed on figures 7.7(a) and 7.7(b), with respect to figures 7.4(a) and 7.4(e). However, a decrease in the magnitude of $\overline{e}_{x,max}$, as well as an increase in the magnitude of $\overline{e}_{z,max}$ is observed. Hence, in contrast to figures 7.4(a) and 7.4(e), $\overline{e}_{z,max}$ is greater than $\overline{e}_{x,max}$ at a given d and k on figures 7.7(a) and 7.7(b). This confirms that, the actual error time history processed by the formation controller is a prominent factor affecting the change of $\overline{e}_{r,max}$ with respect to d. It is largely responsible for the difference of the magnitudes of $\overline{e}_{r,max}$ on figures 7.4(a) and 7.4(e). On the other hand, despite the change of the magnitude of $\overline{e}_{r,max}$ due to different error time histories, the trends of $\overline{e}_{r,max}$ vs. d curves remain unchanged.

7.2.3 The Effect of T on $\overline{\boldsymbol{e}}_{r,max}$

Figures 7.4(b), 7.4(d) and 7.4(f) depict the effects of the relative position information sampling period T and error magnitude k on the components of $\overline{\boldsymbol{e}}_{r,max}$. On all three axes, increasing the sampling period increases the maximum true position error during the formation keeping. An immediate difference of the effect of T on $\overline{\boldsymbol{e}}_{r,max}$ with respect to the effect of d is the greater rate of change of $\overline{\boldsymbol{e}}_{r,max}$ with T. Hence, the formation keeping accuracy is more sensitive to the relative position information's sampling period than its delay, under the condition that the considered system remains stable over the ranges of d and T.

Similar to the cases with varying delay, the effect of sampling period on $\overline{\boldsymbol{e}}_{r,max}$ becomes only visible in case of nonzero error on the relative position information. The explanations given for the delay in this regard hold also for the sampling period. In summary, the effect of T on $\overline{\boldsymbol{e}}_{r,max}$ becomes visible, if the formation controller is in a dynamic state. In the case considered, the presence of the random error within the relative position information is the factor, which causes the controller to dynamically react, as the controller tracks the error.

In order to visualize the means, through which the sampling period influences the formation keeping accuracy, figure 7.8 is presented. Figure 7.8 depicts example time histories of $\overline{e}_y$, corresponding to four different simulations. Each time history corresponds to one simulation with different T, with all other conditions fixed. The time histories were plotted with different tones of gray, with the darker curves corresponding to higher values of T.

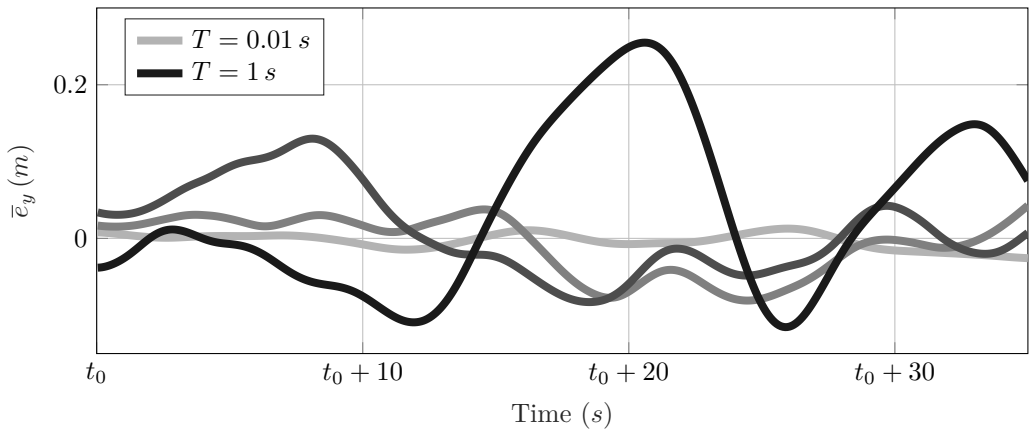

Figure 7.8: A 35-second sample time history of $\overline{e}_y$ for different values of T. The plot was generated using the same simulation data as figure 7.4. Parameter values: $k = 2$, $d = 0\,s$, $T = \{0.01, 0.33, 0.66, 1\}\,s$. The legend shows only the uppermost and lowermost values from the T-set. The term t_0 is not to be associated with that in figure 7.6. Corresponding time histories for x and z axes are presented by figure B.6 in Appendix B on page 168.

One major difference of figure 7.8 with respect to figure 7.6 is the correlation of the different time series with each other within each figure. On figure 7.6, the

curves corresponding to different values of d show very similar development through time. Apart from the different peak values and shifts along the time axis, the rises and falls of the curves predominantly coincide with each other. On figure 7.8 however, the similarity between different time histories is minor. This difference between figures 7.6 and 7.8 is due to the difference of random error time histories processed by the formation controller, as explained below.

Section 7.2.1 states that, the presence of delay or increased amount of sampling period affect the closed-loop dynamics in the same fashion. Furthermore, the parameter values $d = 0.5\,s$ and $T = 1\,s$ make approximately the same effect on closed-loop dynamics. However, the formation controller also tracks the random error coming along with the relative position information. Therefore, besides the closed-loop dynamics, any change on the random error time history will also affect the accuracy of the formation keeping. Hence, the effects of d and T on the properties of the random error time history also need to be considered. With the presence of delay in relative position information, the relative position information processed by the controller becomes outdated by d with respect to the delay-free case. Hence, except the time shift, the random error contained within the relative position information remains essentially the same. However, if the sampling period of the relative position information changes, this also changes the random error time history processed by the formation controller. That is, a sample period of T seconds will cause the formation controller to experience a random error signal sampled by T seconds. Furthermore, the instantaneous magnitude of the random error at each sample will be different for different values of T. This is principally responsible for the dissimilarities of the time histories shown in figure 7.8 with respect to each other.

The scattering of data points on Figures 7.4(b), 7.4(d) and 7.4(f) is also attributed to the relation between T and the resulting random error time history, explained above. As a new error time series is formed with changing T, depending on the resulting error time series, $\overline{\boldsymbol{e}}_{r,max}$ may increase with small increments of T more or less than the trend of $\overline{\boldsymbol{e}}_{r,max}$ averaged over a wider range of T.

An alternative explanation on the means of influence of the parameter T can be given, by considering the relative position information as a whole with its error component. That is, the parameter T is seen merely as the sampling period of the formation controller's feedback signal, which is made up of two portions: true position information and randomly-varying error. Due to the proportion of the error in relative position information, the formation controller partially misguides the follower aircraft. Considering an arbitrary axis of motion, this partial misguidance occurs toward the positive or negative direction of the axis. The misguidance continues along the same direction until the formation controller receives the next update of relative position information after T seconds. Hence, the longer the sampling period of the relative position information is, the longer time the misguidance occurs toward the same direction. The longer the follower aircraft is misguided toward the same direction,

the longer time the true relative position error will rise along that direction. For the cases, in which T is small, until the next update of the relative position information, the position error due to misguidance has a short time to rise. As the next set of relative position information is received, due to the random character of the error in relative position information, the misguidance is likely to change its direction. Hence, the true relative position error does not rise for a long time through one direction.

In parallel with the effect of the delay on the components of $\overline{\boldsymbol{e}}_{r,max}$, the same amount of increase on T causes less increase on $\overline{\boldsymbol{e}}_{y,max}$ than on $\overline{\boldsymbol{e}}_{x,max}$ and $\overline{\boldsymbol{e}}_{z,max}$. This is attributed to the slower dynamics along the lateral axis and investigated separately in Section 7.2.4. Additionally, at $k \neq 0$, the relation of $\overline{\boldsymbol{e}}_{y,max}$ and T shows more scattered, i.e. less precise behavior in comparison to its counterparts on x and z axes. This behavior is also attributed to the speed of closed-loop dynamics along each axis. Since the closed-loop dynamics is slower on the y axis, it requires longer duration of simulation, in order to obtain $\overline{\boldsymbol{e}}_{y,max}$ with the level of precision observed on $\overline{\boldsymbol{e}}_{x,max}$ and $\overline{\boldsymbol{e}}_{z,max}$ graphs.

7.2.4 The Effects of Aircraft Scale on $\overline{e}_{r,max}$

The effects of the parameters k, d and T on $\overline{e}_{r,max}$ are discussed in the previous sections. This section discusses how the effects of k, d and T on $\overline{e}_{r,max}$ is influenced by the scale of the aircraft, that are taking part in the automated formation keeping.

As stated previously, lower-scale and higher-scale aircraft pairs are used for two separate formation flight simulation sets. The ratio of the characteristic lengths of the higher-scale and lower-scale aircraft is 6.25. The aircraft are of the same geometry. Their flight conditions, as well as inertial, actuator, propulsion and flight condition properties are determined by the dynamical scaling relations. The flight control systems of both scales of aircraft are tuned so that the formation controllers exhibit comparable step responses, as displayed by figure 5.2 on page 86. The lower-scale follower aircraft's formation controller reacts 2.5 times faster than that of the higher-scale follower aircraft.

Figure 7.9 presents the change of $\overline{e}_{y,max}$ with k, d and T on lower-scale and higher-scale aircraft comparatively. In order to better visualize the influence of the aircraft scale, the results obtained from the lower-scale and higher-scale aircraft simulations are presented alongside each other. Although the higher-scale aircraft simulations use a greater upper limit of 1 s for the parameter d, in order to ease the comparability, for both scales of aircraft the corresponding figure was plotted up to $d = 0.6\,s$. Apart from this, the figure displays results based on simulations, which use the same parameter values for both scales of aircraft. For brevity, the figure only depicts the lateral component of the maximum position error. Figure B.7 on page 169 gives the change of all three components of $\overline{\boldsymbol{e}}_{r,max}$ with full range of the parameter d for the higher-scale aircraft.

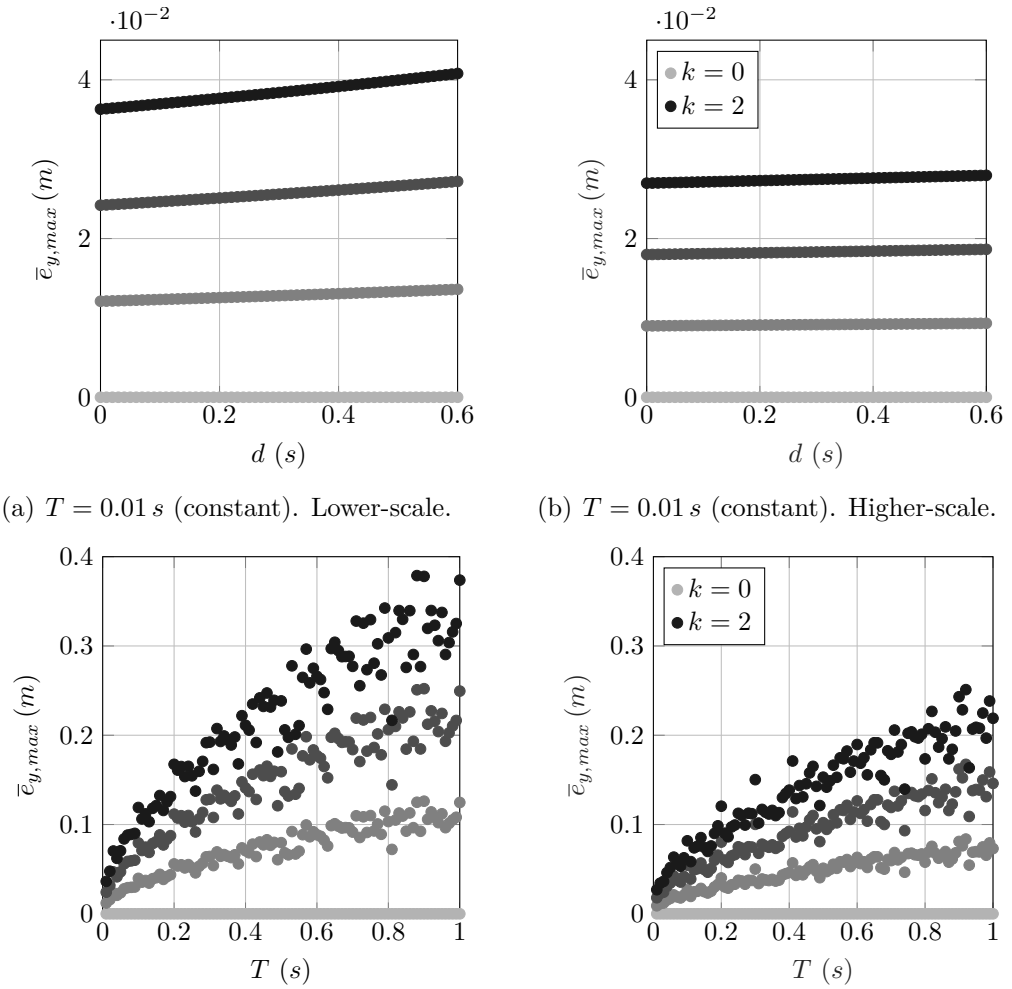

(a) $T = 0.01\,s$ (constant). Lower-scale.

(b) $T = 0.01\,s$ (constant). Higher-scale.

(c) $d = 0\,s$ (constant). Lower-scale.

(d) $d = 0\,s$ (constant). Higher-scale.

Figure 7.9: Variation of $\overline{e}_{y,max}$ with parameters k, d and T for lower-scale and higher scale aircraft. Results belong to the simulations with disabled wake vortex effects. $k = \{0, 0.\bar{6}, 1.\bar{3}, 2\}$. The legend shows only the uppermost and lowermost values from the k-set.

In order to support the forthcoming discussions on figure 7.9, about how the system scale affect the maximum position keeping error during formation keeping, a brief discussion is given below, on how the closed-loop system responses are affected by the parameters d and T on higher-scale and lower-scale aircraft comparatively. For this purpose, figure 7.10 is given, which displays the step responses of lower-scale and higher-scale aircraft on the lateral channel as the parameters d and T are changed. Corresponding figures for the longitudinal and vertical control channels are given by figure B.8 on page 170. As shown on figure 7.10, for the nominal case with $d = 0\,s$ and $T = 0.01\,s$, the step responses of both the lower-scale and higher-scale aircraft exhibit a maximum overshoot of about 5 %. As discussed before, for both scales of aircraft, the overshoots of the step responses increase for $d = 0.5\,s$ and $T = 1\,s$ by

the same amount. However, the amount of increase in overshoot varies between the different scales of aircraft. For the lower-scale aircraft, with the increased amounts of d and T the maximum overshoot reaches up to 13 %. For the higher-scale aircraft, however, this reaches up to about 8 %. The same behavior is observed also on x and z axes. On both axes with $d = 0.5\,s$ and $T = 1\,s$, the maximum overshoot increases up to 40 % for the lower-scale aircraft and up to 17 % for the higher-scale aircraft. This shows that, the higher-scale aircraft is affected by the increase of parameters d and T less than the lower-scale aircraft.

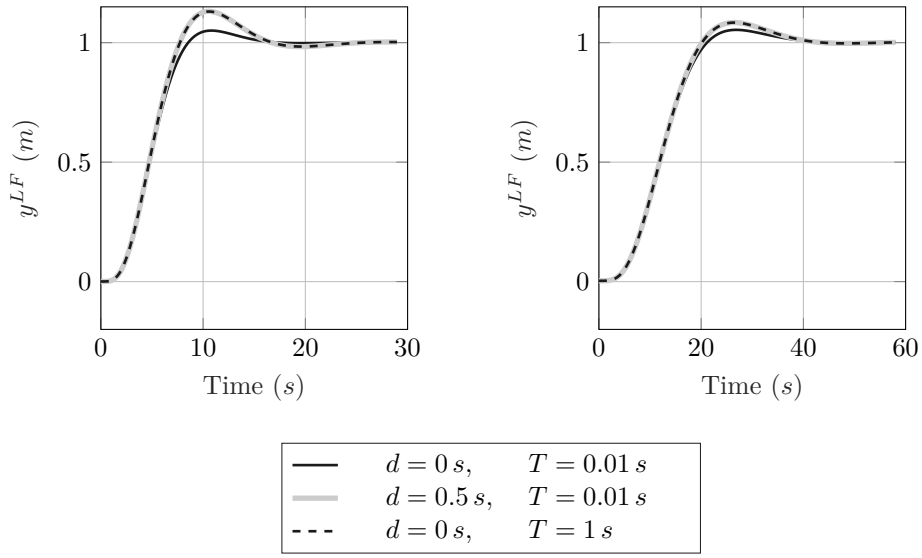

Figure 7.10: Comparison of the lower-scale and higher-scale closed-loop systems' unit step responses on y-axis, as they vary with the parameters d and T. Left column: lower-scale aircraft, right column: higher-scale aircraft.

Returning back to figure 7.9, as the higher-scale aircraft's closed-loop dynamics is affected by the parameters d and T less than that of the lower-scale aircraft, the increase on $\overline{e}_{y,max}$ due to the increase of d and T is smaller on the higher-scale aircraft. With the variation of the parameter T however, an additional effect is introduced to the system, as discussed earlier. That is, for $k \neq 0$, the parameter T not only affects the closed-loop dynamics, but also changes the random error time history tracked by the formation controller. Considering the formation control of both scales of aircraft, which track the randomly-changing error coming along with the relative position information, the slower closed-loop dynamics of the higher-scale aircraft filters lower frequency variations on its input with respect to the lower-scale aircraft. Hence the higher-scale aircraft reacts less to the random error, causing lower buildup of $\overline{e}_{y,max}$ than the lower-scale aircraft.

The discussions given above on the example of y-axis, also hold for x and z axes. In summary, the slower closed-loop dynamics of the higher-scale aircraft is less sensitive against the variations in parameters k, d and T. Hence, with the same amount of

increase in these parameters, lower amount of increase on the components of $\overline{e}_{r,max}$ is observed on the higher-scale aircraft in comparison to the lower-scale aircraft.

7.2.5 The Effects of Wake Vortices on $\overline{e}_{r,max}$

The last aspect covered by the simulation-based analysis is the influence of the parameters k, d and T on $\overline{e}_{r,max}$, under the effect of the wake vortices generated by the leader aircraft. In order to investigate this, the formation flight simulations were carried out enabling the wake vortex model detailed in Chapter 6, with the parameter values given in table 7.1. In order to obtain control data, the simulations were executed also with disabled wake vortex model, keeping the parameter values and all other conditions unchanged. The effects of wake vortices on $\overline{e}_{r,max}$ are then explained based on the comparison of the two sets of simulation.

In the formation flight simulations, the follower aircraft is commanded to keep its position at a location two wingspans behind, quarter wingspans below the leader with no lateral offset. This relative positioning represents the typical separation between the two aircraft during a probe and drogue aerial refueling mission [138]. As depicted by figure 6.3 on page 93, due to the wingtip vortices, the flow field behind the leader aircraft is highly nonuniform. Hence the overall aerodynamic influence of the wake vortices on the follower aircraft is strongly dependent on the relative position between the aircraft. The geometry, size and weight of the two aircraft are the other factors determining the effects of the wake vortices on the follower aircraft. Therefore, it is worth emphasizing that, all results presented in this section, which involve the wake effects, are specific to the particular leader-to-follower relative positioning mentioned above, as well as to the geometry, size and weight relations of the two aircraft.

Figure 7.11 presents the comparison of $\overline{e}_{y,max}$ with and without wake vortex effects, as it changes with the parameters k, d and T. Since the most prominent influence of the wake effects on the follower aircraft is the roll disturbance[3], for brevity only the lateral error component is shown. Corresponding figures for x and z axes are given by figures B.9 and B.10 on pages 171 and 172, respectively.

Comparing the change of $\overline{e}_{y,max}$ with and without wake vortex effects on figure 7.11, it can be seen that, the increase of $\overline{e}_{y,max}$ is lower for all values of d, T and $k \neq 0$ under the effect of the wake vortices as compared to the case without the wake vortex effects. This is due to the stabilizing nature of the wake-induced roll disturbance acting on the follower aircraft at around its formation keeping position, as explained below.

Figure 7.12 shows position-dependent effective sidewash $\overline{v}_w$ and the wake-induced roll disturbance $\overline{p}_w$ acting on the follower aircraft around the region it is located during the formation keeping. As the follower aircraft's relative position varies about

[3]Figure 6.4 on page 99 depicts the components of the effective wake-induced disturbance on the follower aircraft.

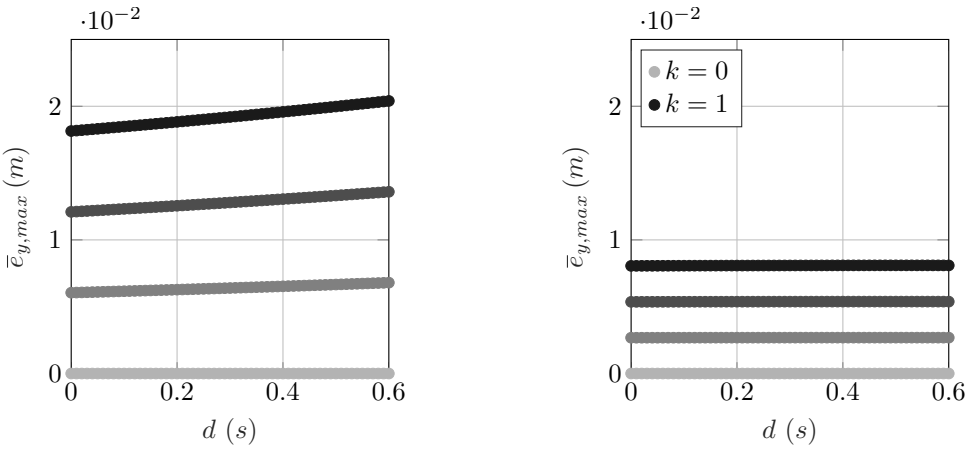

(a) $T = 0.01\,s$ (constant). Wake disabled.

(b) $T = 0.01\,s$ (constant). Wake enabled.

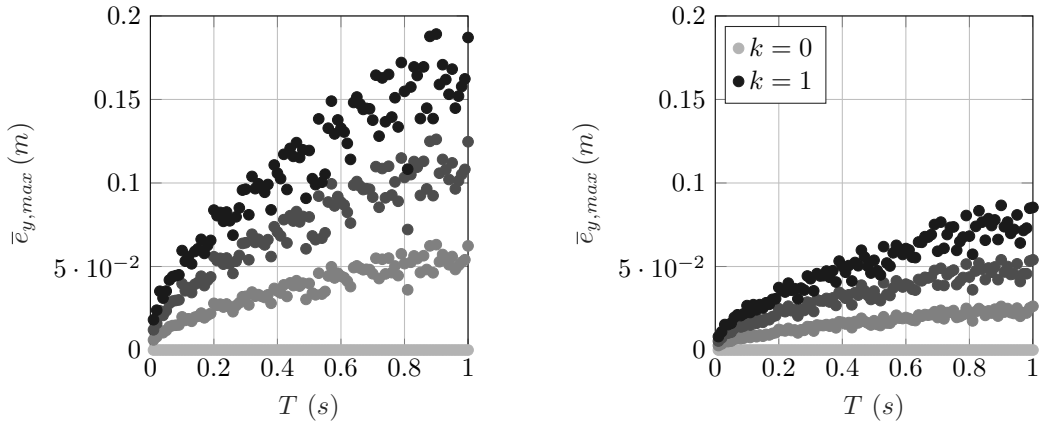

(c) $d = 0\,s$ (constant). Wake disabled.

(d) $d = 0\,s$ (constant). Wake enabled.

Figure 7.11: Variation of $\overline{e}_{y,max}$ with parameters k, d and T on lower-scale aircraft, without and with wake vortex effects. $k = \{0, 0.\bar{3}, 0.\bar{6}, 1\}$. The legend shows only the uppermost and lowermost values from the k-set.

its commanded relative position during the formation flight, the figure shows the disturbance values at different vertical and lateral separations between the aircraft. Since the wake disturbances do not show notable variations along the longitudinal axis around the relative position of concern, the figures are plotted for the constant, commanded longitudinal relative position, $x^{LF} = -2b_L$.

As shown in figure 7.12, within the considered range of lateral positions, for the positive lateral separations, positive sidewash acts to the follower aircraft. That is, if the follower is located at the right side of the centerline of the leader aircraft, $y^{LF} > 0$, positive sidewash acts to the follower aircraft, which pushes the follower aircraft further to the right. Hence the relation of follower's lateral relative position and the vortex-induced sidewash disturbance is destabilizing. The same destabilizing behavior is observed also for the lateral positions at the left side of the leader aircraft

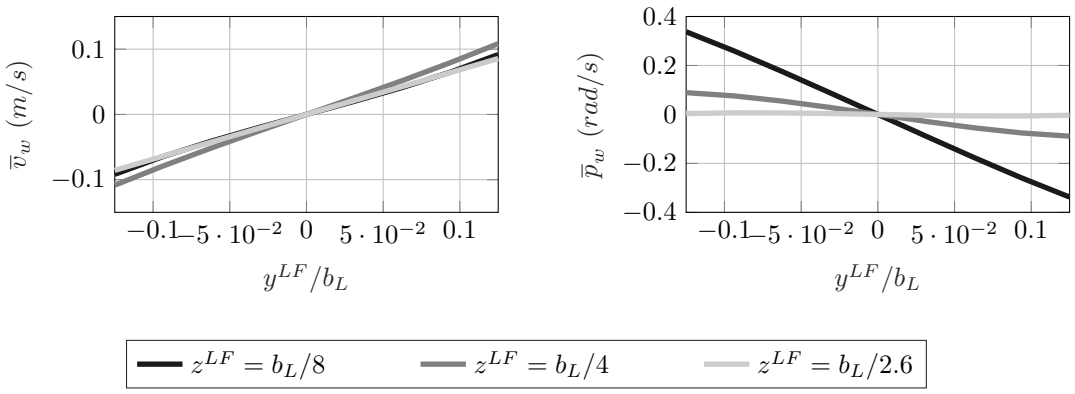

Figure 7.12: Effective lateral wake-induced disturbance acting on the follower. Aircraft longitudinal separation: $x^{LF} = -2b_L$. Lower-scale aircraft pair.

centerline. For the roll disturbance induced by the leader's wake, however, the effect is opposite. As shown, for the vertical separations less than $b_L/2.6$, at the right side of the leader aircraft's centerline, negative rolling disturbance acts to the follower aircraft, which tends to move the aircraft to the left. Similarly, if the follower aircraft is located at the left side of the leader aircraft's centerline, the aircraft experiences positive roll disturbance to the right. Hence within the relative positioning ranges considered, the wake-induced roll disturbance is of stabilizing character. Looking at the magnitudes of the sidewash and the roll disturbance, it can be seen that the dominant wake-induced lateral disturbance is the roll disturbance. Therefore the resultant aerodynamic effect, that the follower aircraft experiences during the formation keeping, is laterally stabilizing about the centerline of the leader aircraft, $y^{LF} = 0$.

During the formation keeping, the follower aircraft is commanded to fly laterally aligned with the leader aircraft's centerline. The increased values of the parameters k, d and T cause the follower aircraft to momentarily divert from the desired lateral position. However, since the resultant lateral wake disturbance tends to bring the follower aircraft back to the leader aircraft centerline, $\overline{e}_{y,max}$ is considerably reduced in comparison to the case without the effects of the leader's wake vortices.

A similar stabilizing effect of lesser magnitude is observed also at the downwash disturbance that the follower aircraft experiences. Figure B.11 on page 172 depicts that, the follower aircraft experiences stronger downwash, as it moves upwards, i.e., vertically closer to the leader aircraft. As the follower aircraft moves downwards from the commanded relative position, the magnitude of the downwash decreases. As a result of this stabilizing disturbance, as shown by figure B.10 on page 172, the magnitude of $\overline{e}_{z,max}$ is slightly reduced under the effects of the wake vortices, as compared to the case without the wake vortex effects.

At the follower aircraft's relative position no significant longitudinal disturbance

is observed. Hence the behavior of $\overline{e}_{x,max}$ with the wake vortex disturbance show no significant change with respect to the case without the wake vortex effects, as shown by figure B.9 on page 171.

Chapter 8

System-Theoretical Approximation of the Simulation Results

Using the system-theoretical foundations presented in Chapter 3, this chapter proposes models, which approximate the simulation results presented in Chapter 7. In this context, the chapter begins with the representation of the closed-loop formation flight dynamics in terms of first-order transfer functions. Subsequently, using the first-order approximations of the dynamical system, the effects of the independent variables on the formation flight's true maximum error are approximated using formulations based on H_2 norm and frequency response.

8.1 Approximations Based on System Theory

8.1.1 Formation-Keeping System as First-Order Dynamics

Neglecting the wake vortex effects, the formation flight dynamical system is considered in form of the functional block diagram given by figure 8.1. For the system shown in figure 8.1, it is assumed that the only disturbance acting on the formation keeping system is that coming from the deficiencies of the relative position information. This is due to the steady, straight and level flight pattern of the leader, as well as the turbulence-free atmospheric condition considered in this work.

Vector signals are used in the diagram for brevity. It is assumed that, the block diagram can be drawn in the same form for each component of the position vectors together with the closed-loop leader and follower dynamics along the corresponding axis of motion. The signal $\boldsymbol{r}_d^{LF}$ is the constant, desired relative position which is commanded to the follower aircraft's formation-hold controller. The signal $\boldsymbol{r}^{LF}$ is the true relative position of the follower aircraft with respect to the leader aircraft.

It is assumed that, during formation keeping the follower aircraft's deviations from the steady, straight and level flight condition are small. Hence the coupling effects

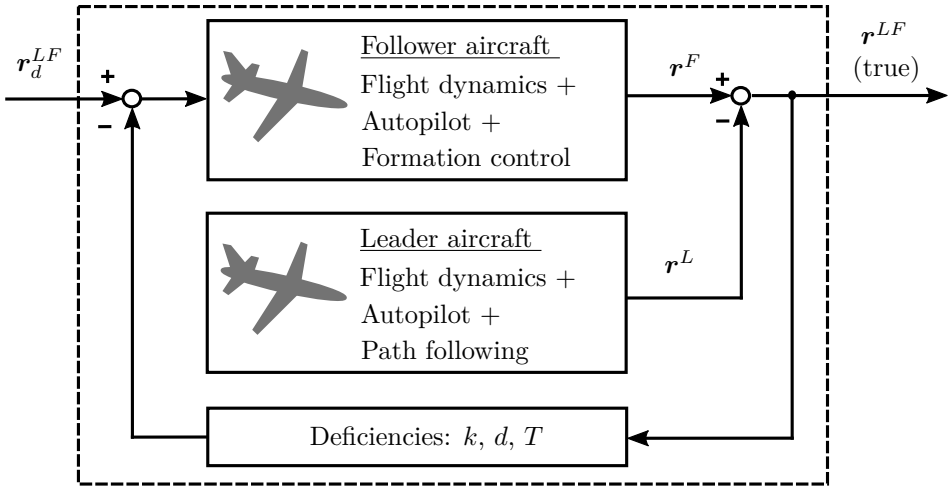

Figure 8.1: Formation flight dynamics as functional block diagram.

among longitudinal, lateral and vertical motion of the follower aircraft are neglected. Based on figure 8.1, the closed-loop formation flight dynamics is defined component-wise as three single-input, single-output dynamical systems with the input r_d^{LF} and the output r^{LF}. Here the scalar term r represents any of the x, y or z component of the position vectors $\boldsymbol{r}_d^{LF}$ and $\boldsymbol{r}^{LF}$. The dynamical behavior of this closed-loop system has already been defined for each axis in form of step responses for the case of perfect relative position information, i.e. $k = 0$, $d = 0$ and $T = 0.01\,s$. The step responses are shown on figure 5.2 on page 86. In order to obtain a mathematical representation of the closed-loop dynamics, second-order transfer functions are fitted to the closed-loop step responses. Figure 8.2 shows the same step response curves as those given by figure 5.2, along with the step responses of the fitted second-order transfer functions. The fitted transfer functions are of the form given in eq. (3.20) on page 59, which are characterized by the damping ratio ζ and the natural frequency ω_0. The damping ratio and natural frequency of the fitted transfer functions are listed on table 8.1. For each axis, the approximated transfer functions are denoted by the terms x/x_d, y/y_d and z/z_d, omitting the superscript LF for simplicity.

Table 8.1 shows that, on each axis, the second-order transfer functions for both lower-scale and higher-scale aircraft have the same damping ratio. According to the natural frequencies of the second-order system approximations, the lower-scale aircraft dynamics is 2.5 times faster than higher-scale aircraft dynamics on all three axes of motion. For each scale of aircraft, the slowest dynamics is on the lateral channel. The longitudinal dynamics is the fastest, but the vertical dynamics is slower than the longitudinal dynamics only by 2 %. The longitudinal dynamics is faster than the lateral dynamics by a factor of 3.75.

The second-order transfer functions, which are used to approximate the closed-loop formation keeping dynamics, were further simplified by converting them to first-

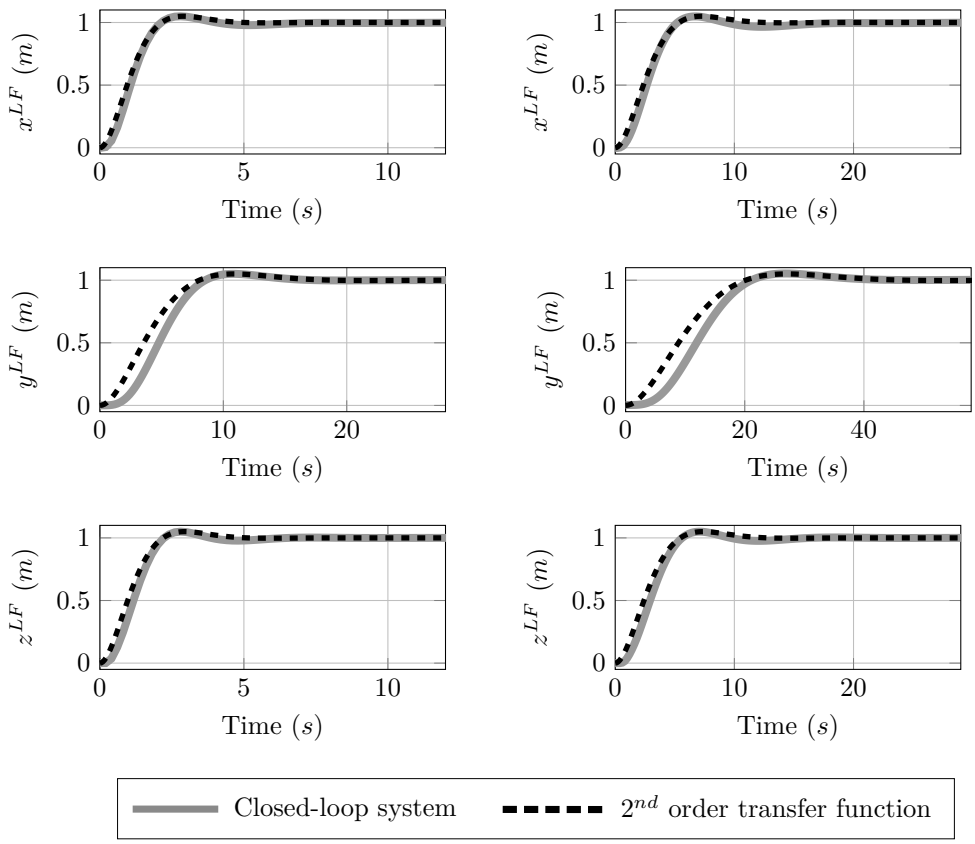

Figure 8.2: Closed-loop system and fitted second-order transfer function responses to a unit step command starting at $t = 0$ s. Left and right-hand-side figures correspond to the lower-scale and higher-scale aircraft respectively.

	Lower scale			**Higher scale**		
	ω_0	ζ	τ	ω_0	ζ	τ
x/x_d	1.5	0.69	0.966	0.6	0.69	2.415
y/y_d	0.4	0.69	3.623	0.16	0.69	9.058
z/z_d	1.47	0.69	0.986	0.588	0.69	2.465

Table 8.1: Parameters of the second-order and first-order transfer functions for component-wise approximation of the closed-loop formation keeping system with $k = 0$, $d = 0$ and $T = 0.01\,s$.

order transfer functions. This was done using the relation $\tau = 1/(\zeta\omega_0)$ (eq. (3.21)), presented on page 60. Although this simplification causes a loss of fidelity in the approximation of the system's dynamics, it enables the representation of the system characteristics by a single parameter, the time constant τ. The time constants of the first-order transfer functions are given in table 8.1. The scale-wise and component-

wise speed comparison of the second-order transfer functions given above also applies to the first-order transfer functions.

8.1.2 True Relative Position Error Dynamics as Transfer Function Block Diagram

The simulation-based analysis uses the maximum true relative position error, $\overline{\boldsymbol{e}}_{r,max}$, in order to represent the performance of the formation keeping. Here, it is aimed to obtain a mathematical expression for describing the change of formation keeping performance with respect to the deficiencies of the relative position information. Therefore it is desired to obtain a system, which represents the dynamics of the relative position error in terms of the deficiencies of the relative position information. This system is derived in this section from the system shown in figure 8.1, and presented in terms of a transfer function block diagram.

First of all, the functional block diagram shown in figure 8.1 is represented in terms of a block diagram of transfer functions. This is shown in figure 8.3, which is drawn for scalar signals and transfer functions. The terms r_d and r represent any component of $\boldsymbol{r}_d^{LF}$ and $\boldsymbol{r}^{LF}$ respectively. That is, r_d is the desired relative position commanded to the system along x, y or z axes, and the term r is the true relative position along the corresponding axis. The superscript LF is omitted for simplicity. The term $P(s)$ is a scalar transfer function representing the leader-follower relative position dynamics along the corresponding axis. The terms $T(s)$ and $d(s)$ are transfer functions representing the sampling period T and the delay d, respectively. The sign (s) is used in order to distinguish the transfer functions from the corresponding parameter, T or d. The term n represents the random, zero-mean relative position error added to the respective true relative position component assuming $k = 1$.

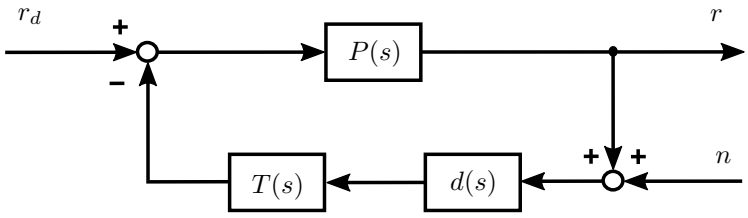

Figure 8.3: Formation flight dynamics as a block diagram of transfer functions.

In the previous section, first-order transfer functions were defined, which represent the closed-loop system shown in figure 8.1 with the *nominal parameter values*, $k = 0$, $d = 0s$ and $T = 0.01s$. The nominal parameter values are the lower limits for the parameter values, and they correspond to the perfect relative position information for the simulation set-up considered in this work. That is, error-free and delay-free relative position information, whose most recent update is available to the formation flight controller at each cycle of its execution. The case of perfect relative position

information is approximated on the transfer function block diagram, figure 8.3, by letting $T(s) = 1$, $d(s) = 1$ and $n = 0$. For each axis, the resulting closed loop transfer function r/r_d correspond to the ones, which are already defined in the previous section. Taking the first-order transfer functions, which are of the form $1/(\tau s + 1)$, this yields $P(s) = 1/\tau s$, for which the term τ is defined per axis on table 8.1.

Having the transfer function $P(s)$ defined, it is desired to rearrange the block diagram shown in figure 8.3, so that its output is the relative position error. In order to facilitate this, a new error signal, n_1 is defined such that, $n_1 = n\, d(s)\, T(s)$. With the new error signal n_1, the block diagram given in figure 8.3 can be redrawn as shown in figure 8.4. The term n_1 is the random error signal n, but sampled with T and delayed by d. It is assumed that, over a sufficiently long duration of simulation, the statistical properties of the signals n and n_1 are the same. The term *statistical properties* here refers to the mean, the standard deviation and the probability distribution of the signal.

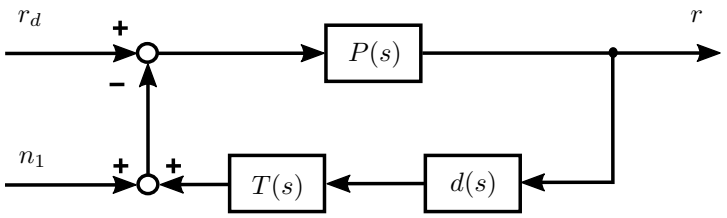

Figure 8.4: Formation flight dynamics as transfer function block diagram, with new error signal n_1.

Figure 8.4 needs to be further rearranged in order to obtain the component-wise true relative position error, $\overline{e}_r$ as the system's output. In order to achieve this, the desired relative position r_d is set to zero. Since the wake vortex effects are assumed to be zero, the dynamical properties of the system do not depend on the relative position at which the follower aircraft maintains its position. Recalling that the true relative position error $\overline{e}_r$ is defined as $\overline{e}_r = r - r_d$, with $r_d = 0$, the true relative position r will be equal to $\overline{e}_r$. Applying $r_d = 0$ and $\overline{e}_r = r$ to figure 8.4, figure 8.5 is obtained.

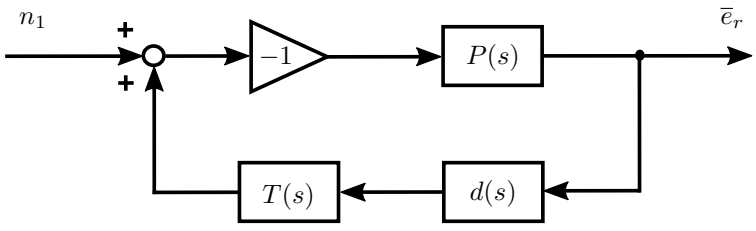

Figure 8.5: Relative position error dynamics as transfer function block diagram, with input n_1, $r_d = 0$ and $\overline{e}_r = r$.

On figure 8.5, the true relative position error $\overline{e}_r$ is the output of a closed-loop system, whose dynamics depend on the leader-follower relative position dynamics, $P(s)$,

the error in the relative position information, n_1, the transfer function representing the amount of the delay in the relative position, $d(s)$, and the sampling period transfer function $T(s)$. That is, $\overline{e}_r$ is already expressed in terms of all desired entities. However, figure 8.5 is rearranged one last time, in order to convert it to the standard negative feedback form, so that it is equivalent to the negative feedback systems given by figure 3.2, on page 61. In order to perform this rearrangement, another error signal, n_2 is defined such that, $n_2 = -n_1$. It is assumed that, the new signal n_2 has the same statistical properties as the signal n_1 over a sufficiently long time span, since the signal n_1 is zero mean. Using the new error signal n_2 and rearranging figure 8.5, the closed-loop system with output $\overline{e}_r$ is obtained in negative feedback form, which is shown in figure 8.6.

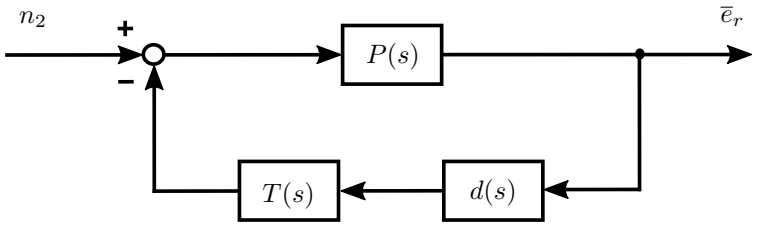

Figure 8.6: Relative position error dynamics as transfer function block diagram, with input n_2, $r_d = 0$ and $\overline{e}_r = r$.

Figure 8.6 is the final system representing the dynamics of the true relative position error in terms of desired system attributes, n_2, $d(s)$ and $T(s)$. Based on this system, the effects of the system attributes on $\overline{e}_{r,max}$ are approximated mathematically in the following sections.

8.1.3 Approximated $\overline{e}_{r,max}$ in Terms of d, k and P

In this section, a function is derived, which approximately relates the maximum relative position error $\overline{e}_{r,max}$, to the delay of the relative position information d, the magnitude of the error in the relative position information represented by k, and the open-loop system dynamics $P(s)$. The sampling period parameter T is kept fixed at its minimum value, namely $T = 0.01s$. This is represented on the system shown by figure 8.6 by $T(s) = 1$. In this case, the only transfer function located on the feedback path is the delay transfer function $d(s)$, which is represented by e^{-sd} for a delay of d seconds, with the term e being the base of the natural logarithm. The resulting time-delayed dynamic system is exactly of the form given by figure 3.2, on page 61. The closed-loop system with input n_2 and output $\overline{e}_r$ is represented by $G_r(s)$, with the subscript r standing for any position component, x, y or z.

As stated in Chapter 3, H_2 norm is a measure for quantifying the magnitudes of the dynamical system outputs. Considering the time-delayed system of interest, the H_2 norm of the closed-loop system $G_r(s)$ provides a measure of the magnitude of $\overline{e}_r$

under the input n_2. The H_2 norm of the time-delayed closed-loop system is already defined by eq. (3.39) on page 64. Rewriting eq. (3.39) by substituting d in place of the delay term, eq. (8.1) is obtained. If the system $G_r(s)$ had no internal delays, its H_2 norm would be the expression given by eq. (8.2).

$$||G_r(s)||_2 = \frac{1}{\sqrt{2\tau}}\sqrt{\frac{\cos(d/\tau)}{1-\sin(d/\tau)}} \tag{8.1}$$

$$||G_r(s)||_2\Big|_{d=0} = \frac{1}{\sqrt{2\tau}} \tag{8.2}$$

Equations (8.1) and (8.2) provide measures for the magnitude of the system output $\overline{e}_r$ for time-delayed and delay-free cases respectively. For the representation of the formation flight performance, the maximum relative position error over a given time span of formation keeping, i.e. $\overline{e}_{r,max}$ is used. The term $\overline{e}_{r,max}$ is assumed to be directly proportional to the H_2 norm of the system $G_r(s)$. Hence, as a measure of $\overline{e}_{r,max}$ in a delay-free system, eq. (8.3) is proposed, in which the term c_1 is a positive real constant.

$$\overline{e}_{r,max}\Big|_{d=0} = c_1\frac{1}{\sqrt{2\tau}} \tag{8.3}$$

The effect of delay on $\overline{e}_{r,max}$ is approximated as a separate, additive term using eqs. (8.1) and (8.2). The change of the H_2 norm due to the presence of nonzero delay is defined with respect to the delay-free case as the difference between eqs. (8.1) and (8.2), yielding eq. (8.4). This change on H_2 norm due to the delay is assumed to correspond to the change on $\overline{e}_{r,max}$ due to the delay, $\Delta\overline{e}_{r,max}(d)$, with respect to the delay-free case. This relation is defined with another direct proportion of a real, positive proportionality constant c_2, as shown in eq. (8.5).

$$||G_r(s)||_2 - ||G_r(s)||_2\Big|_{d=0} = \frac{1}{\sqrt{2\tau}}\sqrt{\frac{\cos(d/\tau)}{1-\sin(d/\tau)}} - \frac{1}{\sqrt{2\tau}} \tag{8.4}$$

$$\Delta\overline{e}_{r,max}(d) = c_2\frac{1}{\sqrt{2\tau}}\left(\sqrt{\frac{\cos(d/\tau)}{1-\sin(d/\tau)}} - 1\right) \tag{8.5}$$

Addition of eq. (8.5) and eq. (8.3) yields a combined expression for $\overline{e}_{r,max}$, as given by eq. (8.6). Here, the first term defines the dependence of $\overline{e}_{r,max}$ on the system property τ on delay-free case and the second term defines the effect of additional increase on $\overline{e}_{r,max}$ due to the presence of delay on the feedback path.

$$\overline{e}_{r,max} = c_1\frac{1}{\sqrt{2\tau}} + c_2\frac{1}{\sqrt{2\tau}}\left(\sqrt{\frac{\cos(d/\tau)}{1-\sin(d/\tau)}} - 1\right) \tag{8.6}$$

Equation (8.6) relates $\overline{e}_{r,max}$ to the system property τ and the amount of delay on the feedback path, d. It is assumed that, keeping all other properties of the input signal n_2 of figure 8.6 constant, any change of the magnitude of n_2 will affect $\overline{e}_{r,max}$ to the same proportion. Recalling that the input n_2 is defined initially under the condition $k = 1$, eq. (8.7) is proposed, which relates $\overline{e}_{r,max}$ to the term k in addition to τ and d.

$$\overline{e}_{r,max} = k\left(c_1\frac{1}{\sqrt{2\tau}} + c_2\frac{1}{\sqrt{2\tau}}\left(\sqrt{\frac{\cos(d/\tau)}{1-\sin(d/\tau)}} - 1\right)\right) \tag{8.7}$$

Equation (8.7) states the final expression, which is used to approximate the effect of delay on $\overline{e}_{r,max}$ in the presence of random error in relative position information and assuming the nominal (minimum) value of T.

8.1.4 Approximated $\overline{e}_{r,max}$ in Terms of T, k and P

For obtaining an approximate expression for $\overline{e}_{r,max}$ in terms of relative position sampling period T, figure 8.6 is considered with $d = 0$ seconds, i.e. $d(s) = 1$. It is discussed in Chapter 7 that, the term T contributes to $\overline{e}_{r,max}$ in two different ways. The first contribution is by acting as a delay term of duration $T/2$ seconds. The second contribution is by changing the sampling period of the random error signal, which is tracked by the system. In this section, these two contributions of the parameter T are approximated separately, and then they are combined in a single expression. For the approximation of the first contribution, the input signal n_2 is assumed to have constant sampling period of 0.01 seconds. For the approximation of the second contribution, the transfer function $T(s)$ is selected as 1 and the sampling period of the input signal n_2 is designated to be the value of T.

For the first type of contribution to $\overline{e}_{r,max}$, applying the approach presented in Section 3.3.5, the sampling period of T seconds is approximated as a pure time delay of $T/2$ seconds. Thus, the transfer function $T(s)$ is selected as $e^{-sT/2}$. In this configuration, figure 8.6 is of the same form as that considered in the previous section, only with a different delay term. Hence, as an expression of the delay-like contribution of T on $\overline{e}_{r,max}$, eq. (8.7) is used with minor alteration. In eq. (8.7), the delay term d is defined with respect to its nominal value of 0 seconds. For the parameter T, the nominal value is 0.01 seconds, which is denoted by T_0. Hence, with respect to the nominal case, the delay perceived by the dynamical system due to the parameter T is defined as $(T - T_0)/2$. Substituting this term in place of d in eq. (8.7) gives an expression for $\overline{e}_{r,max}$, approximating the delay-like contribution of the parameter T, as shown by eq. (8.8).

$$k\left(c_1\frac{1}{\sqrt{2\tau}}+c_2\frac{1}{\sqrt{2\tau}}\left(\sqrt{\frac{\cos((T-T_0)/2\tau)}{1-\sin((T-T_0)/2\tau)}}-1\right)\right) \tag{8.8}$$

The second type of contribution by T on $\overline{e}_{r,max}$ is through changing the sampling frequency of the random error, which is tracked by the system. It is stated previously that, the random error signal is sampled by the same intervals as the sampling period T. For the approximation of this contribution, the error signal is represented by a sine wave signal of period $2T$, roughly approximating the value of each sample of the error signal as one nonzero region of the sine wave. Thus, the system is treated as if it is under the excitation of this sine wave input signal. In order to obtain a magnitude representation for the output of such a system, frequency response magnitude representation is used instead of H_2 norm. It is assumed that, the effect of the parameter T on $\overline{e}_{r,max}$ due to the change of the closed-loop system dynamics is covered by eq. (8.8). Hence, for the second contribution of the parameter T on $\overline{e}_{r,max}$, the transfer function $T(s)$ on figure 8.6 is selected as 1. Naming the closed loop system $G_r(s)$, the magnitude of such a system's frequency response is given by eq. (8.9).

$$|G_r(s)|=\frac{1}{\sqrt{1+(\tau\omega)^2}} \tag{8.9}$$

In eq. (8.9), the term ω is the frequency of the sinusoidal signal in rad/s. In order to adapt eq. (8.9) to the present case, the term ω is replaced by $2\pi/2T$, yielding eq. (8.10).

$$|G_r(s)|=\frac{1}{\sqrt{1+(\pi\tau/T)^2}} \tag{8.10}$$

Equation (8.10) defines a measure for the magnitude of the output of a system, which is excited by a sinusoidal input signal of period $2T$. The change of the system's output magnitude with respect to the output magnitude in nominal case with $T=T_0$ is defined by eq. (8.11).

$$\frac{1}{\sqrt{1+(\pi\tau/T)^2}}-\frac{1}{\sqrt{1+(\pi\tau/T_0)^2}} \tag{8.11}$$

It is assumed that, the additional increase on $\overline{e}_{r,max}$ due to the change of the sampling period of the random error signal is proportional to the term given in eq. (8.11). Using a positive and real proportionality constant, c_3, and also generalizing for all values of k, the additional increase in $\overline{e}_{r,max}$ is approximated by eq. (8.12).

$$kc_3\left(\frac{1}{\sqrt{1+(\pi\tau/T)^2}}-\frac{1}{\sqrt{1+(\pi\tau/T_0)^2}}\right) \tag{8.12}$$

Equation (8.12) defines the second contribution of the parameter T on $\overline{e}_{r,max}$. Adding eqs. (8.8) and (8.12), a combined expression is obtained, which approximates the effects of the parameters k and T on $\overline{e}_{r,max}$ depending on the system parameter τ. This expression is given by eq. (8.13).

$$\begin{aligned}\overline{e}_{r,max} = k\Bigg(c_1\frac{1}{\sqrt{2\tau}} + c_2\,\frac{1}{\sqrt{2\tau}}\left(\sqrt{\frac{\cos((T-T_0)/2\tau)}{1-\sin((T-T_0)/2\tau)}}-1\right)\\ + c_3\left(\frac{1}{\sqrt{1+(\pi\tau/T)^2}}-\frac{1}{\sqrt{1+(\pi\tau/T_0)^2}}\right)\Bigg)\end{aligned} \tag{8.13}$$

In eq. (8.13), the first two constants, c_1 and c_2, are the same as those in eq. (8.7), which approximates the effect of d on $\overline{e}_{r,max}$. For the nominal case of $T = T_0$, the second and third terms of eq. (8.13) become zero and only the first term remains.

8.2 Comparison of the Approximations With Simulation Results

This section presents the graphical comparisons of the approximations derived in the previous section with the results obtained from the simulations. The main objective herein is to present, to which extent the simulation results can be represented by the approximations given in the previous section. In this context, the scaling capability of the approximations from lower-scale aircraft to higher-scale aircraft is also presented.

The expressions given in eqs. (8.7) and (8.13) are used for approximations of the effects of the parameters d and T on $\overline{e}_{r,max}$, respectively. The three coefficients of eqs. (8.7) and (8.13), namely c_1, c_2 and c_3 were tuned in order to match the magnitudes of the expressions with the data obtained from the simulations. A least-squares-based minimum-search logic was used for obtaining the values of each coefficient.

The logic for determining the values of the coefficients c_1, c_2 and c_3 is given by eqs. (8.14) and (8.15). The procedure is described below using the general term r, which represents x, y or z axes. The same procedure was applied separately for each axis and aircraft scale.

On any given axis, first, eq. (8.14) was applied, in order to determine the values of c_1 and c_2. Then, with the determined values of c_1 and c_2, eq. (8.15) was applied, in order to find the value of c_3. For the τ terms in eqs. (8.7) and (8.13), the values of corresponding aircraft scale and motion axis were used. In eq. (8.14), the term $\overline{e}_{r,max,approx.}$ refers to the expression given by eq. (8.7). In eq. (8.15), the term $\overline{e}_{r,max,approx.}$ represents eq. (8.13). In both eqs. (8.14) and (8.15), the term $\overline{e}_{r,max,sim.}$ represents the value of simulation-based $\overline{e}_{r,max}$ for the scale and axis of concern, cor-

responding to the values of the parameters k, d and T. The terms a_k, a_d and a_T represent the number of values in the corresponding value set of the parameters k, d and T, respectively[1]. The terms C_1, C_2 and C_3 represent the initially-determined range of values for the coefficients c_1, c_2 and c_3 such that, $C_1 \in \mathbb{R}_{>0}$, $C_2 \in \mathbb{R}_{>0}$ and $C_3 \in \mathbb{R}_{>0}$.

$$\begin{aligned} &\underset{c_1,\, c_2}{\arg\min} \left(\sum_{i=1}^{a_k} \sum_{j=1}^{a_d} \left(\overline{e}_{r,max,approx.}(k_i, d_j) - \overline{e}_{r,max,sim.}(k_i, d_j, T_0) \right)^2 \right), \\ &\text{subject to } c_1 \in C_1, c_2 \in C_2 \end{aligned} \tag{8.14}$$

$$\begin{aligned} &\underset{c_3}{\arg\min} \left(\sum_{i=1}^{a_k} \sum_{j=1}^{a_T} \left(\overline{e}_{r,max,approx.}(c_1, c_2, k_i, T_j) - \overline{e}_{r,max,sim.}(k_i, d_0, T_j) \right)^2 \right), \\ &\text{subject to } c_3 \in C_3 \end{aligned} \tag{8.15}$$

The expressions of eqs. (8.7) and (8.13) are used for approximating the relations of k, d and T combinations with $\overline{\boldsymbol{e}}_{r,max}$ in different *simulation cases*, that is, different aircraft scales, as well as disabled or enabled wake vortex effects. The reason for determining the values of the coefficients c_1, c_2 and c_3 with the logic above rather than with manual tuning is to have a constant tuning criterion throughout different cases.

Having the coefficients of eqs. (8.7) and (8.13) determined for each axis, eq. (8.7) and eq. (8.13) were evaluated at each k-d and k-T combination, respectively. The results were laid out over the simulation-based $\overline{\boldsymbol{e}}_{r,max}$ plots of the type presented in Chapter 7. The approximations of eq. (8.7) were plotted over $\overline{\boldsymbol{e}}_{r,max}$ vs. d graphs of constant T. The approximations of eq. (8.13) were laid out over $\overline{\boldsymbol{e}}_{r,max}$ vs. T plots of constant d.

Figure 8.7 presents the approximated and simulated $\overline{\boldsymbol{e}}_{r,max}$ components, as they vary with the parameters k, d and T. The data shown in the figure belong to the case of lower-scale aircraft and disabled wake vortex effects. The figure caption gives the coefficients of the approximations for each axis. The simulated $\overline{\boldsymbol{e}}_{r,max}$ data are essentially the same as those given by figure 7.4 on page 111. For the sake of clarity, smaller markers are used on figure 8.7 for the $\overline{\boldsymbol{e}}_{r,max}$ data points obtained from the simulation. Furthermore, on the $\overline{\boldsymbol{e}}_{r,max}$ vs. d plots, only a quarter of the simulation data points are shown, so that the approximation curves can be more clearly distinguished.

Figure 8.7 shows that, eq. (8.7) almost exactly matches the simulation-based change of $\overline{\boldsymbol{e}}_{r,max}$ with k and d. This holds for all three axes of motion. A similar

[1]Table 7.1 on page 105.

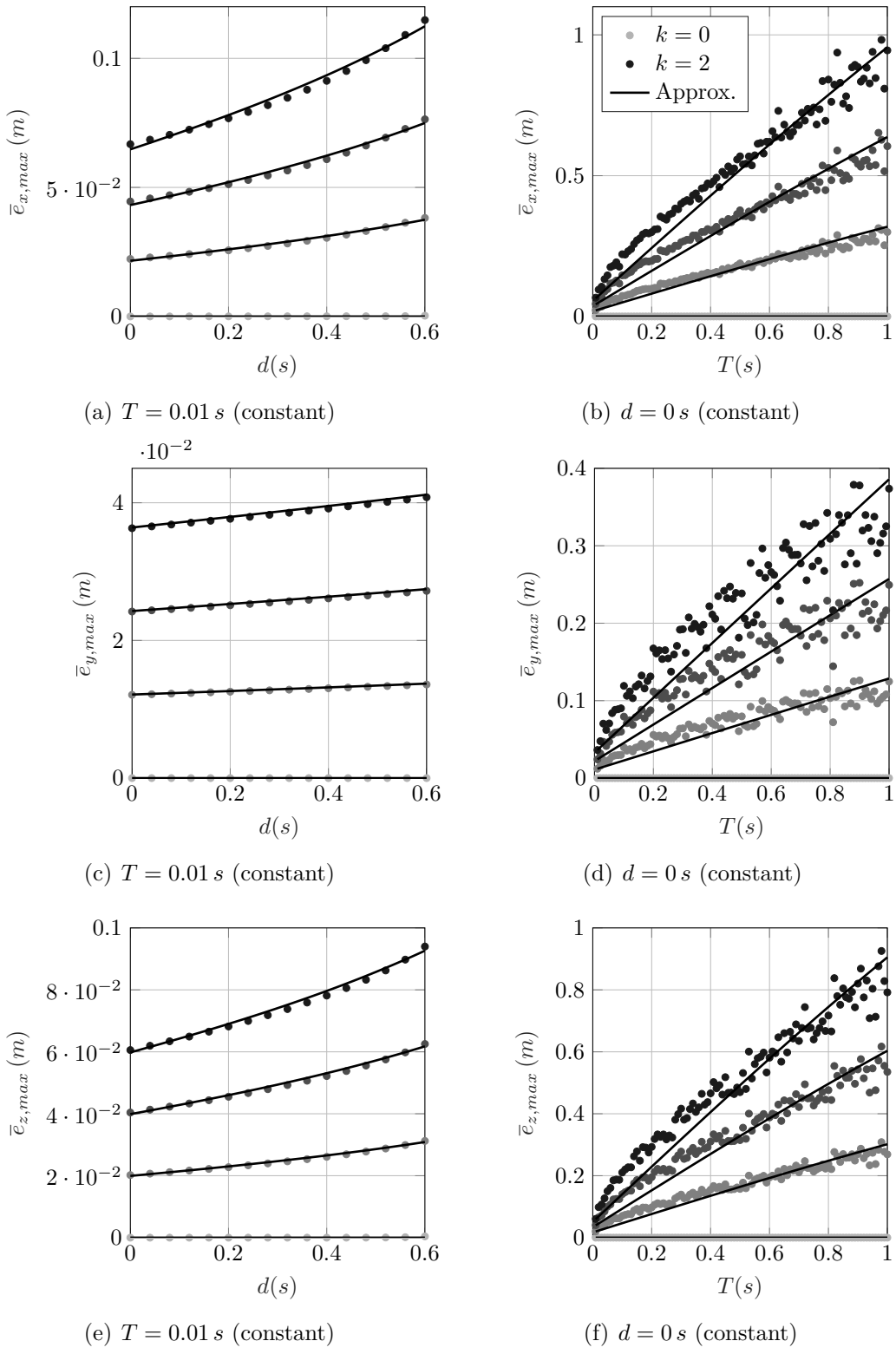

(a) $T = 0.01\,s$ (constant)

(b) $d = 0\,s$ (constant)

(c) $T = 0.01\,s$ (constant)

(d) $d = 0\,s$ (constant)

(e) $T = 0.01\,s$ (constant)

(f) $d = 0\,s$ (constant)

Figure 8.7: Approximation and simulation $\overline{\boldsymbol{e}}_{r,max}$ vs. k, d, T. Lower-scale aircraft, wake effects disabled. Approximation coefficients in the form (c_1, c_2, c_3): $(0.045, 0.084, 1.379)$ for x-axis, $(0.049, 0.074, 1.994)$ for y-axis, $(0.042, 0.060, 1.348)$ for z-axis.

behavior is observed for eq. (8.13) with the simulated change of $\overline{\boldsymbol{e}}_{r,max}$ with k and T. Equation (8.13) constitutes an adequate fit to the scattered simulation data and provides a fairly close representation of the trend of $\overline{\boldsymbol{e}}_{r,max}$ with respect to k and T.

The graphical comparison of approximated and simulated $\overline{\boldsymbol{e}}_{r,max}$ for higher-scale aircraft and for the lower-scale aircraft with wake vortex effects are given in Appendix B. Figure B.12 on page 173 gives the comparison of the simulation-based and approximated $\overline{\boldsymbol{e}}_{r,max}$ for the higher-scale aircraft. Figure B.13 on page 174 shows simulated and approximated $\overline{\boldsymbol{e}}_{r,max}$ of the lower-scale aircraft with wake vortex effects. Both figures show that the approximations fit to the simulation data with similar accuracy as that on figure 8.7. Hence, as figures 8.7, B.12 and B.13 illustrate, once the coefficients of the approximations are determined based on one simulation case, they are able to closely represent the simulation data for the same simulation case.

Another test to which the approximations are subjected in this section is the assessment of their scaling capability. That is, how closely the simulation data of one scale of aircraft can be represented by eqs. (8.7) and (8.13), if their coefficients are determined based on the simulation data with the other scale of aircraft. In order to test this, the coefficients of eqs. (8.7) and (8.13), which were determined based on the simulation data with the lower-scale aircraft, are used. Equations (8.7) and (8.13) were then evaluated with the higher-scale aircraft time constants (τ) and the values of k, d and T corresponding to the higher-scale aircraft simulation. The graphical comparison of the approximations with the higher-scale-aircraft simulation data is presented. Figure 8.8 shows the comparison of the approximations and the simulation data on all three axes. The coefficient values are given in the figure's caption. The values are the same as those used for figure 8.7.

As illustrated by figure 8.8, the approximations provide predictions with a lower degree of accuracy in comparison to the cases presented on figures 8.7 and B.12. The rates of change of $\overline{\boldsymbol{e}}_{r,max}$ components, as well as the values of $\overline{\boldsymbol{e}}_{r,max}$ for $d = 0$ and $T = 0.01s$ cannot be matched as closely by the predictions. On the y and z components of the delay plots, it is shown that, the approximations are able to closely predict the rate of change of $\overline{\boldsymbol{e}}_{r,max}$ with a slight under-prediction of the value of $\overline{\boldsymbol{e}}_{r,max}$ at $d = 0$. On the x axis, the simulation values are matched closely for $d = 0$, however the predicted rate of change is steeper than that provided by the simulation data. This different behavior on the three axes is mainly attributed to the initial determination of the coefficients for approximations of the lower-scale aircraft simulation data. Different set of coefficients would yield different matching behavior on the axes. On the $\overline{\boldsymbol{e}}_{r,max}$ vs. T plots, due to the steeper rate of increase, the initial $\overline{\boldsymbol{e}}_{r,max}$ values at $T = 0.01s$ become comparatively insignificant. On all three axes, milder predictions for the rate of increase of $\overline{\boldsymbol{e}}_{r,max}$ are obtained. This consistent behavior on all axes indicate a limitation of the scaling capability of the approximating expression, eq. (8.13). This limitation may be alleviated by a higher-order representation of the system dynamics. A more detailed analysis for choosing the period of the frequency-response

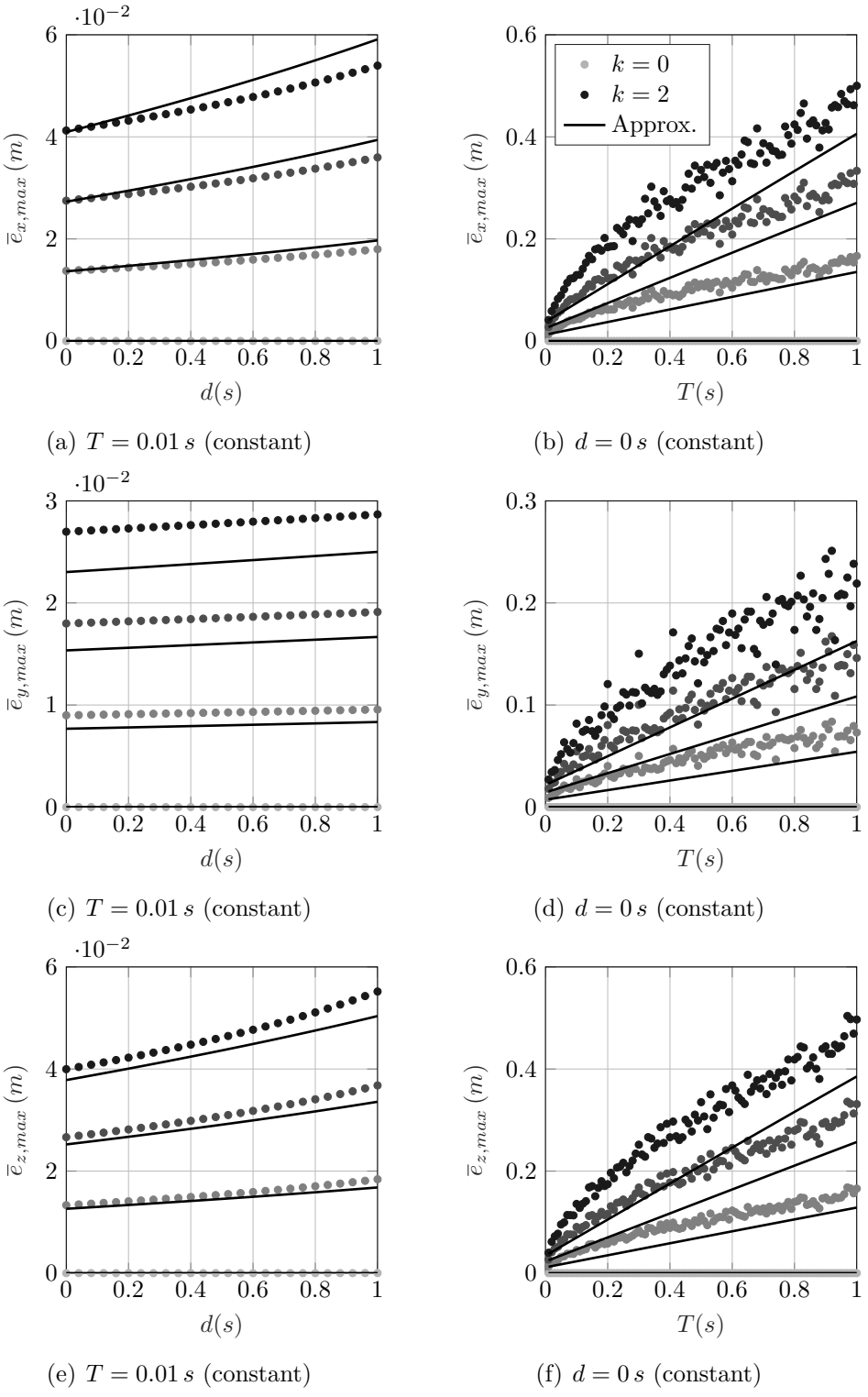

(a) $T = 0.01\,s$ (constant)

(b) $d = 0\,s$ (constant)

(c) $T = 0.01\,s$ (constant)

(d) $d = 0\,s$ (constant)

(e) $T = 0.01\,s$ (constant)

(f) $d = 0\,s$ (constant)

Figure 8.8: Prediction of higher-scale simulation $\overline{\boldsymbol{e}}_{r,max}$ with the approximations tuned with lower-scale aircraft simulation data. Wake effects disabled. Approximation coefficients in the form (c_1, c_2, c_3): $(0.045, 0.084, 1.379)$ for x-axis, $(0.049, 0.074, 1.994)$ for y-axis, $(0.042, 0.060, 1.348)$ for z-axis.

approximation's sine wave input in terms of T may also yield an alternate expression in lieu of eq. (8.13), with enhanced scaling capability. Furthermore, on eq. (8.13), the two different effects of T, namely its effect on the system dynamics and its influence on the random error tracked by the system, are represented by two additive terms separately. An expression approximating the two different effects of T as a single term may also provide a more accurate approximation, hence an improved scaling capability.

Nevertheless, the approximations model the effect of the system scale in the right direction, as they provide decreased $\overline{\boldsymbol{e}}_{r,max}$ predictions for the higher-scale aircraft with respect to the more agile lower-scale aircraft. Furthermore, considering the used length scale factor of 6.25 and corresponding mass ratio of 244 among the higher-scale and lower-scale aircraft, approximations are expected to provide closer predictions for the aircraft of different scale, if the size and weight difference between the two scales of aircraft is lower.

Chapter 9

Conclusions and Future Work

9.1 Summary and Conclusions

Formation flight is a capability, which enables aerial refueling and offers enhanced aerodynamic efficiency for the aircraft, in addition to its operational conveniences for air traffic control and tactical advantages for military applications. The automation of the formation flight has been widely studied in the literature for both manned and unmanned aircraft within the contexts of pilot workload reduction, as well as bringing in the capabilities of manned aircraft to the unmanned aircraft.

For the automated formation flight missions, sensors and navigation solutions provide the necessary flight information, which are processed by the flight control systems in order to carry out the mission automatically. However, the flight data obtained from these sources have certain limitations in terms of accuracy, up-to-dateness and frequency of availability. These deficiencies of the flight data effect the accuracy of the formation keeping, which is critical for the safety, as well as for effectively achieving the intended purpose of the formation flight. Hence, this work investigated how the deficiencies of the flight information, specifically the relative position information, manifest their influence on the accuracy of the automated formation flight.

A simple but frequently-used formation flight scenario has been considered in this work. That is a two-aircraft formation on a straight and level flight path, on which the follower aircraft maintains its position constant with respect to the leader aircraft. The leader and the follower aircraft were selected to be identical. For the term flight information, the relative position information of the two aircraft was used, as this particular information is the most essential one for enabling the automated formation flight. The formation flight scenario has been considered, in which the follower aircraft is responsible for maintaining the formation by its formation flight controller. The formation controller, which regulated the relative position of the two aircraft, as well as all inner-loop feedback controllers were built up using proportional and integral control actions.

The main methodology, which was harnessed in this work for the above-stated research focus, is nonlinear simulations. A MATLAB/Simulink-based simulation environment was used, in which six degree-of-freedom flight-dynamical models of the leader and follower aircraft, their guidance and control algorithms, a flight information model, as well as a wake vortex model had been constructed. The deficiencies of the relative position information has been concretized in terms of three parameters: Delay of the relative position information, d, the period of availability of this information to the formation flight controller, T, and the magnitude of the random error coming along with the relative position information, k. The accuracy of the formation keeping has been represented by the maximum position error in absolute terms, measured during a predefined duration of the formation flight simulation. The simulations were run repetitively by changing the value of one parameter at a time, in order to find out the effect of each parameter on the components of the maximum position error, $\overline{\boldsymbol{e}}_{r,max}$. The results were presented graphically. Complementing the simulation-based analysis, expressions were derived using linear systems theory, which approximate the effects of the parameters k, d and T, as well as the system dynamics on $\overline{\boldsymbol{e}}_{r,max}$.

As they constitute one of the main application targets of automated formation flight, unmanned aircraft models were used in simulations. Keeping the leader and follower aircraft identical, separate sets of formation flight simulations were performed with two aircraft pairs of different scale. The two scales of aircraft were termed as lower-scale and higher-scale aircraft. The lower-scale aircraft was represented by a small unmanned aircraft of 3.2-meter wingspan. A MALE-sized UAV of 20-meter wingspan served as the higher-scale aircraft. The higher-scale aircraft model was derived from the known specifications of the lower-scale aircraft, by applying the relations of dynamic scaling. By this means, it was intended to obtain more directly-comparable results from the simulations of the two scales of aircraft. The main reason for using different scales of aircraft was to investigate, how the aircraft size affects the influence of the parameters k, d and T on $\overline{\boldsymbol{e}}_{r,max}$.

During the application of the procedure outlined above, the following conditions and simplifying assumptions were considered. Hence, unless otherwise stated, they apply to the conclusions drawn within the context of the aforementioned research focus.

1. Formation keeping remains stable for the entire value ranges of d and T.
2. The error component of the relative position information changes randomly throughout the instants, at which the relative position information becomes available to the formation flight controller. The probability distribution of the random error is Gaussian.
3. The leader aircraft flies on a straight and level path and it does not accelerate.
4. Both aircraft are commanded to fly the designated velocity of the formation

flight, which is known to both aircraft.

5. The atmosphere is turbulence-free.

Under the conditions stated above and for the cases in which the wake vortex effects on the follower aircraft are negligible, the following conclusions are drawn for dynamically-scaled aircraft of different size:

◇ The maximum relative position error during formation keeping increases with increasing values of relative position information's k, d and T.

◇ The effects of d and T become only visible on the maximum position error $\overline{\boldsymbol{e}}_{r,max}$, if the relative position information includes nonzero error, i.e., $k > 0$. In this case the formation controller is in a non-steady state, as it continuously tracks the error within the relative position information. The parameters d and T show their effect on $\overline{\boldsymbol{e}}_{r,max}$ during this dynamic state of the formation controller.

◇ The maximum position error during formation keeping is more sensitive against the increase of T than that of d. That is, the increase of maximum position error due to a unit increase of T is greater than the increase of maximum position error due to a unit increase of d. This difference is attributed to the two-way influence of the parameter T on the system. It was shown that, the sampling period of the relative position information, T, affected the closed loop system dynamics in a similar way as the delay, but it also altered the time history of the error, which is tracked by the system. Due to this alteration of the error time history by different values of T, scattering was observed on the change of $\overline{\boldsymbol{e}}_{r,max}$ due to the parameter T.

◇ The actual error time history within the relative position information, which is processed by the formation flight controller, is a factor affecting the magnitude of the maximum position error, $\overline{\boldsymbol{e}}_{r,max}$. However, the tendencies of the change of $\overline{\boldsymbol{e}}_{r,max}$ with respect to the error magnitude k, delay d and sampling period T remain independent of the actual error time history processed by the formation flight controller.

Adhering to the conditions listed above (1–5) and assuming that the wake vortex effects on the follower aircraft are negligible, keeping the leader and follower aircraft identical, the following conclusion is drawn regarding the effect of the aircraft size on the relation of $\overline{\boldsymbol{e}}_{r,max}$ with the parameters k, d and T:

◇ The same amount of increase on the parameters k, d and T causes less increase on $\overline{\boldsymbol{e}}_{r,max}$ for the higher-scale aircraft than for the lower-scale aircraft. That is, the higher-scale aircraft, having slower dynamics than the lower scale aircraft, behaves more robust against the relative position information imperfections. This behavior was observed not only on the simulations with lower-scale and higher-scale aircraft, but also on slower-reacting lateral control channels of both scales

of aircraft with respect to their faster-reacting longitudinal and vertical control channels.

Conforming to all conditions stated above (1–5), the effect of wake vortices on the formation keeping accuracy was investigated for a typical relative aircraft positioning used in probe and drogue aerial refueling. In this case the follower aircraft was commanded to maintain its position at a point two wingspans behind and a quarter wingspan below the leader aircraft while remaining laterally aligned with the leader aircraft. The following conclusion is drawn:

◇ For the relative positioning stated above, the maximum relative position error does not show notable change on the longitudinal axis, as the wake-induced disturbance along this axis is negligibly small for the given relative positioning. The effect of the wake is notable but stabilizing on both the lateral and vertical channels. The most significant effect was observed on the lateral channel. Due to the strong rolling disturbance acting on the follower aircraft, which tends to bring the follower aircraft back to the leader centerline, the increase of $\overline{e}_{y,max}$ with the increase of parameters k, d and T is reduced significantly. On the vertical channel, the downwash acting on the follower aircraft increases with reduced vertical separation, and decreases with the increased vertical separation between the aircraft. As a result of this downwash gradient, the increase of $\overline{e}_{z,max}$ due to the increase of k, d and T is reduced.

Under the conditions stated above (1–5), assuming that the follower aircraft's deviations from steady, straight and level flight condition during the formation keeping is small and thus neglecting the coupling effects between the longitudinal, lateral and vertical motion of the follower aircraft, system-theoretical models were proposed, which approximate the effects of the parameters k, d and T on $\overline{\boldsymbol{e}}_{r,max}$. First-order transfer functions were used in order to represent the formation flight dynamics. In order to represent the maximum position error during formation flight, $\overline{\boldsymbol{e}}_{r,max}$, H_2 norm and frequency-response magnitude formulations were used. Effects of the parameters d and T on $\overline{\boldsymbol{e}}_{r,max}$ were modeled separately. The following observations and conclusions are presented:

◇ The approximation of the effects of k and d on $\overline{\boldsymbol{e}}_{r,max}$ provided almost exact match with the simulation data, provided that the coefficients of the approximation are tuned appropriately. Although the effects of k and T on $\overline{\boldsymbol{e}}_{r,max}$ could not be as accurately matched, the approximations provide close representations of the trend of increase of $\overline{\boldsymbol{e}}_{r,max}$ with the increase of the values of k and T. For the aircraft relative positioning used in this work, the approximations provided matches of the simulation data for both enabled and disabled wake vortex effects. No significant change was observed on the matching accuracy of the approximations in between both cases.

◇ For the cases, in which the approximations were used to predict the effect of the scale of aircraft on the change of $\overline{\boldsymbol{e}}_{r,max}$ with respect to k, d and T, the approximations matched the simulation data less accurately. However, the approximations model the effect of the system scale correctly by shifting the magnitude of approximated $\overline{\boldsymbol{e}}_{r,max}$ in the right direction depending on the dynamics of the aircraft. As means of alleviating the scaling limitation of the approximations, use of a higher-order dynamical representation of the closed-loop system model was recommended. For improving the scaling capability of the approximation for the parameter T, a more elaborate analysis for selecting the period of the frequency-response approximation's sine wave input was indicated. Furthermore, modeling the two-way influence of the parameter T with a single term, instead of two separate, additive terms was recommended.

9.2 Future Work

Possible extensions and improvements to this study, which are left as future work, are stated below.

◇ This work's approach to the simulation of the perturbed relative position information may be extended by inclusion of filter algorithms such as complementary and Kalman filters or dead-reckoning algorithms. Thus the interplay between the filter parameters and the parameters characterizing the relaitve position information's deficiencies, as well as their overall effect on formation keeping could be investigated. It is worth noting that the filter algorithms may require additional states of the leader aircraft, such as velocity. Therefore, the accuracy, up-to-dateness and frequency characteristics of the additional state variables, as well as the filter's tuning parameters will extend the parameter space of the analysis besides governing the overall effectiveness of the filter. In this respect, a preliminary study of the author [70] regarding the effectiveness of a dead-reckoning algorithm during automated formation keeping could be taken as a starting point.

◇ Considering the aerodynamic disturbance on the follower aircraft due to the leader's wake, the effects of the relative position information deficiencies were only investigated at a scenario, in which the follower aircraft was located at a typical probe and drogue aerial refueling position on the longitudinal centerline of the leader aircraft. Since the leader aircraft wake flowfield is nonuniform, the wake disturbance will act on the follower aircraft differently, if it flies at different locations with respect to the leader. Hence, the effect of the relative position information deficiencies can be investigated considering the wake vortex effects, with the follower aircraft flying at other commonly-used formation flight locations. These locations can be the probe and drogue aerial refueling location with

the drogue attached to the leader aircraft's wing, or the leader aircraft's sweet spot, at which the follower aircraft maintains its position for the purpose of drag reduction.

- ◇ Besides the relative position of the two aircraft, the effect of the leader's wake on the follower aircraft depends also on the relative size of the two aircraft. In addition to yielding different wake flowfield and resulting in induced velocities of different magnitude within the flowfield, the sizes of the aircraft also determine how the effective aerodynamic disturbance acts on the follower aircraft. This work only considered identical leader and follower aircraft for the formation flight. Hence, the effects of the relative position information deficiencies on the accuracy of the formation keeping can be investigated using leader and follower aircraft of different relative size.

- ◇ In this study, the formation flight scenario is considered, in which the leader aircraft flies on a straight and level flight path without accelerating, and the follower aircraft maintains its position with respect to the leader aircraft. The analysis presented in this work may be extended for a formation keeping scenario, in which the leader aircraft flies on curved paths. By this means, the effects of path curvature on the accuracy of the formation keeping can be investigated. In this respect, horizontal, circular flight paths of different radii can be considered.

- ◇ This work kept the flight conditions fixed for each scale of aircraft. That is, for each scale of aircraft the formation flight takes place at constant altitude and constant commanded velocity. However, it is presumed that, particularly the commanded velocity of the formation would have an influence on the accuracy of the formation keeping. The follower aircraft may be affected by the deficiencies of the relative position information differently at different flight velocities, especially along its longitudinal axis. Hence, the analysis can be repeated at different flight velocities in order to investigate the influence of the velocity on the accuracy of the formation keeping in the presence of relative position information deficiencies.

- ◇ Apart from the consideration of the aerodynamic disturbance on the follower aircraft due to the leader's wake vortices, this work assumed turbulence-free atmospheric conditions. Hence, the analysis presented in this work could be extended by considering varying levels of atmospheric turbulence acting on both aircraft. It is worth noting that, the sizes of the two aircraft gain further importance when considering the effect of turbulence on them [140].

Bibliography

[1] Eurocontrol Specifications for harmonized Rules for Operatinal Air Traffic (OAT) under Instrument Flight Rules (IFR) inside controlled Airspace of the ECAC Area (EUROAT). Technical Report Edition 2.0, Edition date: 18/09/2013, European Organisation for the Safety of Air Navigation (EUROCONTROL), October 2013.

[2] S. Segal, J. Z. Ben-Asher, and H. Weiss. Derivation of Formation Flight Guidance Laws for Unmanned Air Vehicles. *Journal of Guidance, Control, and Dynamics*, 28(4):733–742, 2005.

[3] C. E. Hanson, J. Ryan, M. J. Allen, and S. R. Jacobson. An Overview of Flight Test Results for a Formation Flight Autopilot. Technical Report NASA/TM-2002-210729, NASA Dryden Flight Research Center, Edwards, California, USA, August 2002.

[4] R. K. Osteroos, D. L. Ferris, J. R. Maddocks, I. P. Moreno, and M. Sabella. Limited Evaluation of the Formation Flight Controller (Project Solo Form). Technical Report AFFTC-TIM-04-08, Air Force Flight Test Center, Edwards Air Force Base, California, USA, December 2002.

[5] Y. Gu, G. Campa, and M. Innocenti. Formation Flight Control. *International Journal of Aerospace Engineering*, 2011. Article ID 798981, 2 pages, doi:10.1155/2011/798981.

[6] M. A. Bennington and K. D. Visser. Aerial Refueling Implications for Commercial Aviation. *Journal of Aircraft*, 42(2):366–375, 2005.

[7] R. K. Nangia and T. Martensson. Towards Design of Efficient Concepts for Civil Air to Air Refuelling (AAR). In *RAeS Applied Aerodynamics Conference "Advanced Aero Concepts, Design & Operations"*, Bristol, United Kingdom, 22–24 July 2014.

[8] R. K. Nangia. Efficient Tankers & Logistics for Introducing Air to Air Refuelling (AAR) into Civil Aviation. In *Conferences in Air Transport & Operations (CATO) / AIAA International Meeting for Aircraft Product Support Processes (IMAPP)*, Delft, The Netherlands, 20–23 July 2015.

[9] Air-to-Air Refuelling. Technical Report ATP-3.3.4.2 (ATP-56(B)) Change 2, NATO Standardization Agency, 2010.

[10] J. D. Anderson. *Introduction to Flight*. McGraw-Hill, Inc., 3rd edition, 1989.

[11] D. Saban and J. F. Whidborne. Modeling of Wake Vortex Effects for Unmanned Air Vehicle Simulations. In *AIAA Modeling and Simulation Technologies Conference*, Chicago, Illinois, USA, 10–13 August 2009.

[12] C. W. Schwarz, K.-U. Hahn, and D. Fischenberg. Wake Encounter Severity Assessment Based on Validated Aerodynamic Interaction Models. In *AIAA Atmospheric and Space Environments Conference*, Toronto, Ontario, Canada, 2–5 August 2010.

[13] E. L. Houghton and P. W. Carpenter. *Aerodynamics For Engineering Students*. Butterworth Heinemann, 5th edition, 2003.

[14] W. Okolo, A. Dogan, and W. Blake. Determination of Sweet Spot for Trailing Aircraft in Formation Flight. In *AIAA Atmospheric Flight Mechanics Conference*, Portland, Oregon, USA, 8–11 August 2011.

[15] A. Kaden and R. Luckner. Modeling Wake Vortex Roll-Up and Vortex-Induced Forces and Moments for Tight Formation Flight. In *AIAA Modeling and Simulation Technologies Conference*, Boston, Massachusetts, USA, 19–22 August 2013.

[16] C. Hanson and J. J. Ryan. Peak-Seeking Optimization of Spanwise Lift Distribution for Wings in Formation Flight. In *AIAA Guidance, Navigation, and Control Conference*, Minneapolis, Minnesota, USA, 13–16 August 2012.

[17] J. Pahle, D. Berger, M. Venti, C. Duggan, J. Farber, and K. Cardinal. An Initial Flight Investigation of Formation Flight for Drag Reduction on the C-17 Aircraft. In *AIAA Atmospheric Flight Mechanics Conference*, Minneapolis, Minnesota, USA, 13–16 August 2012.

[18] H. Shen, N. H. Perkins, K.-C. Lin, and A. Zarmehr. Energy-Saving Formation Flight: A Review of the Past, Present, and Future. *International Journal of Innovative Research in Technology and Science (IJIRTS)*, 4(3):35–40, 2016.

[19] S. Hartjes, M. E. G. van Hellenberg Hubar, and H. G. Visser. Multiple-Phase Trajectory Optimization for Formation Flight in Civil Aviation. In B. Dołęga, R. Głębocki, D. Kordos, and M. Żugaj, editor, *Advances in Aerospace Guidance, Navigation and Control*, pages 389–405. Springer International Publishing, Cham, 2018.

[20] W. Okolo, A. Dogan, and W. Blake. Application of Sweet Spot Determination to a Conventional Pair of Aircraft. In *AIAA Atmospheric Flight Mechanics Conference*, Minneapolis, Minnesota, USA, 13–16 August 2012.

[21] W. Okolo, A. Dogan, and W. Blake. Effect of Trail Aircraft Size on Sweet Spot Location for a Conventional Aircraft Pair in Formation. In *AIAA Atmospheric Flight Mechanics Conference*, Kissimmee, Florida, USA, 5–9 January 2015.

[22] W. Blake and D. Multhopp. Design, Performance and Modeling Considerations for Close Formation Flight. In *23rd AIAA Atmospheric Flight Mechanics Conference*, Boston, Massachusetts, USA, 1998.

[23] K.-U. Hahn and C. W. Schwarz. Safe Limits for Wake Vortex Penetration. In *AIAA Guidance, Navigation and Control Conference and Exhibit*, Hilton Head, South Carolina, USA, 20–23 August 2007.

[24] C. M. Haissig. Military Formation Flight as a Model for Increased Capacity in Civilian Airspace. In *IEEE Digital Avionics Systems Conference (DASC)*, Salt Lake City, Utah, USA, 24–28 October 2004.

[25] J. L. Dargan. Proportional Plus Integral Control of Aircraft for Automated Maneuvering Formation Flight. Master's thesis, Air Force Institute of Technology, Wright-Patterson Air Force Base, Ohio, USA, December 1991. AFIT/GE/ENG/91D-14.

[26] S. A. Ning. *Aircraft Drag Reduction Through Extended Formation Flight*. PhD thesis, Stanford University, Stanford, California, USA, August 2011.

[27] M. Khosrow-Pour. *Dictionary of Information Science and Technology*. IGI Global, 2nd edition, 2012.

[28] A. Faisal, T. Yigitcanlar, M. Kamruzzaman, and G. Currie. Understanding autonomous vehicles: A systematic literature review on capability, impact, planing and policy. *The Journal of Transport and Land Use*, 12(1):45–72, 2019.

[29] L. E. Buzogany. Automated Control of Aircraft in Formation Flight. Master's thesis, Air Force Institute of Technology, Wright-Patterson Air Force Base, Ohio, USA, December 1992. AFIT/GE/ENG/92D-07.

[30] P. R. Rohs. A Fully Coupled, Automated Formation Control System for Dissimilar Aircraft in Maneuvering, Formation Flight. Master's thesis, Air Force Institute of Technology, Wright-Patterson Air Force Base, Ohio, USA, March 1991. AFIT/GE/ENG/91M-03.

[31] V. P. Reyna. Automation of Formation Flight Control. Master's thesis, Air Force Institute of Technology, Wright-Patterson Air Force Base, Ohio, USA, March 1994. AFIT/GE/ENG/94M-01.

[32] M. J. Veth. Advanced Formation Flight Control. Master's thesis, Air Force Institute of Technology, Wright-Patterson Air Force Base, Ohio, USA, December 1994. AFIT/GE/ENG/94D-30.

[33] N. Fezans and T. Jann. Modeling and Simulation for the Automation of Aerial Refueling of Military Transport Aircraft with the Probe-and-Drogue System. In *AIAA Modeling and Simulation Technologies Conference*, Denver, Colorado, USA, 5–9 June 2017.

[34] T. J. Koo and S. M. Shahruz. Formation of a Group of Unmanned Aerial Vehicles (UAVs). In *American Control Conference*, Arlington, Virginia, USA, 25–27 June 2001.

[35] B. T. Clough. Unmanned Aerial Vehicles: Autonomous Control Challenges, A Researcher's Perspective. In *AIAA Infotech at Aerospace Conferences "Unmanned Unlimited" Conference and Workshop & Exhibit*, San Diego, California, USA, 15–18 September 2003.

[36] J. P. Nalepka and J. L. Hinchman. Automated Aerial Refueling: Extending the Effectiveness of Unmanned Air Vehicles. In *AIAA Modeling and Simulation Technologies Conference and Exhibit*, San Francisco, California, USA, 15–18 August 2005.

[37] K. D. Mullens, E. B. Pacis, S. B. Stancliff, A. B. Burmeister, T. A. Denewiler, M. H. Bruch, and H. R. Everett. An Automated UAV Mission System. Technical report, Space and Naval Warfare Systems Center, San Diego, California, USA, September 2010.

[38] M. Pachter, J. J. D'Azzo, and J. L. Dargan. Automatic Formation Flight Control. *Journal of Guidance, Control, and Dynamics*, 17(6):1380–1383, 1994.

[39] C. J. Schuhmacher and R. Kumar. Adaptive Control of UAVs in Close-Coupled Formation Flight. In *American Control Conference*, Chicago, Illinois, USA, 28–30 June 2000.

[40] F. Giulietti, L. Pollini, and M. Innocenti. Autonomous Formation Flight. *IEEE Control Systems Magazine*, 20(6):34–44, 2000.

[41] M. Pachter, J. J. D'Azzo, and A. W. Proud. Tight Formation Flight Control. *Journal of Guidance, Control, and Dynamics*, 24(2):246–254, 2001.

[42] L. Pollini, F. Giulietti, and M. Innocenti. Sensorless Formation Flight. In *AIAA Guidance, Navigation, and Control Conference and Exhibit*, Montreal, Canada, 6–9 Aug 2001.

[43] M. J. Allen, J. Ryan, C. E. Hanson, and J. F. Parle. String Stability of a Linear Formation Flight Control System. Technical Report NASA/TM-2002-210733, NASA Dryden Flight Research Center, Edwards, California, USA, August 2002.

[44] E. Lavretsky. F/A-18 Autonomous Formation Flight Control System Design. In *AIAA Guidance, Navigation and Control Conference and Exhibit*, Monterey, California, USA, 5–8 August 2002.

[45] K. Misovec. Applied Adaptive Techniques for F/A-18 Formation Flight. In *AIAA Guidance, Navigation, and Control Conference and Exhibit*, Monterey, California, USA, 5–8 August 2002.

[46] L. Pollini, R. Mati, M. Innocenti, G .Campa, and M. Napolitano. A Synthetic Environment for Simulation of Vision-Based Formation Flight. In *AIAA Modeling and Simulation Technologies Conference and Exhibit*, Austin, Texas, USA, 11–14 Aug 2003.

[47] R. K. Osteroos, M. Pachter, and D. R. Jacques. Full Capability Formation Flight Control. In *AIAA Guidance, Navigation and Control Conference and Exhibit*, Providence, Rhode Island, USA, 16–19 August 2004.

[48] G. Campa, M. R. Napolitano, B. Seanor, and M. G. Perhinschi. Design of Control Laws for Maneuvered Formation Flight. In *American Control Conference*, Boston, Massachusetts, USA, 30 June–2 July 2004.

[49] B. Seanor, G. Campa, Y. Gu, M. Napolitano, L. Rowe, and M. Perhinschi. Formation Flight Test Results for UAV Research Aircraft Models. In *AIAA 1st Intelligent Systems Technical Conference*, Chicago, Illinois, USA, 20–22 September 2004.

[50] A. Dogan and S. Venkataramanan. Nonlinear Control for Reconfiguration of Unmanned-Aerial-Vehicle Formation. *Journal of Guidance, Control, and Dynamics*, 28(4):667–678, 2005.

[51] M.-J. Tahk, C.-S. Park, and C.-K. Ryoo. Line-of-Sight Guidance Laws for Formation Flight. *Journal of Guidance, Control, and Dynamics*, 28(4):708–716, 2005.

[52] S. M. Ross, M. Pachter, D. R. Jacques, B. A. Kish, and D. R. Millman. Autonomous Aerial Refueling Based on the Tanker Reference Frame. In *IEEE Aerospace Conference*, Big Sky, Montana, USA, 4–11 March 2006.

[53] J. Hansen, G. Romrell, N. Nabaa, R. Andersen, L. Myers, and J. McCormick. DARPA Autonomous Airborne Refueling Demonstration Program with Initial Results. In *International Technical Meeting of the Satellite Division of The Institute of Navigation (ION GNSS)*, Fort Worth, Texas, USA, 26–29 September 2006.

[54] B. Seanor, Y. Gu, and M. Napolitano. 3-Aircraft Formation Flight Experiment. In *IEEE 14^{th} Mediterranean Conference on Control and Automation*, Ancona, Italy, 28–30 June 2006.

[55] B. S. Kim, A. J. Calise, and R. J. Sattigeri. Adaptive, Integrated Guidance and Control Design for Line-of-Sight based Formation Flight. In *AIAA Guidance, Navigation, and Control Conference and Exhibit*, Keystone, Colorado, USA, 21–24 August 2006.

[56] J. Moon, J. V. R. Prasad, and A. J. Calise. Guidance Law for Formation Flight of UAVs: An Adaptive Approach. In *American Helicopter Society 62^{nd} Annual Forum*, Phoenix, Arizona, USA, 9–11 May 2006.

[57] J. Moon, R. Sattigeri, J. V. R. Prasad, and A. J. Calise. Adaptive Guidance and Control for Autonomous Formation Flight. In *American Helicopter Society 63^{rd} Annual Forum*, Virginia Beach, Virginia, USA, 1–3 May 2007.

[58] S. M. Kansari-Zadeh and F. Saghafi. Vision-Based Navigation in Autonomous Close Proximity Operations using Neural Networks. *IEEE Transactions on Aerospace and Electronic Systems*, 47(2):864–883, April 2011.

[59] D. I. You and D. H. Shim. Autonomous Formation Flight Test of Multi-Micro Aerial Vehicles. *Journal of Intelligent Robotic Systems*, 61(1-4):321–337, January 2011.

[60] D. B. Wilson and A. H. Göktoğan. An Unmanned Aerial Vehicle Rendezvous and Formation Flight Demonstration. In *International Conference on Unmanned Aircraft Systems (ICUAS)*, Philadelphia, Pennsylvania, USA, 12–15 June 2012.

[61] K. H. Kienitz, A. Kaden, and R. Luckner. Modeling and Design Considerations for Robust Control of Aircraft in Tight Cruise Formation. In *AIAA Guidance, Navigation, and Control Conference*, Boston, Massachusetts, USA, 19–22 August 2013.

[62] C. Rice, Y. Gu, H. Chao, T. Larrabee, and S. Gururajan. Control Performance Analysis for Autonomous Close Formation Flight Experiments. In *International Conference on Unmanned Aircraft Systems (ICUAS)*, Orlando, Florida, USA, 27–30 May 2014.

[63] F. A. de Almeida. Tight Formation Flight with Feasible Model Predictive Control. In *AIAA Guidance, Navigation, and Control Conference*, Kissimmee, Florida, USA, 5–9 January 2015.

[64] D. B. Wilson, A. H. Göktoğan, and S. Sukkarieh. Guidance and Navigation for UAV Airborne Docking. In *Robotics: Science and Systems Conference*, Rome, Italy, 13–17 July 2015.

[65] D. B. Wilson, A. H. Göktoğan, and S. Sukkarieh. Vision-aided Guidance and Navigation for Close Formation Flight. *Journal of Field Robotics*, pages 1–26, 2015. doi: 10.1002/rob.21637.

[66] B. Cheon, J. Kim, C. Min, D. Han, and K. Cho D. Lee. Monocular Vision-Based Guidance and Control for a Formation Flight. *International Journal of Aeronautical and Space Sciences*, 16(4):581–589, 2015.

[67] E. N. Johnson, A. J. Calise, Y. Watanabe, J. Ha, and J. C. Neidhoefer. Real-Time Vision-Based Relative Aircraft Navigation. *Journal of Aerospace Computing, Information, and Communication*, 4:707–738, April 2007.

[68] R. P. Dibley, M. J. Allen, and N. Nabaa. Autonomous Airborne Refueling Demonstration Phase I Flight-Test Results. In *AIAA Atmospheric Flight Mechanics Conference and Exhibit*, Hilton Head, South Carolina, USA, 20–23 August 2007.

[69] M. C. Kilic and J. C. Dauer. Robustness Analysis of a Formation Flight Guidance Algorithm for Automated Aerial Refueling. In *AIAA Guidance, Navigation, and Control Conference*, Boston, Massachusetts, USA, 19–22 August 2013.

[70] M. C. Kilic and M. J. Meiboom. Sensitivity Analysis of an Automated Formation Flight Based on GPS and Transmission Data Specifications. In *AIAA Guidance, Navigation, and Control Conference*, Kissimmee, Florida, USA, 5–9 January 2015.

[71] G. Bever, P. Urschel, and C. E. Hanson. Comparison of Relative Navigation Solutions Applied Between Two Aircraft. Technical Report NASA/TM-2002-210728, NASA Dryden Flight Research Center, Edwards, California, USA, June 2002.

[72] D. B. Wilson, A. H. Göktoğan, and S. Sukkarieh. A Vision Based Relative Navigation Framework for Formation Flight. In *IEEE International Conference on Robotics & Automation (ICRA)*, Hong Kong, China, 31 May–7 June 2014.

[73] J. Shan and H. T. Liu. Close-Formation Flight Control with Motion Synchronization. *Journal of Guidance, Control, and Dynamics*, 28(6):1316–1320, 2005.

[74] P. R. Rakesh and R. Padhi. Formation Flying of UAVs with Dynamic Inversion Based Partial Integrated Guidance and Control. In *AIAA Guidance, Navigation, and Control Conference*, Portland, Oregon, USA, 8–11 Aug 2011.

[75] G. M. Siouris. *An Engineering Approach to Optimal Control and Estimation Theory*. John Wiley & Sons, Inc., 1996.

[76] R. C. Luo, C.-C. Yih, and K. L. Su. Multisensor Fusion and Integration: Approaches, Applications, and Future Research Directions. *IEEE Sensors Journal*, 2(2):107–119, April 2002.

[77] M. Mammarella, G. Campa, M. R. Napolitano, M. L. Fravolini, Y. Gu, and M. G. Perhinschi. Machine Vision/GPS Integration Using EKF for the UAV Aerial Refueling Problem. *IEEE Transactions on Systems, Man, and Cybernetics-Part C: Applications and Reviews*, 38(6):791–801, November 2008.

[78] P. Binetti, K. B. Ariyur, M. Krstic, and F. Bernelli. Formation Flight Optimization Using Extremum Seeking Feedback. *Journal of Guidance, Control, and Dynamics*, 26(1):132–142, 2003.

[79] R. W. Beard and T. W. McLain. *Small Unmanned Aircraft Theory and Practice*. Princeton University Press, 2012.

[80] S. Park, J. Deyst, and J. P. How. A New Nonlinear Guidance Logic for Trajectory Tracking. In *AIAA Guidance, Navigation and Control Conference and Exhibit*, Providence, Rhode Island, USA, 16–19 August 2004.

[81] Z. Mahboubi, Z. Kolter, T. Wang, G. Bower, and A. Y. Ng. Camera Based Localization for Autonomous UAV Formation Flight. In *AIAA Infotech@Aerospace*, St. Louis, Missouri, USA, 29–31 March 2011.

[82] K. Nakai and K. Uchiyama. Vector Fields for UAV Guidance Using Potential Function Method for Formation Flight. In *AIAA Guidance, Navigation, and Control Conference*, Boston, Massachusetts, USA, 19–22 August 2013.

[83] Y. Nagao and K. Uchiyama. Formation Flight of Fixed-Wing UAVs Using Artificial Potential Field. In *Congress of the International Council of the Aeronautical Sciences (ICAS)*, St. Petersburg, Russia, 7–12 September 2014.

[84] D. R. Nelson, D. B. Barber, T. W. McLain, and R. W. Beard. Vector Field Path Following for Small Unmanned Air Vehicles. In *American Control Conference*, Minneapolis, Minnesota, USA, 14–16 June 2006.

[85] N. A. Shneydor. *Missile Guidance and Pursuit: Kinematics, Dynamics and Control*. Horwood Publishing Limited, 1998.

[86] J. H. Blakelock. *Automatic Control of Aircraft and Missiles*. John Wiley & Sons Inc., 2nd edition, 1991.

[87] Y. Ochi and T. Kominami. Flight Control for Automatic Aerial Refueling via PNG and LOS Angle Control. In *AIAA Guidance, Navigation, and Control Conference and Exhibit*, San Francisco, California, USA, 15–18 August 2005.

[88] J. K. Hall. Three Dimensional Formation Flight Control. Master's thesis, Air Force Institute of Technology, Wright-Patterson Air Force Base, Ohio, USA, March 2000. AFIT/GAE/ENY/00M-06.

[89] C. M. Elliott and A. Dogan. Improving Receiver Station-Keeping in Aerial Refueling by Formulating Tanker Motion as Disturbance. In *AIAA Atmospheric Flight Mechanics Conference*, Chicago, Illinois, USA, 10–13 August 2009.

[90] E. Kim, A. Dogan, and W. Blake. Control of a Receiver Aircraft Relative to the Tanker in Racetrack Maneuver. In *AIAA Guidance, Navigation, and Control Conference and Exhibit*, Keystone, Colorado, USA, 21–24 August 2006.

[91] A. W. Proud. Close Formation Flight Control. Master's thesis, Air Force Institute of Technology, Wright-Patterson Air Force Base, Ohio, USA, March 1999. AFIT/GE/ENG/99M-24.

[92] Q. Zhang and H. H. T. Liu. Robust Design of Close Formation Flight Control via Uncertainty and Disturbance Estimator. In *AIAA Guidance, Navigation, and Control Conference*, San Diego, California, USA, 4–8 January 2016.

[93] C. J. Spinelli. Development and Testing of a High-Speed Real-Time Kinematic Precise DGPS Positioning System Between Two Aircraft. Master's thesis, Air Force Institute of Technology, Wright-Patterson Air Force Base, Ohio, USA, September 2006. AFIT/GCS/ENG/06-12.

[94] L. Pollini, M. Innocenti, and R. Mati. Vision Algorithms for Formation Flight and Aerial Refueling with Optimal Marker Labeling. In *AIAA Modeling and Simulation Technologies Conference and Exhibit*, San Francisco, California, USA, 15–18 Aug 2005.

[95] D. Lobl and F. Holzapfel. Simulation Analysis of a Sensor Data Fusion for Close Formation Flight. In *AIAA Guidance, Navigation and Control Conference*, National Harbor, Maryland, USA, 13–17 January 2014.

[96] W. R. Williamson, M. F. Abdel-Hafez, I. Rhee, E.-J. Song, J. D. Wolfe, D. F. Chichka, and J. L. Speyer. An Instrumentation System Applied to Formation Flight. *IEEE Transactions on Control Systems Technology*, 15(1):75–85, 2007.

[97] F. Lin, K. Peng, X. Dong, S. Zhao, and B. M. Chen. Vision-based Formation for UAVs. In *IEEE International Conference on Control & Automation (ICCA)*, Taichung, Taiwan, 18–20 June 2014.

[98] Y. Deng, N. Xian, and H. Duan. A Binocular Vision-based Measuring System for UAVs Autonomous Aerial Refueling. In *IEEE International Conference on Conrol & Automation (ICCA)*, Kathmandu, Nepal, 1–3 June 2016.

[99] Y. Gu, B. Seanor, G. Campa, M. R. Napolitano, L. Rowe, S. Gururajan, and S. Wan. Design and Flight Testing Evaluation of Formation Control Laws. *IEEE Transactions on Control Systems Technology*, 14(6):1105–1112, 2006.

[100] Y. Gu, G. Campa, B. Seanor, S. Gururajan, and M. R. Napolitano. Autonomous Formation Flight – Design and Experiments. *INTECH Open Access Publisher*, 2009. doi: 10.5772/6475. URL `http://www.intechopen.com/books/aerial_vehicles/autonomous_formation_flight__design_and_experiments`.

[101] A. El-Rabbany. *Introduction to GPS: The Global Positioning System*. Artech House, Inc., 2002.

[102] S. J. Comstock. Development of a Low-Latency, High Data Rate, Differential GPS Relative Positioning System for UAV Formation Flight Control. Master's thesis, Air Force Institute of Technology, Wright-Patterson Air Force Base, Ohio, USA, September 2006. AFIT/GAE/ENG/06-03.

[103] S. Khanafseh, B. Kempny, and B. Pervan. New Applications of Measurement Redundancy in High Performance Relative Navigation Systems for Aviation. In *International Technical Meeting of the Satellite Division of The Institute of Navigation (ION GNSS)*, Fort Worth, Texas, USA, 26–29 September 2006.

[104] S. M. Khanafseh and B. Pervan. Autonomous Airborne Refueling of Unmanned Air Vehicles Using the Global Positioning System. *Journal of Aircraft*, 44(5): 1670–1682, 2007.

[105] P. R. Thomas, U. Bhandari, S. Bullock, T. S. Richardson, and J. L. du Bois. Advances in air to air refuelling. *Progress in Aerospace Sciences*, 71:14–35, November 2014.

[106] S. Krause and B. Aydin. Visual detection of air-to-air refueling drogue. In *International Conference on Unmanned Aircraft Systems (ICUAS)*, Denver, Colorado, USA, 9–12 June 2015.

[107] M. D. Tandale, R. Bowers, and J. Valasek. Trajectory Tracking Controller for Vision-Based Probe and Drogue Autonomous Aerial Refueling. *Journal of Guidance, Control, and Dynamics*, 29(4):846–857, 2006.

[108] C. Martinez, T. Richardson, and P. Campoy. Towards Autonomous Air-to-Air Refuelling for UAVs Using Visual Information. In *IEEE International Conference on Robotics and Automation (ICRA)*, Karlsruhe, Germany, 6–10 May 2013.

[109] J. D. Anderson. *Fundamentals of Aerodynamics*. The McGraw-Hill Companies, Inc., 3rd edition, 2001.

[110] A. Dogan, S. Venkataramanan, and W. Blake. Modeling of Aerodynamic Coupling Between Aircraft in Close Proximity. *Journal of Aircraft*, 42(4):941–955, 2005.

[111] J. L. Hansen and B. R. Cobleigh. Induced Moment Effects of Formation Flight Using Two F/A-18 Aircraft. Technical Report NASA/TM-2002-210732, NASA Dryden Flight Research Center, Edwards, California, USA, August 2002.

[112] G. T. Spence, A. Le Moigne, D. J. Allerton, and N. Qin. Wake Vortex Model for Real-Time Flight Simulation Based on Large Eddy Simulation. *Journal of Aircraft*, 44(2):467–475, 2007.

[113] D. F. Chicka, J. L. Speyer, C. Fanti, and C. G. Park. Peak-Seeking Control for Drag Reduction in Formation Flight. *Journal of Guidance, Control, and Dynamics*, 29(5):1221–1230, 2006.

[114] J. J. Ryan. Formation Flight System Extremum-Seeking-Control Using Blended Performance Parameters. Patent, US 9864380 B1, 9 January 2018.

[115] H. P. Thien, M. A. Moelyadi, and H. Muhammad. Effects of Leader's Position and Shape on Aerodynamic Performances of V Flight Formation. In *International Conference on Intelligent Unmanned Systems (ICIUS)*, Bali, Indonesia, 24–25 October 2007.

[116] A. J. Devuono and C. M. Shearer. Flight Dynamic Response of HALE Aircraft to KC-135 Flowfield. In *AIAA Atmospheric Flight Mechanics Conference and Exhibit*, Honolulu, Hawaii, USA, 18–21 August 2008.

[117] C. E. Hanson. Static Aeroelastic Effects of Formation Flight for Slender Unswept Wings. Technical Report NASA/TM-2009-214649, NASA Dryden Flight Research Center, Edwards, California, USA, August 2009.

[118] R. Brockhaus, W. Alles, and R. Luckner. *Flugregelung*. Springer, 3rd edition, 2011. in German.

[119] B. L. Stevens and F. L. Lewis. *Aircraft Control and Simulation*. John Wiley & Sons, Inc., 1992.

[120] N. A. Weiss. *Introductory Statistics*. Pearson Education, Inc., 9th edition, 2012.

[121] A. Shakoori, M. Mortazavi, and H. Nobahari. Aircraft Dynamically Similar Model Design using Simulated Annealing. *Applied Mechanics and Materials*, 225:323–328, 2012. doi: 10.4028/www.scientific.net/AMM.225.323.

[122] D. Lundström. *Aircraft Design Automation and Subscale Testing - With Special Reference to Micro Air Vehicles*. PhD thesis, Linköping University, Linköping, Sweden, 2012.

[123] C. H. Wolowicz, J. S. Bowman, and W. P. Gilbert. Similitude Requirements and Scaling Relationships as Applied to Model Testing. Technical Report NASA TP 1435 c.1, NASA Dryden Flight Research Center, Edwards, California, USA, August 1979.

[124] T. G. Gainer and S. Hoffman. Summary of Transformation Equations and Equations of Motion Used in Free-Flight and Wind Tunnel Data Reduction and Analysis. Technical Report NASA SP–3070, NASA Langley Research Center, Hampton, Virginia, USA, 1972.

[125] J. W. Edwards and D. A. Deets. Development of a Remote Digital Augmentation System and Application to a Remotely Piloted Research Vehicle. Technical Report NASA TN D–7941, NASA Flight Research Center, Edwards, California, USA, 1975.

[126] R. A. Serway and J. W. Jewett. *Physics for Scientists and Engineers with Modern Physics*. Brooks/Cole, 9th edition, 2014.

[127] K. Ogata. *Modern Control Engineering*. Prentice Hall, 5th edition, 2010.

[128] G. F. Franklin, J. D. Powell, and A. Emami-Naeini. *Feedback Control of Dynamic Systems*. Pearson Higher Education, Inc., 6th edition, 2010.

[129] S. Skogestad and I. Postlethwaite. *Multivariable Feedback Control: Analysis and Design*. John Wiley & Sons, 2nd edition, 2001.

[130] R. Toscano. *Structured Controllers for Uncertain Systems: A Stochastic Optimization Approach*. Springer, 2013.

[131] W. K. Gawronski. *Advanced Structural Dynamics and Active Control of Structures*. Springer, 2004.

[132] E. Jarlebring, J. Vanbiervliet, and W. Michiels. Characterizing and Computing the H2 Norm of Time-Delay Systems by Solving the Delay Lyapunov Equation. *IEEE Transactions on Automatic Control*, 56(4):814–825, April 2011.

[133] S. Walbers. Simulating the Prometheus UAV. Technical Report IB 111-2005/39, Deutsches Zentrum für Luft- und Raumfahrt e.V., Institute of Flight Systems, Aircraft Branch, Braunschweig, Germany, July 2005.

[134] G. Walde. Ein nichtlinearer Regler nach der Methode der Eingangs-/ Ausgangslinearisierung für das unbemannte Luftfahrzeug Prometheus. Diploma thesis, Technische Universität Berlin, Berlin, Germany, May 2010. in German.

[135] S. Park, J. Deyst, and J. P. How. Performance and Lyapunov Stability of a Nonlinear Path-Following Guidance Method. *Journal of Guidance, Control, and Dynamics*, 30(6):1718–1728, 2007.

[136] D. Saban. *Wake Vortex Modelling and Simulation for Air Vehicles in Close Formation Flight*. PhD thesis, Cranfield University, Cranfield, United Kingdom, January 2010.

[137] G. Strang. *Calculus*. Wellesley-Cambridge Press, 1991.

[138] W. Mao and F. O. Eke. A Survey of the Dynamics and Control of Aircraft During Aerial Refueling. *Nonlinear Dynamics and Systems Theory*, 8(4):375–388, December 2008.

[139] L. Mirkin and Z. J. Palmor. Control Issues in Systems with Loop Delays. In D. Hristu-Varsakelis and W. S. Levine, editor, *The Handbook of Networked and Embedded Systems*, pages 628–648. Birkhauser, Boston, 2005.

[140] J. R. Richardson. *Quantifying and Scaling Airplane Performance in Turbulence*. PhD thesis, University of Michigan, Ann Arbor, Michigan, USA, 2013.

Appendix A

Aircraft-Related Data and Simulation Conditions

	Lower scale	**Higher scale**	**Units**
V_d	35	87.5	m/s
γ_d	0	0	rad
χ_d	0	0	rad
h	400	400	m
$\left(x_d^{LF}\right)_{K_L}$	-6.4	-40	m
$\left(y_d^{LF}\right)_{K_L}$	0	0	m
$\left(z_d^{LF}\right)_{K_L}$	0.8	5	m

Table A.1: Commanded formation flight conditions.

	Lower scale		Higher scale		Units
u	35		87.5		m/s
v	0		0		m/s
w	0		0		m/s
ϕ	0		0		rad
θ	0.0422		0.0422		rad
ψ	0		0		rad
p	0		0		rad/s
q	0		0		rad/s
r	0		0		rad/s
δ_e	0.097		0.097		rad
δ_a	0		0		rad
δ_r	0		0		rad
δ_t	0.1692		0.1692		rad
	Leader	**Follower**	**Leader**	**Follower**	
x	50	43.6	50	10	m
y	0	0	0	0	m
z	-400	-399.2	-400	-395	m

Table A.2: Simulation initial conditions.

ρ at 400 m altitude	1.179 kg/m^3
g at 400 m altitude	9.805 m/s^2

Table A.3: Environmental conditions.

	Lower scale	Higher scale	Units
K_{P_V}	0.3564	0.1426	s/m
K_{I_V}	0.07128	0.019	m^{-1}
K_{P_θ}	-2.36	-2.36	–
K_{P_γ}	0.839	0.839	–
K_{I_γ}	2.15623	0.8625	s^{-1}
K_{P_p}	-0.04893	-0.1225	s
K_{I_p}	-0.699	-0.77	–
K_{damp}	0.2	0.6125	s
K_{P_ϕ}	0.97614	0.3866	s^{-1}
K_{P_χ}	1.56875	1.56875	–

Table A.4: Automatic pilot gains.

	Lower scale	Higher scale	Units
K_{P_x}	0.908	0.3536	s^{-1}
K_{P_y}	0.006191	0.000991	m^{-1}
K_{P_z}	-0.024308	-0.0039	m^{-1}

Table A.5: Formation flight controller gains.

	Lower scale	Higher scale	Units
l	20	125	m

Table A.6: Path-following algorithm parameters.

Appendix B

Supplementary Figures

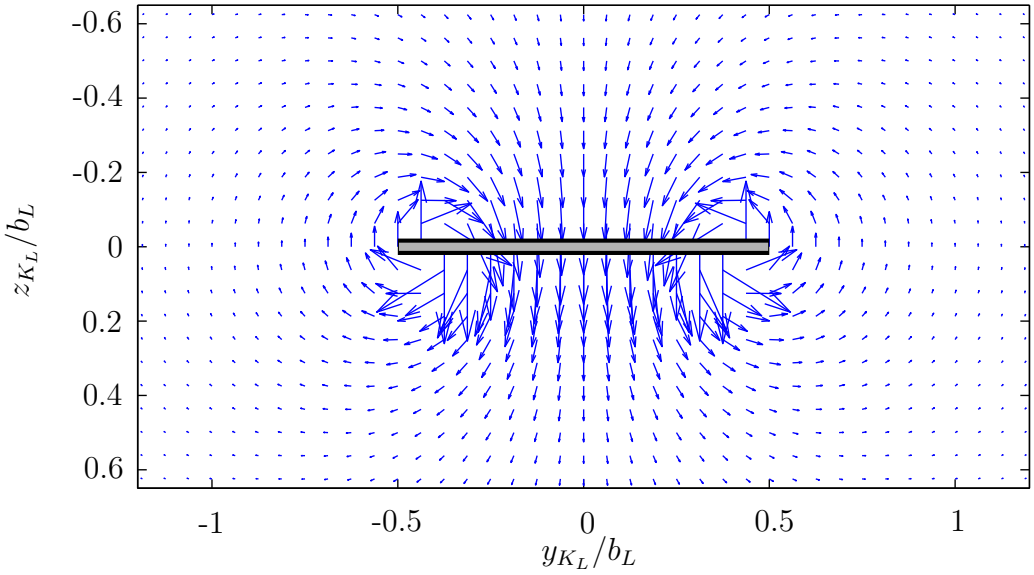

Figure B.1: Leader wake flow field seen from behind the wing, at $x = -0.15b_L$.

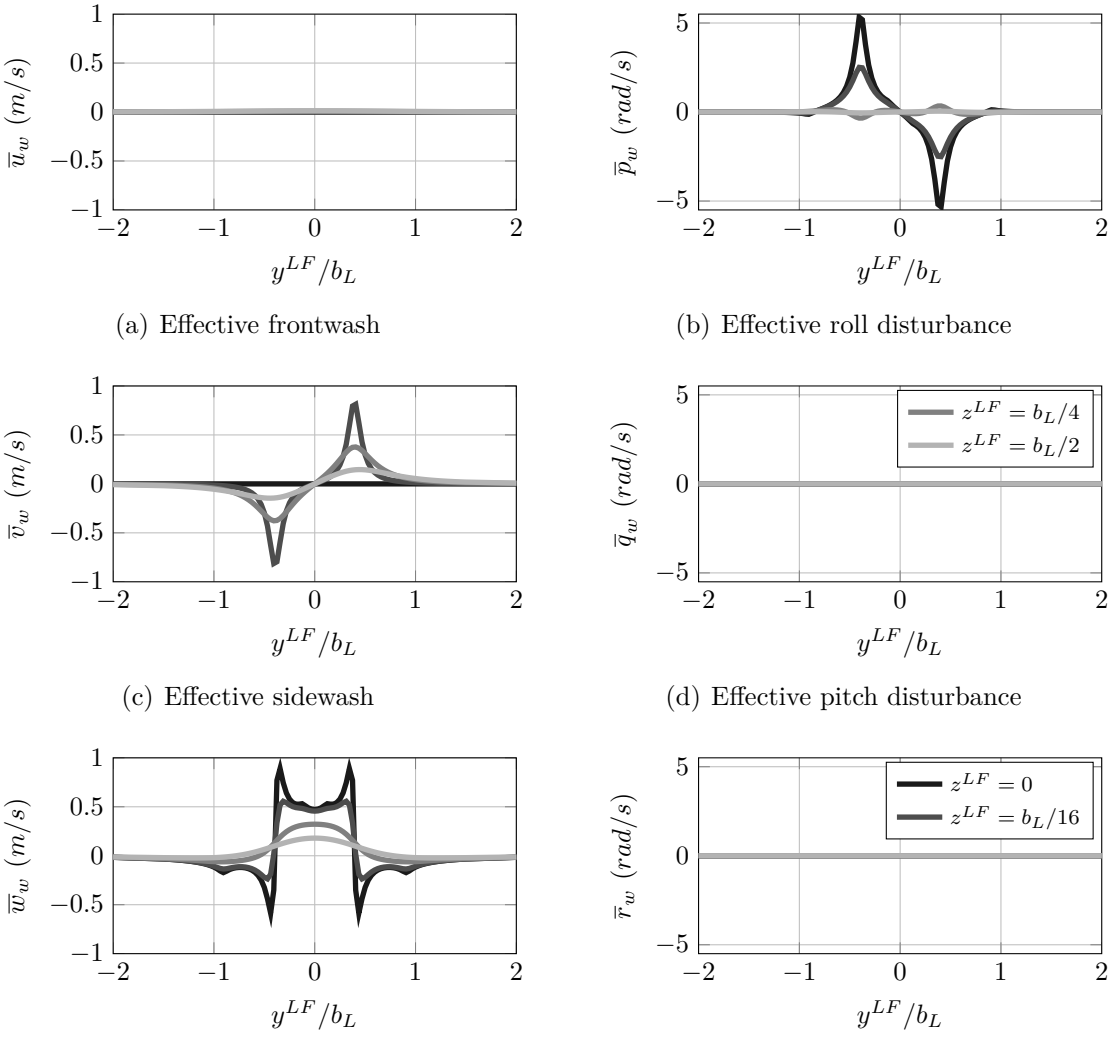

(a) Effective frontwash

(b) Effective roll disturbance

(c) Effective sidewash

(d) Effective pitch disturbance

(e) Effective upwash

(f) Effective yaw disturbance

Figure B.2: Effective leader wake disturbance acting on the follower. Aircraft longitudinal separation: $x^{LF} = -b_L$. Lower-scale aircraft pair at straight and level flight at 400 m altitude with $V = 35\ m/s$.

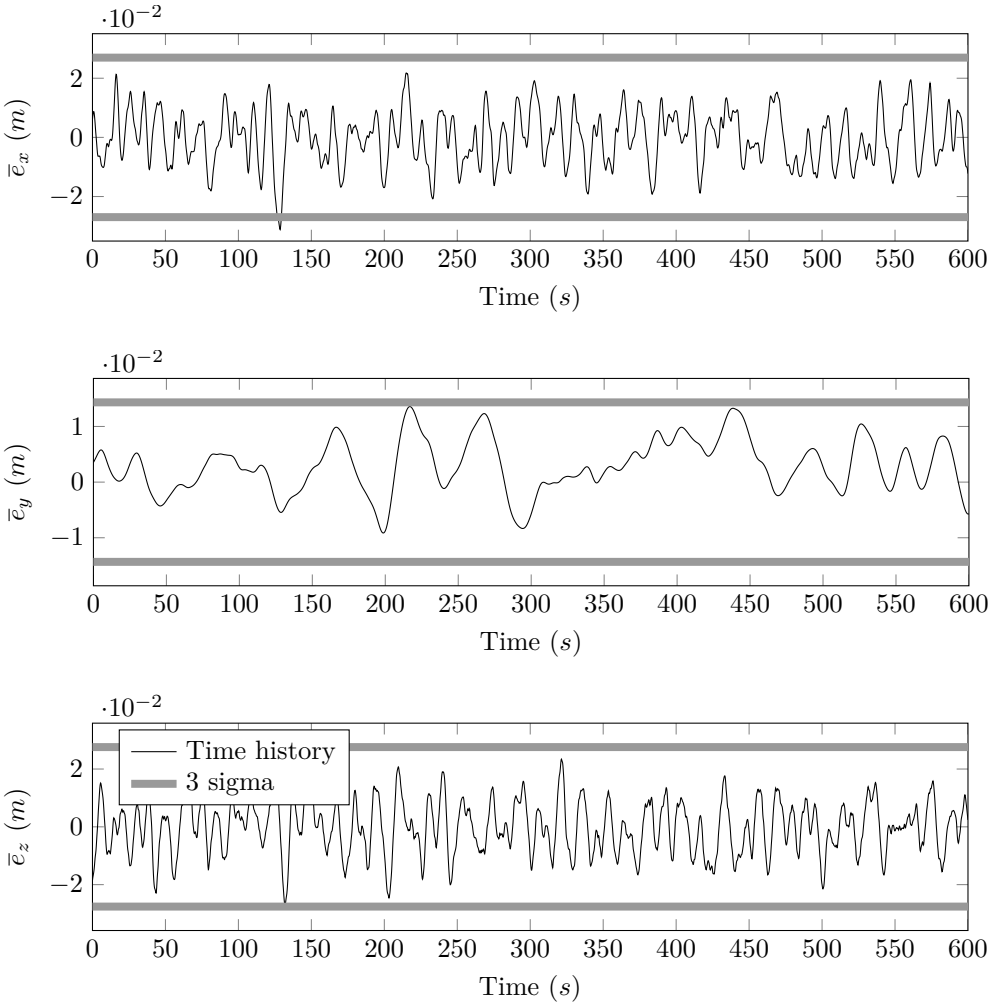

Figure B.3: Example time history of $\overline{\boldsymbol{e}}_r$ taken from the simulation environment. The time history was obtained from a single simulation run, in which the following parameter set was used: $k = 1$, $d = 1\,s$, $T = 0.01\,s$. Higher-scale aircraft models were used and wake vortex effects were disabled.

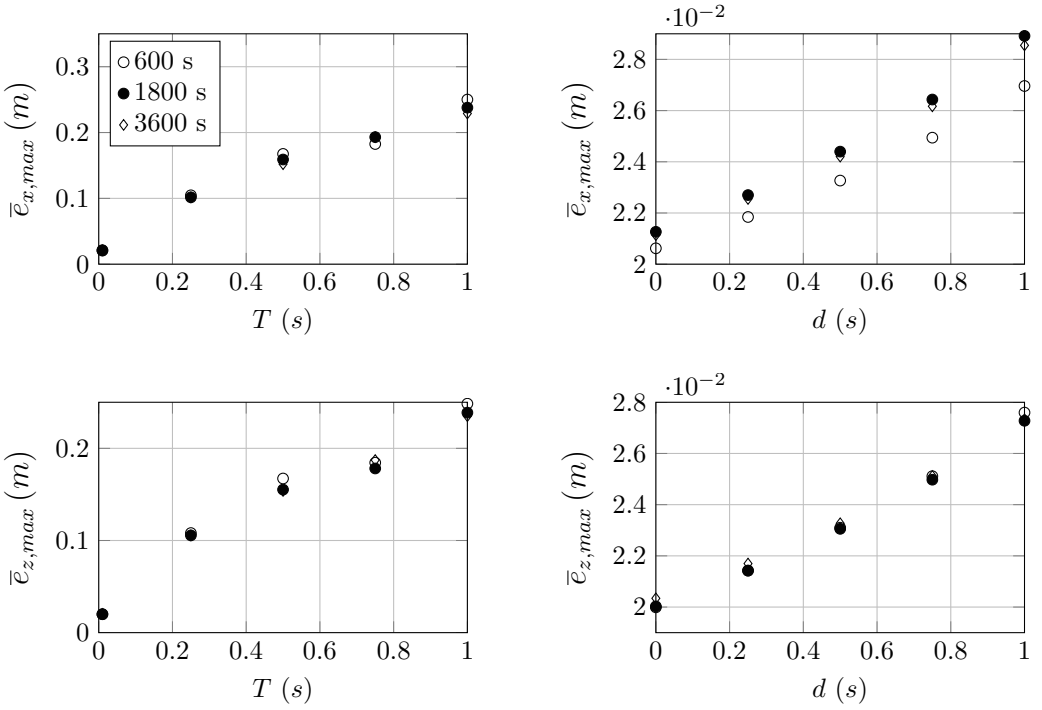

Figure B.4: Change of determined $\overline{e}_{x,max}$ and $\overline{e}_{z,max}$ with respect to different simulation durations. The plots are based on simulations with higher-scale aircraft and $k = 1$.

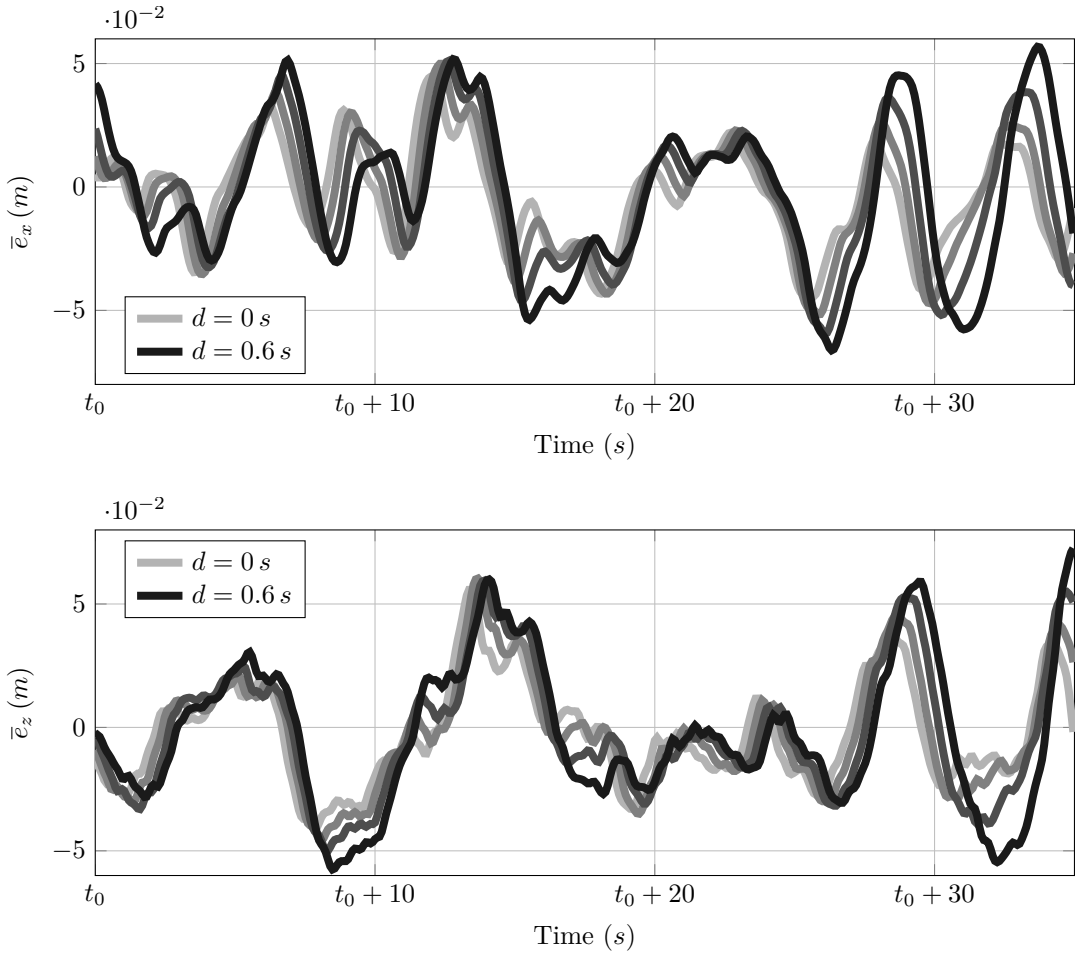

Figure B.5: A 35-second sample time history of $\overline{e}_x$ and $\overline{e}_z$ for different values of d. The plot was generated using the same simulation data as figure 7.4. Parameter values: $k = 2$, $T = 0.01\,s$, $d = \{0, 0.2, 0.4, 0.6\}\,s$. The legend shows only the uppermost and lowermost values from the d-set. The time histories correspond to that for y axis, given by figure 7.6.

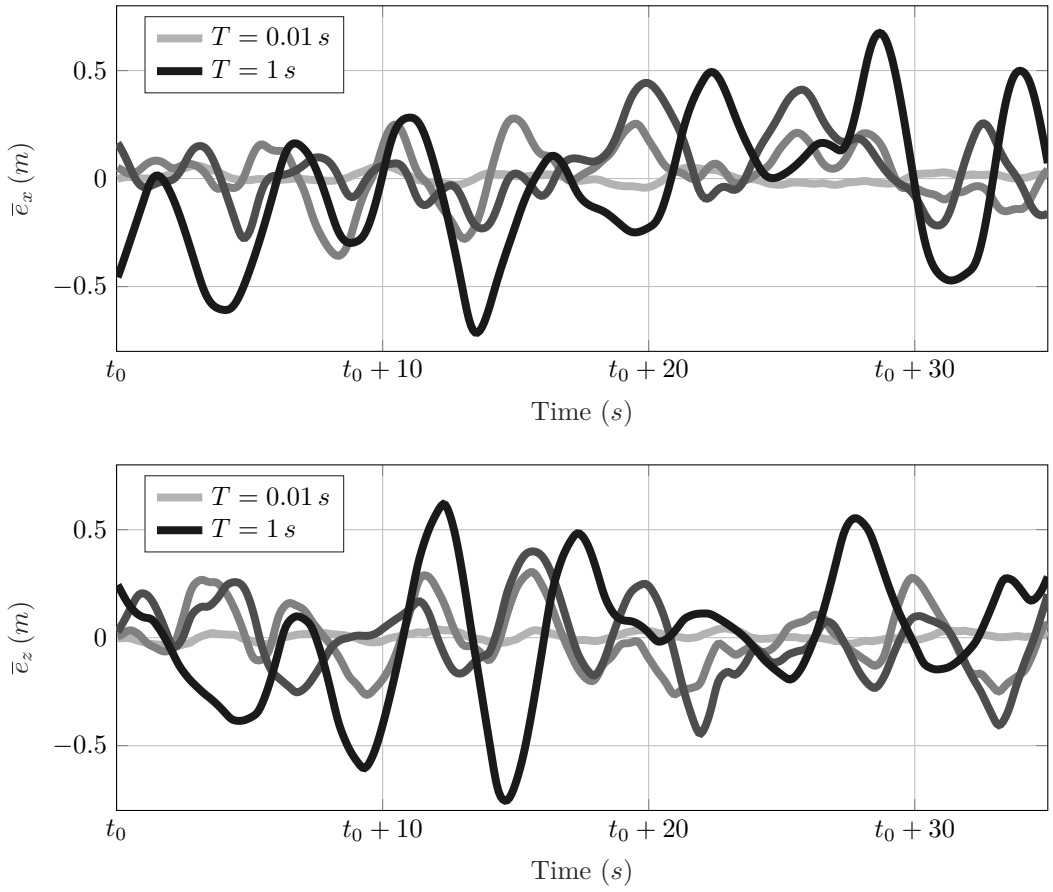

Figure B.6: A 35-second sample time history of $\overline{e}_x$ and $\overline{e}_z$ for different values of T. The plot was generated using the same simulation data as figure 7.4. Parameter values: $k = 2$, $d = 0\,s$, $T = \{0.01, 0.33, 0.66, 1\}\,s$. The legend shows only the uppermost and lowermost values from the T-set. The time histories correspond to that for y axis, given by figure 7.8. The term t_0 is not to be associated with those in figure B.5.

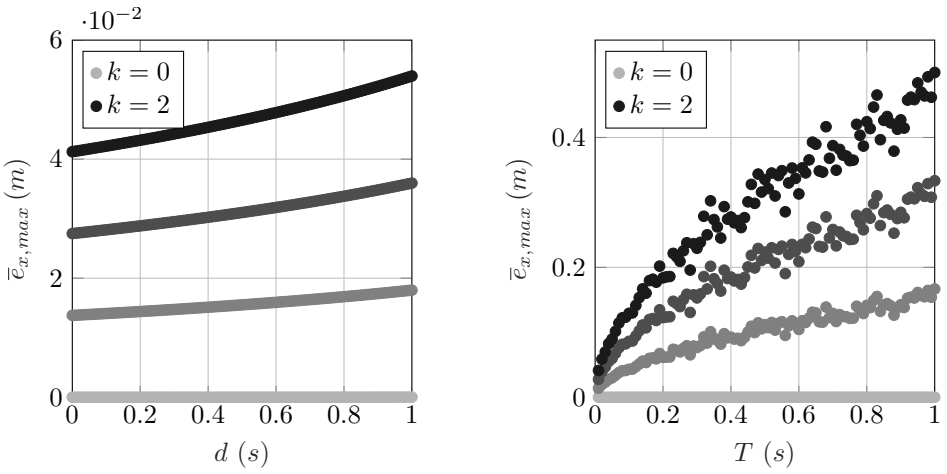

(a) $T = 0.01\,s$ (constant)

(b) $d = 0\,s$ (constant)

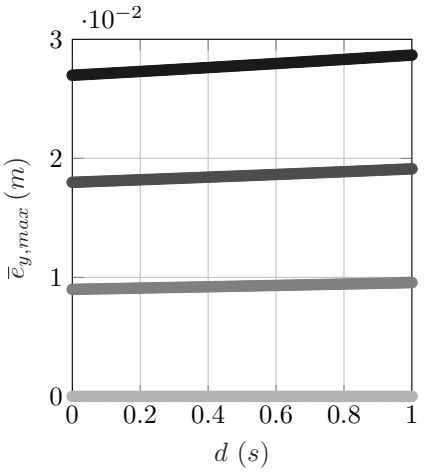

(c) $T = 0.01\,s$ (constant)

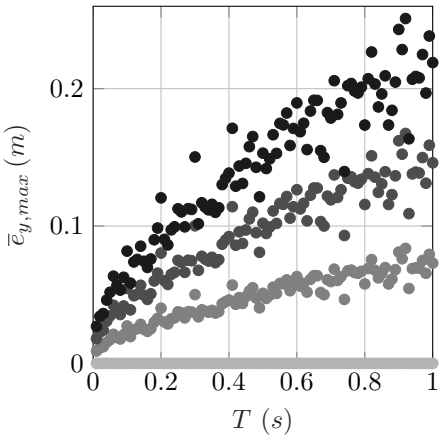

(d) $d = 0\,s$ (constant)

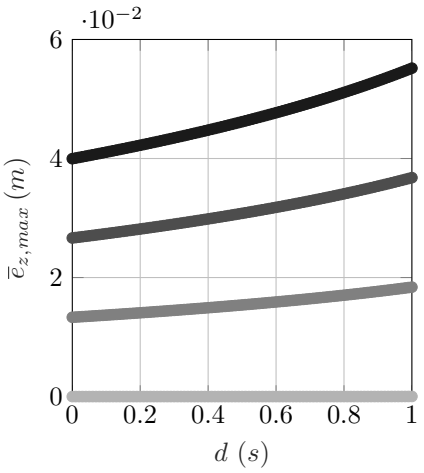

(e) $T = 0.01\,s$ (constant)

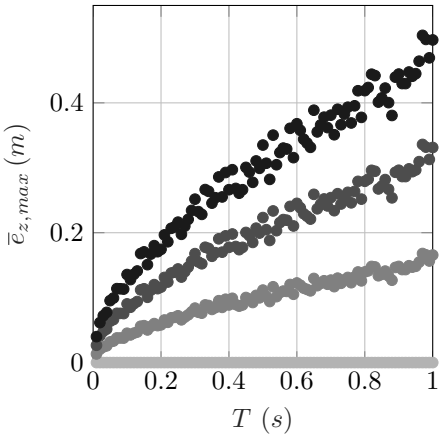

(f) $d = 0\,s$ (constant)

Figure B.7: Component-wise variation of $\overline{\boldsymbol{e}}_{r,max}$ with parameters k, d and T. Results belong to the simulations with higher-scale aircraft and wake vortex effects disabled. $k = \{0, 0.\bar{6}, 1.\bar{3}, 2\}$. The legend shows only the uppermost and lowermost values from the k-set.

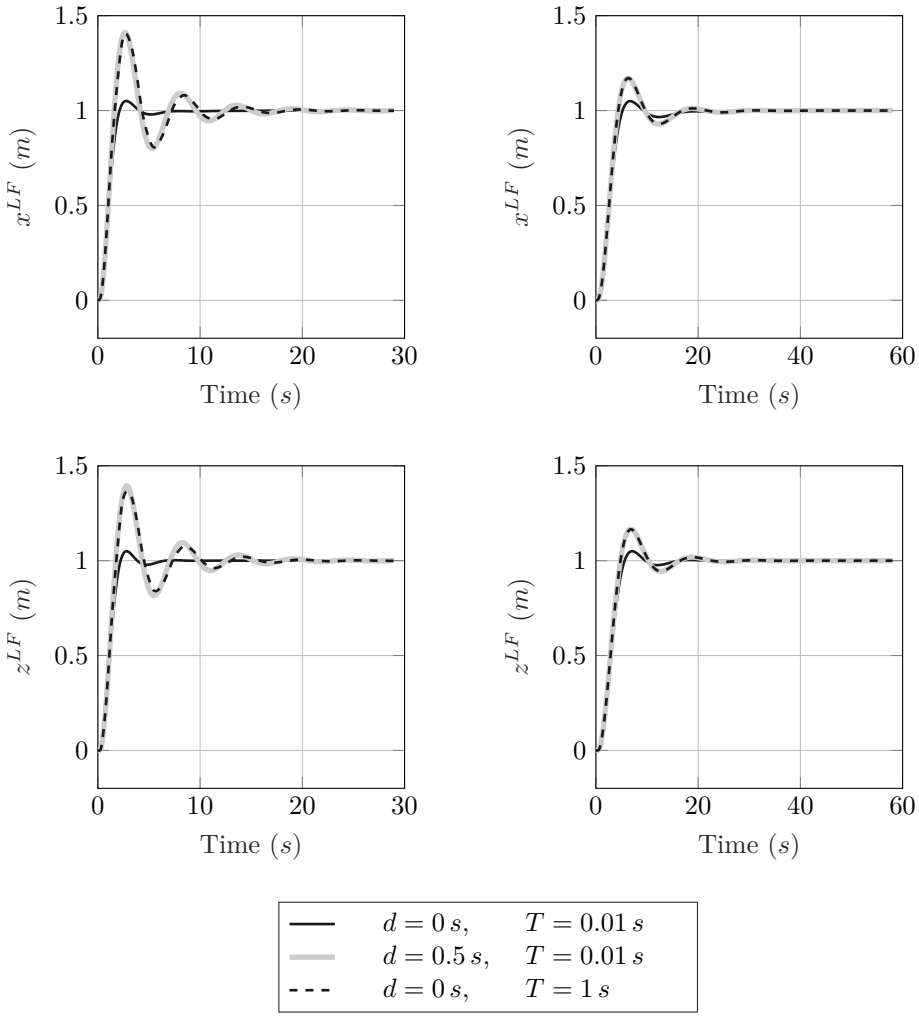

Figure B.8: Comparison of the lower-scale and higher-scale closed-loop systems' unit step responses on x and z axes, as they vary with the parameters d and T. Left column: lower-scale aircraft, right column: higher-scale aircraft.

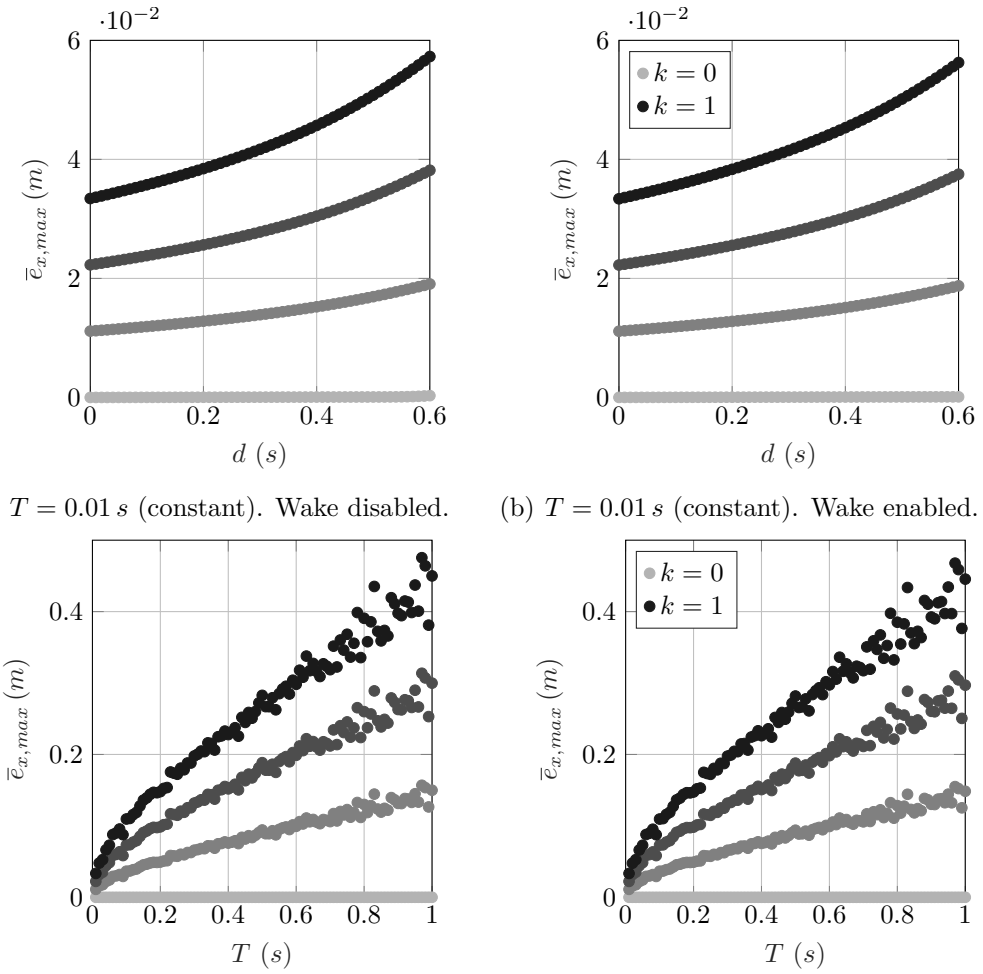

(a) $T = 0.01\,s$ (constant). Wake disabled.

(b) $T = 0.01\,s$ (constant). Wake enabled.

(c) $d = 0\,s$ (constant). Wake disabled.

(d) $d = 0\,s$ (constant). Wake enabled.

Figure B.9: Variation of $\overline{e}_{x,max}$ with parameters k, d and T on lower-scale aircraft, without and with wake vortex effects. $k = \{0, 0.\bar{3}, 0.\bar{6}, 1\}$. The legend shows only the uppermost and lowermost values from the k-set.

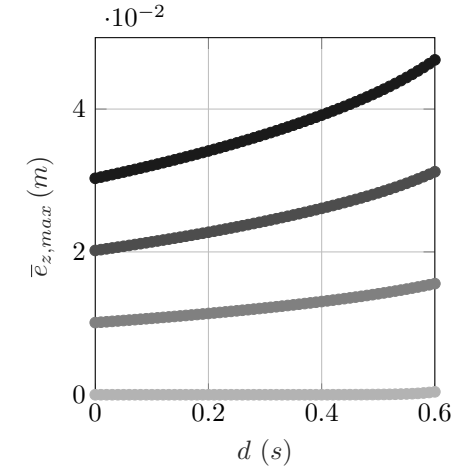

(a) $T = 0.01\,s$ (constant). Wake disabled.

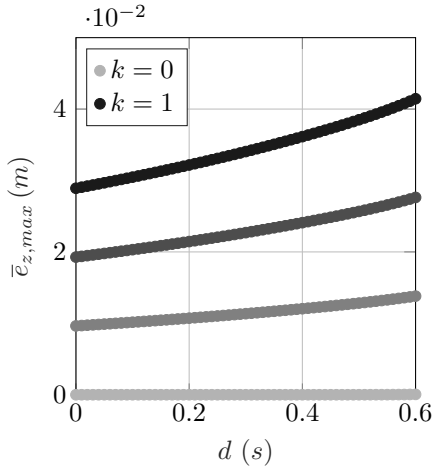

(b) $T = 0.01\,s$ (constant). Wake enabled.

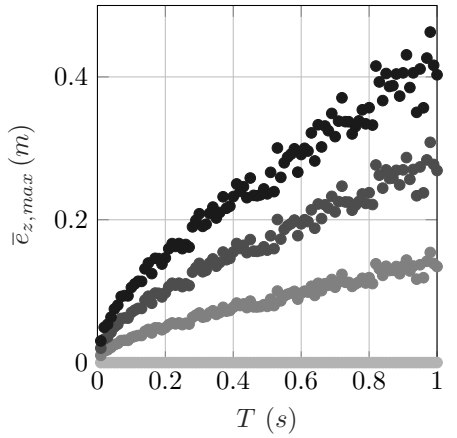

(c) $d = 0\,s$ (constant). Wake disabled.

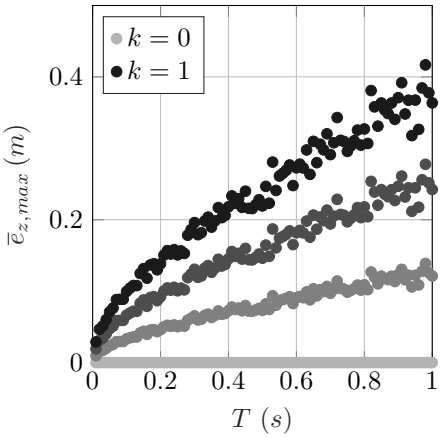

(d) $d = 0\,s$ (constant). Wake enabled.

Figure B.10: Variation of $\overline{e}_{z,max}$ with parameters k, d and T on lower-scale aircraft, without and with wake vortex effects. $k = \{0, 0.\overline{3}, 0.\overline{6}, 1\}$. The legend shows only the uppermost and lowermost values from the k-set.

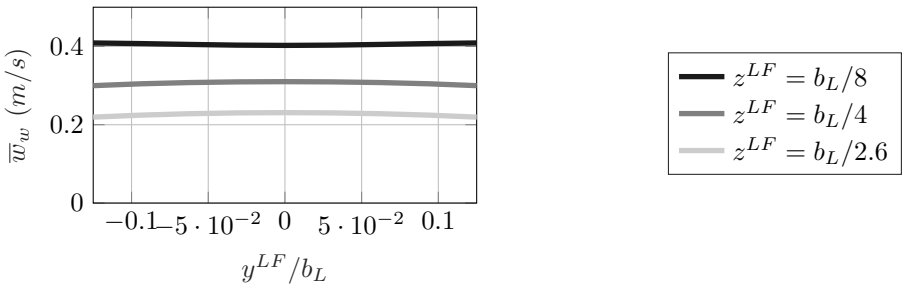

Figure B.11: Effective vertical wake-induced disturbance acting on the follower. Aircraft longitudinal separation: $x^{LF} = -2b_L$. Lower-scale aircraft pair.

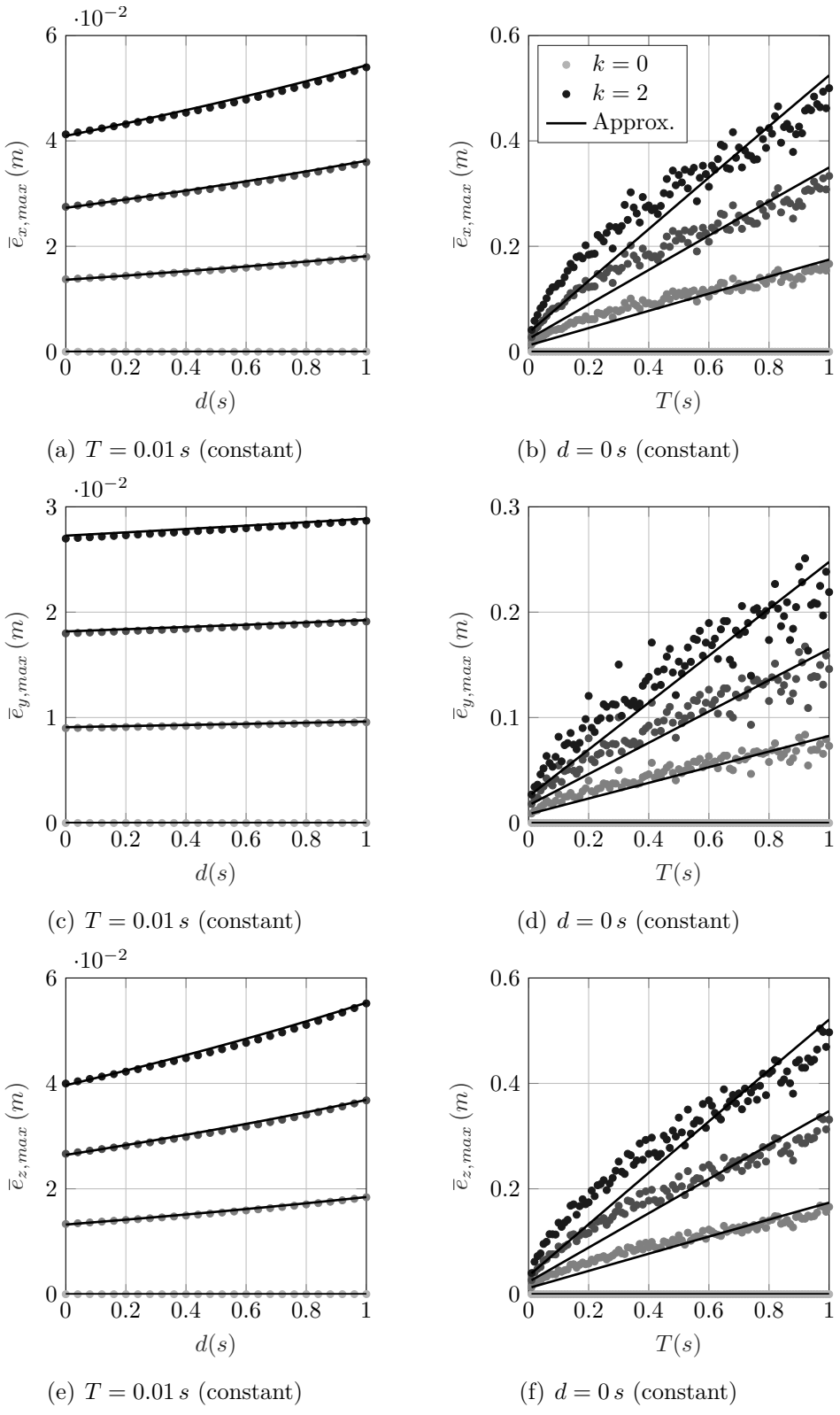

(a) $T = 0.01\,s$ (constant)

(b) $d = 0\,s$ (constant)

(c) $T = 0.01\,s$ (constant)

(d) $d = 0\,s$ (constant)

(e) $T = 0.01\,s$ (constant)

(f) $d = 0\,s$ (constant)

Figure B.12: Approximation and simulation $\overline{\boldsymbol{e}}_{r,max}$ vs. k, d, T. Higher-scale aircraft, wake effects disabled. Approximation coefficients in the form (c_1, c_2, c_3): $(0.045, 0.062, 1.845)$ for x-axis, $(0.058, 0.060, 3.158)$ for y-axis, $(0.044, 0.075, 1.870)$ for z-axis.

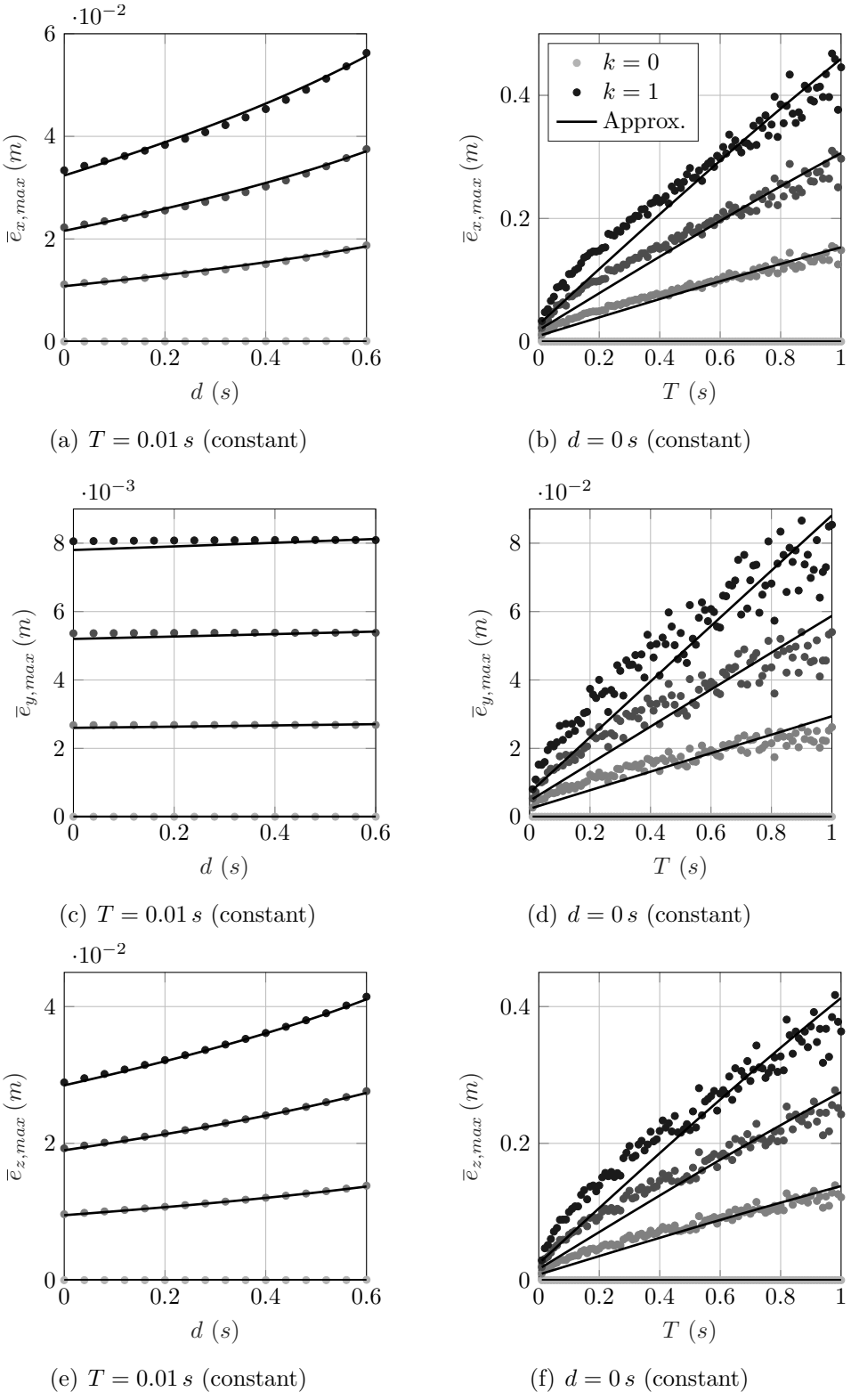

(a) $T = 0.01\,s$ (constant)

(b) $d = 0\,s$ (constant)

(c) $T = 0.01\,s$ (constant)

(d) $d = 0\,s$ (constant)

(e) $T = 0.01\,s$ (constant)

(f) $d = 0\,s$ (constant)

Figure B.13: Approximation and simulation $\overline{\boldsymbol{e}}_{r,max}$ vs. k, d, T. Lower-scale aircraft, wake effects enabled. Approximation coefficients in the form (c_1, c_2, c_3): $(0.045, 0.082, 1.320)$ for x-axis, $(0.021, 0.010, 0.924)$ for y-axis, $(0.040, 0.046, 1.231)$ for z-axis.